Use of inorganic composites for the synthesis of nanoparticles

THESIS SUBMITTED TO

UNIVERSITY OF PUNE

FOR THE DEGREE OF

DOCTOR IN PHILOSOPHY

IN

CHEMISTRY

BY

AMBARISH SANYAL

PHYSICAL AND MATERIALS CHEMISTRY DIVISION
NATIONAL CHEMICAL LABORATORY
PUNE-411008
INDIA

NOVEMBER 2006

CERTIFICATE

This is to certify that the work discussed in the thesis entitled " **USE OF INORGANIC COMPOSITES FOR THE SYNTHESIS OF NANOPARTICLES "** by **AMBARISH SANYAL** for the degree of philosophy in chemistry was carried out under my supervision at the Physical and Materials Chemistry Division of National Chemical Laboratory, Pune. Such material as has been obtained by other sources has been duly acknowledged in this thesis. To the best of my knowledge, the present work or any part thereof, has not been submitted to any other University for the award of any other degree or diploma.

Date: **Dr. Murali Sastry**

Place: NCL, Pune (Research Guide)

CANDIDATE'S DECLARATION

I, Mr. Ambarish Sanyal, hereby declare that the work incorporated in this thesis entitled "**USE OF INORGANIC COMPOSITES FOR THE SYNTHESIS OF NANOPARTICLES "** for the degree of philosophy in chemistry was carried out by me under the guidance of Dr. Murali Sastry at the Physical and Materials Chemistry Division of National Chemical Laboratory, Pune. Such material as has been obtained by other sources has been duly acknowledged in this thesis. I declare that the present work or any part thereof, has not been submitted to any other University for the award of any other degree or diploma.

Date: **Mr. Ambarish Sanyal**

Place: NCL, Pune

ACKNOWLEDGEMENTS

The work presented in this thesis is the result of immense help and support that I have received from many people and it is indeed a great pleasure and the perfect time that I extend my deepest gratitude to all the people involved. To my great delight I would like to express my sincere heart-felt gratitude to ***Dr. Murali Sastry****, my research guide, for providing me the excellent opportunity to take the first step in a research career under his guidance. There goes a saying "You can't direct the wind, but you can adjust the sails". His benign attention, dedicated work and tireless enthusiasm and motivation in the right direction have led to what I am able to present today. Each and every day of my research work, there was something new to learn in store for me and I am really glad that I had the opportunity to learn that every single detail starting from execution of lab-culture to scientific presentations and overall personality growth. Thank you so much Sir.*

I express my sincere thanks to Dr. S. Sivaram, Director NCL, Pune for giving me the opportunity to work in this institute and enjoy all the facilities needed for my research work.

I would like to thank Dr. S.K. Date and Dr. Sourav Pal, former and present Heads, Physical Chemistry Division for their constant support.

I would take this opportunity to extend my sincere thanks to Dr. P. A. Joy and Dr. S. P. Gejji who have been constantly looking after my progress since the time of registration as the members of the monitoring committee.

I would like to extend my special thanks to Dr. Absar Ahmad who has helped me immensely specially in carrying out the work related to biological synthesis of mineral crystals. I would like to express my sincere gratitude to Dr. B.L.V. Prasad who has always been extremely supportive in any kind of discussion that I had during my research work and was always ready to help and give advice during the course of my research. My sincere thanks to Dr. Pankaj Poddar and Mrs. S. D. Adyanthaya for help in all the scientific work pertaining to instruments as well as administrative work. I owe my special gratitude to Ms. Renu Pasricha, Mr. A.B.Gaikwad and Dr. S.R. Sainkar who have always been ready to do the TEM and SEM of my samples. It was only because of their scientific interest and kind-hearted nature that encouraged me to undergo a special training on

Scanning Electron Microscope. I take this opportunity to thank Dr. Neela R. Pavaskar who gave me a hands-on training in XRD and also to Mrs. Anjana Mitra, Mr. P.D. Godbole, Dr. Patil and Dr. A. B. Mandale who have always helped me in the characterization of my samples.

It is indeed a pleasure to thank Dr. K. N. Ganesh and Dr. Pravin S. Shirude Orgainc Chemistry (Synthesis) who have helped me in the Isothermal Titration Calorimetric measurements. I would also like to thank Dr. Ganesh Pandey, Dr. Prabal Banerjee and Mr. Srinivas Dumbre for allowing me to use their UV-irradiation facility during my initial days in NCL.

I would like to express my sincere thanks to my lab-seniors (Ashwini, Sumant, Anita, Dr. Madhukumar, Dr. Senthil, Dr. Jaspreet) who have helped me get accustomed to the research work and lab-environment. I take this opportunity to thank Debu, Saikat, Kannan, Shivshankar, Hrushikesh who have always helped me with various suggestions. I thank all my labmates Akhilesh, Tanushree, Amit, Atul, Vipul, Sourav, Sanjay, Prathap, Ritwik, Sujatha for their constant help and support. Many thanks to Minakshi, Dr. Bapu Bandgar and a special word of mention to Dr. Balaprasad Ankamwar who have been always extremely helpful to give a helping hand in some of my work.

I would like to thank Sourav, Deepti, Manasi and Tanushree for proof-reading the chapters and suggesting valuable corrections in it. I would like to thank all the staff members of the Physical Chemistry Division and specially those from the administrative section who have really helped me steer through all the official jobs in a very easy and helpful manner.

It is also a pleasure to thank all the newcomers to this lab who have interacted with me in a very supportive and helpful manner. A special word of gratitude to the project students Manuel from France, Chinmay, Prachi, Sajini and many others who might not have been directly attached to my research work but were always there to give a helping hand as and when required. I am honoured to have an innumerable number of friends here in NCL and I would also like to take this opportunity to thank all of them and also those from the "Bengali" group in the hostel who have always helped me with some fruitful scientific discussions.

I would like to thank the Council of Scientific and Industrial Research (CSIR), Government of India, for providing the financial support in order to carry out my research work.

This thesis would not have been possible without the continuous, motivated and moral support from my parents, brother and other relatives who have always been extremely patient, supportive and encouraged me to look optimistically into the future even in my stressful times. Finally I would like to thank Tanushree whose constant persevering and scientific outlook have always helped in trying to achieve the perfection during my research work. Last but not the least I would like to express my sincere gratitude to all those in particular to the teachers in my school, and Jadavpur University, Kolkata who have encouraged me in pursuing a research career.

November 2006 **Ambarish Sanyal**

Table of Contents

Chapter 1: Introduction

Chapter 2: Characterization techniques

Chapter 3: Synthesis of gold and platinum nanosheets at the liquid-liquid interface

Chapter 4: Synthesis and assembly of metal nanoparticles using Keggin-amino acid hybrid nanostructures

Chapter 5: Biological synthesis of mineral crystals

Chapter 6: Conclusions

CHAPTER I

Introduction

This chapter provides an introduction to the thesis by describing the stimulating properties of a material in the nano-regime and then moves onto different types of nanostructures. It gives a brief overview on the various methods to create low-dimensional nanostructures. It also includes the need for synthesis of organic-inorganic hybrid as well as anisotropic nanostructures. Besides, it provides a brief idea on the biomimetic growth of inorganic minerals by use of different agents of purely biological origin. Finally, it concludes with the motivation behind the work and a chapter-wise description of the protocols carried out in this thesis.

1.1 Introduction

There has been a saying since a long time that "Necessity is the mother of invention", hence people have been passionate enough to nurture science and transform it into fruitful technology. Things, which had been a trend of yesterday, have become an essentiality of today. Nanotechnology is one such innovation that has become the indispensable tool for researchers from various fields. Although it might sound somewhat weird as this is one such field where one cannot see through naked eyes in a very true sense but definitely compelled to believe the potentiality of the size regime. As was very aptly said by John Dewey in his 'Quest for Certainty' that "Every great advance in science has issued from a new audacity of the imagination." Nanoscale is thus the imaginative world of 'the small', where one nanometer refers to one billionth of a meter, or 1/ 20000 times the smallest cell that a naked eye can see. So now the obvious question is upto what length scale shall we speak of nanometer, 10 nm, 100 nm or 1000 nm? The answer to this is definitely debatable, but most scientists feel that the length scale can be extended to that point where the chemical properties are different compared to the bulk regime.

Nanomaterials thus show unusual physico-chemical and opto-electronic properties which are different from their bulk counterparts [1]. In fact, the observance of this rather unusual and spectacular phenomenon dates back to the Roman Empire (4^{th} century AD) where a cup showing the myth of King Lycurgus showed different colours when viewed at transmitted and reflected lights. The cup popularly known as the "Lycurgus Cup", still present in the British Museum, was found to contain very small amounts of gold and silver in the nano size that resulted in the bright red colour when viewed in transmitted light [2]. Just as nanoscience has drawn innumerable people to work in unison to develop advanced materials, in a similar manner the use of nanomaterials has been diversified into various fields like electronics [3], catalysis [4], optics [5], drug delivery [6], metallurgy [7] and sensors [8]. Nanoparticles thus form a part of the 'colloid' family which had been known since the later part of 19^{th} century. Colloids, which were first coined in 1862, actually came from the Greek word, "kolla" which meant glue. The reason for such a name is that some of the original colloidal solutions, in order to differentiate from crystallites, at that time were composed of

organic substances that were glues. It was only in 1857 that Michael Faraday showed that the intense ruby red colour as was observed in the "Lycurgus Cup" was due to metallic gold in colloidal form. In metals, electrons are least confined and are delocalised in a large space. There is an overlap of the valence and the conduction bands giving electrons their mobility, thus giving rise to conductivity. However, as the size of the material decreases, the electronic motion is confined, giving rise to a separation of the valence and the conduction bands, which gives rise to semiconductor properties.

Further decrease in size results in the formation of insulator like properties. For noble metals, when the size of the metal decreases to such an extent (size becomes less than the distance between successive collisions of the electrons with the lattice centers) that the surface free electrons are able to vibrate coherently, strong absorption results in the visible and near UV region. This coherent oscillation when resonant with that of the electromagnetic radiation, causes the intense colour, a property commonly termed as "Surface Plasmon Resonance" as is shown in the schematic of Figure 1.1. Later on, in the beginning of the 20th century, Mie solved Maxwell's equations and explained the scattering phenomena of spherical nanoparticles with electromagnetic radiation [9].

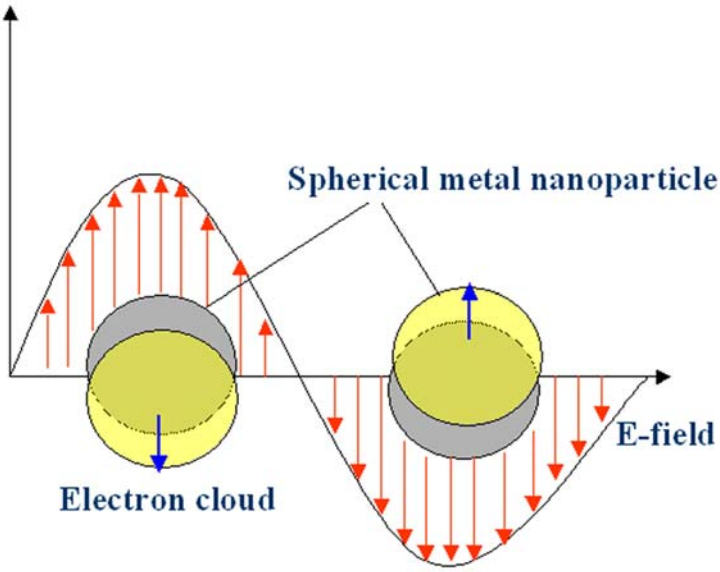

Figure 1.1: *Schematic showing the distortion of electron cloud of a spherical metal nanoparticle by electromagnetic radiation leading to Surface Plasmon Resonance. (Ref: Schatz and co workers, J. Phys. Chem. B* ***2003****, 107, 668.)*

The only material related functions in the Mie's theory were the complex dielectric function of the metal and the dielectric constant of the surrounding medium. Thus, the above-mentioned theory could predict the UV-Vis spectra of small metallic particles of known dielectric function and dissolved in a solvent of known dielectric constant. Another important aspect of nanomaterials is their stability. The electrostatic interaction of colloidal particles is aptly described by the DLVO theory, named after Derjaguin, Laundau, Verway and Overbeek, which represent a combination of Vander-Waal's attraction and electrostatic repulsion. The stability of the colloidal solution will largely depend on the electrolyte concentration and surface charge density of the nanoparticle. For a solution containing nanoparticles of low charge density, the repulsion energy barrier is low enough to bring about slow aggregation known as flocculation. Thus, above a particular electrolyte concentration, the double-layer repulsion vanishes and the colloid precipitates out. Hence, the addition of a capping agent becomes a necessary factor in order to make the colloid thermodynamically stable [10].

Synthesis of stable nanoparticles has thus been always a challenge to materials scientists over the years. There are basically two different approaches for the synthesis of nanoparticles: the "top-down" and the "bottom-up" approach. The "top-down" approach involves breakdown of a bulk object into its smaller and smaller counterparts that includes processes like ball milling [11], lithography [12] and laser-beam induced growth [13]. However, ball-milling method, one of the oldest commercially used methods for 'top-down' approach, is not considered efficient due to a lot of contamination as well as technical limitations. The second one, "bottom-up" approach, which involves construction of matter atom by atom, is hence somewhat superior to the "top-down" approach. This includes processes like chemical sol-gel synthesis [14], precipitation [15], self- assembly [16], microemulsion and template based synthesis [17]. Self-assembly of molecules into an expanded form of exhilarating molecular structures has drawn attention due to a wide range of applications ranging from materials synthesis [18] to catalysis [19] and separation techniques [20].

1.2 Different methods for the synthesis and assembly of nanoparticles

1.2.1 Sol-gel technique

The sol-gel process involves the conversion of a solution of molecular precursors by a chemical reaction into a sol or a gel, which is subsequently transformed into a crystalline material upon drying, densification, or calcination. The gel is a polymer of three-dimensional network with surrounding interconnected pores. Hydrolysis and polycondensation of tetraethoxysilane (TEOS) under alkaline conditions in ethanol medium have resulted in the synthesis of SiO_2 particles having 20 nm diameters [21]. In some cases the tendency of these nanoparticles formed against aerial oxidation is inhibited by use of amino acids like alanine, tryptophan etc [22]. In some recent work this technique have been used to prepare porous spheres of γ-Al_2O_3 [23]. However, in this case a surfactant SPAN-80 was used along with the dehydrating agent. Apart from metal oxides like silica, Titania and zirconia, the sol-gel technique has been used to synthesize different ferroelectric materials like $BaTiO_3$, $PbTiO_3$, $BaSrTiO_3$ [24, 25]. One important advantage of the sol-gel technique is the production of homogeneous ultrafine powders with the additional capability of industrially scaling up. One distinct disadvantage of surface sol-gel technique is that as a low temperature technique this might give low-density or incompletely crystallized films.

1.2.2 Microemulsions and reverse micelle technique

Schulman in 1943 noted that certain ratios of water, oil, surfactant and a cosurfactant produced a transparent solution which he termed as “microemulsion” [26]. The oil phase usually consist of long chain hydrocarbons while the surfactant used by Schulman, cetyl trimethyl ammonium bromide (CTAB), is also used nowadays. The cosurfactant , which generally consist of small organic molecules like alcohols acts as “spacers” and minimize the electrostatic repulsion between the polar head groups of the surfactants. These spherical aggregates are termed as “reverse micelles” when the nanoreactor “water pool” is in an oil medium. These reverse micelles are generally characterized by ω_0, which is the ratio of the molar concentration of water and the surfactant S. Therefore,

$$\omega_0 = \frac{[H_2O]}{[S]}$$

The reduction of metals in this reverse micellar technique is probably one of the earliest methods where an aqueous solution of H_2PtCl_6 was taken in a reverse micelle and aqueous sodium borohydride or hydrazine in the other reverse micelle. Fusion of these two reverse micelles resulted in the formation of 3 nm Pt nanoparticles, which had potential use in catalysis [27]. Various other inorganic materials like $CoFe_2O_4$, Fe_3O_4, Al_2O_3, SnO_2 and $Cu_2[Fe(CN)_6]$ have been prepared by use of various surfactants like SDS, AOT and Triton X-114 [28-32].

1.2.3 Sonochemical synthesis

Sonochemistry is the research area in which molecules undergo chemical reaction due to the application of powerful ultrasound radiation in the range of 20 KHz to 10 MHz. Though there have been a number of theories explaining the disruption of chemical bond during sonication, the general event in a sonochemical-assisted synthesis is the creation, growth and collapse of a bubble that is formed in the liquid [33]. Metallic nanoparticles of Au and Ag have been prepared by sonicating aqueous solutions of the corresponding metallic salts in the presence of a surfactant. Fe nanoparticles of 8 nm average size have been obtained by the sonolysis of $Fe(CO)_5$ in the presence of oleic acid [34]. The ultrasound reduction of aqueous solution of $PtCl_4^{2-}$ into colloidal Pt of 3 nm in diameter has also been reported [35]. The group reported that the presence of aliphatic alcohols increases the process of reduction. Apart from these Fe from $Fe(CO)_5$, Ni from $Ni(CO)_4$ and Co from the corresponding nitroso carbonyl have also been synthesised sonochemically [36-38]. Apart from metallic nanoparticles oxides like TiO_2 [39], CeO_2 [40] and mixed oxides like $LaNiO_3$ [41] and $LaSrMnO_3$ [42] have also been synthesized sonochemically.

1.2.4 Photochemical reduction

Huang and co workers reported the synthesis of Ag nanoparticles by irradiation of aqueous $AgNO_3$ solution with UV light of wavelength 243 nm in the presence of poly (N-vinylpyrrolidone)[PVP] as a stabilizer [43]. There have been lot of reports for the

radiation-assisted reduction of noble metal nanoparticles where γ-radiation has been used. Almost in all the cases the initial reaction product is either an $OH^{\bullet}$ or an $H^{\bullet}$ which are scavenged by some small molecules like alcohols which in turn they act as the reducing agents. The photochemical method finds great application particularly when 2 dissimilar metals are synthesized on top of the other forming a core-shell type of arrangement or when the system requires enlargement of colloidal metal nanoparticles. Metallic nanoparticles of 2 nm size of Au, 2-4 nm of Co and 20-100 nm of Cu have been synthesised by this process. Core-shell nanocomposites of $Au_{core}Pt_{shell}$, $Au_{core}Ag_{shell}$, $Au_{core}Pb_{shell}$, and $Au_{core}Hg_{shell}$ have also been prepared by this method [44-47]. Yang and coworkers have reported that photochemical reduction of choloroaurate ions in the presence of a small amount of Ag ions is responsible for the formation of anisotropic gold nanorods [48].

1.2.5 Synthesis through Coprecipitation

1.2.5.1 From aqueous solution

In order to synthesise noble metal nanoparticles from aqueous solution, a suitable reducing agent should be present. The most common reducing agents are gaseous H_2, aqueous $NaBH_4$, Hydrazine hydrate ($N_2H_4.H_2O$) and Hydrazine dihydrochloride ($N_2H_4.2HCl$). The E_0 value for the electrochemical half cell reaction for borohydride reduction is –0.481 V and for hydrazine reduction is –0.23 V, hence any metal having a E_0 value more positive than the above 2 values would be reduced. Thus, Au, Pt, Co, Ni and Ag nanoparticles have been formed via use of these reducing agents and suitable stabilizers like CTAB, SDS etc [49-53]. Apart from these, Turkevich and group in 1951 have shown that gold colloids can be synthesised by boiling a solution containing $HAuCl_4$ and sodium citrate [54]. However, it has been observed that when thiols are used as the stabilizing agents, stronger reducing agents like $NaBH_4$ are required since the complex of $AuCl_4^-$ and thiol is too stable to be reduced by weaker reducing agents like citrate.

1.2.5.2 From nonaqueous solution

One of the most noteworthy works of synthesis of gold colloids in nonaqueous medium is of Brust and coworkers where they involved a two-phase reaction mixture system for the reduction of gold [55]. The aqueous $AuCl_4^-$ ions were phase transferred into the organic toluene medium by use of a tertiary ammonium salt (tetra octyl ammonium bromide). Gold nanoparticles were then subsequently formed in the organic medium by addition of aqueous $NaBH_4$ in the presence of dodecanethiol. The reaction thus involved 3 different steps a) phase transfer of aqueous ions into the organic phase, b) reduction and c) capping of the formed nanoparticles. This reaction activated various researchers to make progress in selecting various capping agents in order to control the size and shape of the nanoparticles. Sastry and coworkers condensed this 3-step process into a single step process whereby a multifunctional molecule hexadecylaniline (HDA) was used as a phase transfer catalyst, reducing and a capping agent [56]. They have even shown that the size of the nanoparticles in the organic phase can be modulated by changing the $HAuCl_4$: HDA molar ratio.

1.2.6 Self-Assembled Monolayers (SAMs) and Langmuir-Blodgett technique

SAMs are ordered molecular assemblies formed by the adsorption of a surfactant onto a solid surface. The simplicity involved in the SAMs offer unique opportunities to have a better understanding on self-organizing, interfacial phenomena and also on the interactions between the surfactant and the substrate surface. Self-assembled monolayers (SAM) of organic bifunctional molecules on gold or aluminium substrates with terminal thiol groups have been widely prepared. Alivisatos and coworkers [57] were the first to show the capability of 2D SAM of 1,6 hexanedithiol, formed on gold thin film in organization of CdS nanoparticles through covalent interactions. In another approach they have shown that carboxylic acid derivatized CdS nanoparticles can also be arranged on aluminium thin film [57]. The self-assembly in this case occurs through electrostatic interaction of the free carboxylic groups on the CdS surface with the aluminium atoms on the surface of the substrate [57]. Similar strategy has been extended by Sastry and co-workers for the organization of silver nanoparticles on 2D SAMs of aromatic bifunctional molecules such as 4-CTP and 4-ATP on both gold and aluminium thin film surfaces

using covalent and electrostatic interactions respectively [58]. It is now possible to assemble small and more complex inorganic ions such as polyoxometallates (Keggin salts) [59, 60] and biomacromolecules such as proteins/enzymes [61,62] and DNA [63,64] at the air-water interface.

Although the assembly of amphiphilic monolayers onto air-water interface dates back to Babylonian times [65], Pockels [66] and Langmuir [67] laid the foundation work for the better understanding of organizational capability at the air-water interface. In order to form a 2D array of close-packed nanoparticles, the first step needed is the surface modification of the nanoparticles to render them hydrophobic and soluble in non-polar organic solvents. Once this step is over by use of an appropriate capping agent, they are then dispersed in the organic solvent and spread onto the surface of water. On evaporation of the solvent the nanoparticles self-assemble and the monolayers formed after compression can then be transferred to suitable solid substrates. There has been a lot of reports where surfactant-stabilized hydrophobic silver [68], CdS [69], magnetite [70] and ferroelectric lead zirconium titanate nanoparticles [71] could be spread on the surface of water and thereafter transferred as close-packed nanoparticle multilayers by the LB method, which lead to the development of an extremely simple and elegant method for the organization of nanoparticles at the air-water interface. Polymer latex spheres, zeolite and silica particles of different sizes have also been transferred onto solid substrates by use of the LB technique [72, 73]. Apart from these it has been shown by Sastry and co workers that flat gold nanoribbons can be formed by the reduction of $HAuCl_4$ at the subphase by HDA Langmuir monolayers in a constrained environment [74a]. Tyrosine reduced octadecylamine capped silver nanoparticles have also been assembled into highly ordered linear superstructures and transferred onto supports by this method [74b]. Thus synergistic interactions between the self-organizing particles at different layers or in some cases with the template lead to the development of hierarchically ordered nanostructures. The following section thus deals with nanostructures, its various form and type of synthesis.

1.3 Nanostructures-definition, synthesis and their various facets

Nanostructures are defined based on their geometrical considerations as is shown in the schematic of Figure 1.2 [75]. When the mobility of the electrons can be confined in two dimensions, then we have reached 2D nanostructures or "quantum-well". One-dimensional quantum confinement results in 1D nanostructures or "quantum/ nano wires" whereas zero-dimensional confinement leads to quantum dots. The anisotropy inherently present in the 0D and 1D systems have gathered considerable amount of interest resulting in unique properties and potential applications [76, 77] of such materials in nanodevices. However, as of today there exists no general strategy for the synthesis of such low-dimensional systems. 1D nanostructures have been christened with a variety of names such as nanowires, nanorods, nanowhiskers, nanofibres and so on.

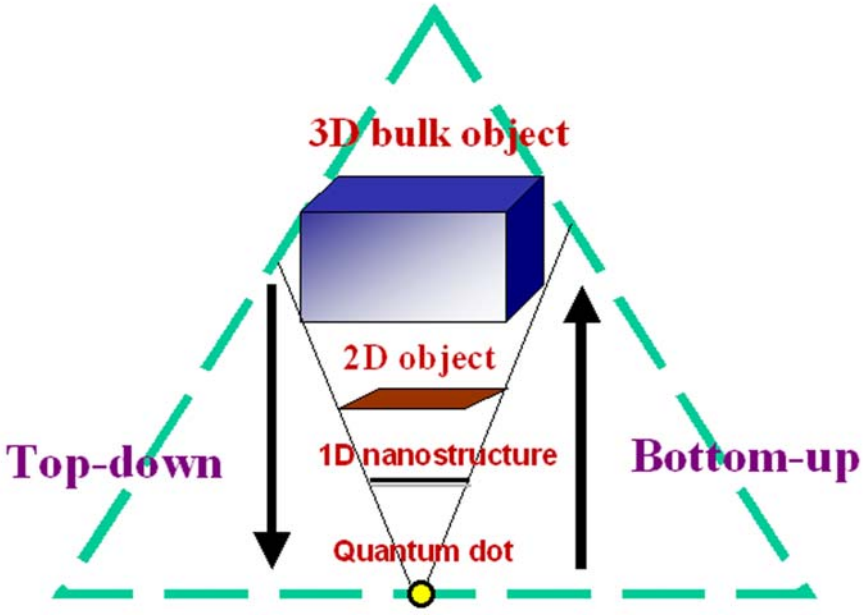

Figure 1.2: *Cartoon showing the length scales of various structures.*

Growth of 2D nanostructures has primarily been through deposition of thin films, which includes molecular beam epitaxy [78], sputtering [79], chemical vapour deposition [80], Langmuir-Blodgett films [81] and Self-Assembled Monolayers (SAMs) [82]. Thus, keeping in mind the applicability of these low-dimensional systems, a brief overview of the synthesis of 1D nanostructures will be covered in the following sections.

1.3.1 Vapour-liquid-solid or Solid-liquid-solid (VLS or SLS) growth

In this method, a second phase material, usually referred to as a catalyst or impurity is introduced onto a solid substrate at a particular temperature and at a particular orientation. Wagner and Ellis first proposed the VLS theory of growth of Silicon whiskers on gold substrates [83]. In earlier studies of growth of Si nanowires, liquid gold droplets were used as the catalyst material at a temperature of 500 ^{0}C. Here, one needs to have a prior knowledge of the equilibrium phase diagrams in order to choose a catalyst. After this, one should check the particular eutectic temperature at which there is a coexistence of the liquid alloy and the solid nanowire. Thus, in this case the Si vapour usually obtained by degrading diphenylsilane preferentially dissolves into the Au droplet forming the eutectic alloy. As the reaction proceeds the Si grows into a wire by continuous addition at the nucleation centre. However, in this case the diameter of the nanowire formed would be limited by the diameter of the liquid drop used which is roughly of 100 nm. Following this method, several types of nanowires like Si, Ge, GaN, GaAs, InP, CdS etc. nanowires have been prepared [84]. The nanowires formed are generally polycrystalline, amorphous or single crystals depending on the substrate and growth conditions.

1.3.2 Template-based synthesis

This is one of the most common methods of synthesis for the fabrication of nanorods, nanowires, nanotubes using a host of template, which are discussed in the following sections.

1.3.2.1 Porous alumina membrane

The anodic alumina membrane is a very promising hard template due to its regular and ordered structure. The membrane is prepared by a two-step aluminium anodic oxidation process, which results in the formation of hexagonally ordered pores of a particular diameter [85]. One interesting feature of this formed membrane is that the pore diameter can be altered by several techniques like treatment with agents like H_3PO_4 or simply by varying the potential in oxalic acid medium [86]. Generally before mounting into the electrochemical cell the porous alumina membrane is ultrasonically agitated in

deionised water in order to free the surface of unwanted coating or pollutant. The metallic nanowires like Ag, Sn [87] are then deposited into these nanopores by a three-electrode direct current method and in the presence of the corresponding electrolytes at room temperature. In the case of formation of Ag nanowires, they grew in (220) direction as opposed to the bulk (111) direction, which shows that this method helps in the growth in a particular orientation [88]. Hence, this is one of the most general methods that have been used to develop several conducting polymers [89] and semiconductors [90] also.

1.3.2.2 Double hydrophilic block copolymer (DHBC)

Although silver nanowires have been grown by DHBCs [91], yet there has been a lot of interest in the growth of mineral crystals by use of these DHBCs. This is because that the designs found in nature and the way organisms have utilised their own structures for survival have inspired many contemporary researchers to mimic them and grow similar mineral crystals at room temperature. In that respect, double-hydrophilic block coplymers have been the most effective template for the synthesis of various mineral crystals like $CaCO_3$ [92], $BaSO_4$ [93] and so on. Block copolymers can be treated as low molecular weight surfactants and usually consist of a hydrophilic and a hydrophobic block. A schematic of the function of a DHBC is shown in Figure 1.3.

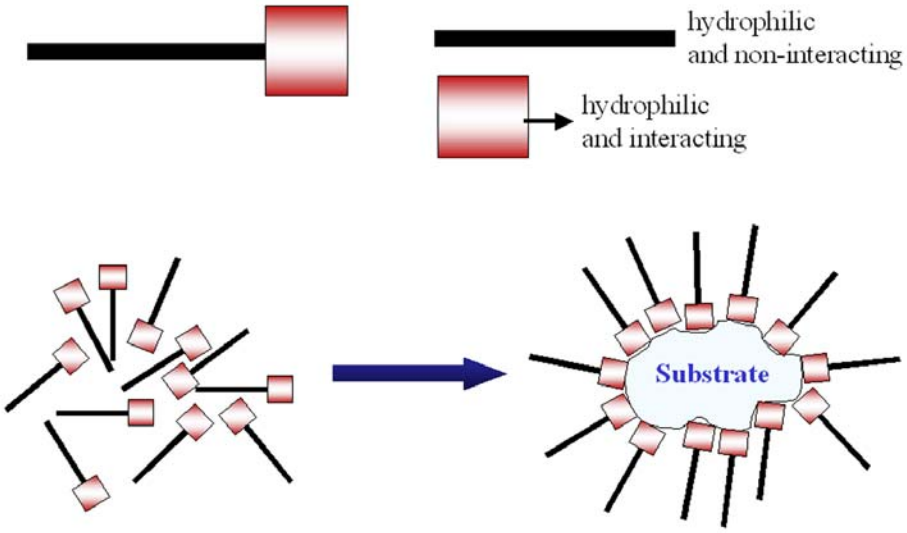

Figure 1.3: *Cartoon of the function of a double hydrophilic block copolymer (Ref: Cőlfen, H. Macromol. Rapid Commun.* ***2001****, 22, 219.)*

A double hydrophilic copolymer is thus a diblock copolymer which has two hydrophilic blocks but of different chemical nature. Very often, one of the blocks induces solubilisation whereas the other block interacts with the surface. These DHBCs behave as switchable amphiphiles as the molecules start interacting upon meeting a substrate like a mineral surface [94]. Thus, in most of the cases silver nanowires are formed by the interaction of a –COOH group carried by one of the block polymer whereas the other does not interact at all [95]. These have far-reaching applications that include gene therapy [96], drug carrier systems and crystal growth modifiers [97].

1.3.2.3 Lithography techniques

This is one of the primary " top-down" approaches for the synthesis and assembly of one-dimensional nanostructures. It was discovered during the end of the 18^{th} century when Alois Senefelder of Munich sketched his design on a porous stone with a greasy substance. The design area repelled the solution mixture containing gum Arabic and water used for wetting the surface whereas the stone areas absorbed it. Thus, a clean impression of the design was obtained when a sheet of paper was pressed against it [98]. Photolitography and electron-beam lithography have been widely used for the patterning of larger dimensions and also for dimensions less than 50 nm respectively [99]. Using Dip-Pen Lithography (DPN) various organic [100], semiconducting [101] and metallic [102] materials have been obtained. This process uses an Atomic Force Microscope (AFM) tip wetted with "ink" onto a surface suitable for fabricating patterns. However, one drawback of the Lithography technique is that there is a loss of control over the surface patterns once the features are further miniaturized.

1.3.2.4 Biological templates

Due to the basic interacting capability of the base pairs, DNA has been effectively used to assemble metal nanoparticles like Au [103], Ag [104], Pt [105], Pd [106] and even Cu [107]. There are standard procedures for the construction of DNA network where in most of the cases λ-DNA solution is coated onto funtionalised mica [108]. Metal nanoparticles are thus formed on the DNA network by the reduction of the corresponding salt with $NaBH_4$. The formation of the nanorods and nanowires largely

depend on the density of the DNA network, which in turn depends on the concentration of DNA used. DNA has a diameter of c.a. 2 nm and a variable length; hence organization of nanoparticles onto the DNA backbone has often resulted in the formation of one-dimensional nanowires. However, this process lacks the control of growth of the higher-order superstructures. There have also been reports of formation of Ag nanoparticles by photoreduction of the DNA-Ag^+ complex with UV light at 254 nm [109]. In another case gold nanowires have been assembled using DNA by attaching it to conventionally patterned gold contacts on a Si substrate [110]. Virus stands for yet another beautiful natural example of self-assembly of which tobacco mosaic virus (TMV) has been extensively dealt with. TMV contains as many as 2130 identical proteins assembled around a single strand of RNA as a coat, giving it a size-length of 300 nm and an external and internal diameter of 18 nm and 4 nm respectively. The self-assembly is highly specific and uses non-covalent interactions [111]. The outer surface of the TMV predominantly contains a significant no. of lysine and arginine moieties whereas the interior surface contains more of glutamic and aspartic acid. Thus selective adsorption and consequent reduction of anionic metal precursors can be preferentially done at the outer surface at pH~ 3, since at this pH, only the outer surface will be protonated. Thus using these various properties nanotubular assemblies of Au, Pt, Ni, Pb and CdS have been obtained [112].

1.4 Moving onto hybrid organic-inorganic nanostructures

In addition to hybrid inorganic templates, organic-inorganic hybrid compounds have attracted increasing interest in recent years due to the possibility of combining the different characteristics of the components to get unusual structures, properties and applications. As discussed in an earlier note that the sol-gel process has been one of the most general methods for the synthesis of inorganic-organic hybrid composites. In this process, various ceramic materials like SiO_2, TiO_2 etc. with high purity can be obtained by simple hydrolysis of organo-silicates and organo-tungstates. Another advantage of this method is that the temperatures involved here are relatively low when compared to melting of typical ceramics. One important property of these hybrid structures is that the stiffness of these materials increases with incorporation of the inorganic material into the

organic matrix [113]. To justify this, the most suitable example is bone, which is 10 times tougher than the individual collagen fibres. This is due to the strengthening by a few nanometers thickness of calcium hydroxyapatite crystals. Thus, there have been reports of usage of crystalline polymer matrix instead of an amorphous polymer to control the morphology of the particles where submicron sized TiO_2 particles in the polypropylene-TiO_2 composites were obtained. Several inorganic materials or additives have been added to polymers to form hybrid organic-inorganic microstructures. Clay is one of them which contains layers of silicates that undergo homogeneous intercalation with the organic molecules at the microscopic level [114], which was shown by Toyota researchers. The positively charged polymer (Nylon 6, polycaprolactam) ends bind with the negatively charged silicates through electrovalent bond and exhibit mechanical properties far superior to the unfilled polymers or other composites.

1.5 Synthesis of anisotropic nanostructures

As discussed previously, one of the reasons behind the intense study of metal nanoparticles during the last decade has been due to their unusual physicochemical and optoelectronic properties. While particle size is an important factor in controlling the optical [1] and chemical properties of nanoscale matter [115], it is also recognized that the shape of nanoparticles adds an additional degree of freedom in modulating these properties [116]. Tuning the properties such as particle size and shape by use of suitable reducing agents has resulted in the production of various shapes such as rods [117], wires [118], nanoplates [119-121], nanodisks [122-124] and nanoprisms [125-128] possessing significant anisotropy. The fate of the surface plasmons occur either in a radiative manner where the plasmons get transformed into photons or through a non-radiative manner [129]. A decrease in the damping of the decay time augments applications of surface plasmons for Surface Enhanced Raman Spectroscopy (SERS). Thus anisotropic nanoparticles in addition to the absorption in the Near Infra-red (NIR, longitudinal component) region, show an enhanced optical nonlinearity [130] and a decrease in the plasmon relaxation time [129]. Although a large number of reports exist in the literature for synthesis of monodisperse gold nanoparticles, few deal with the synthesis of anisotropic gold nanoparticles. Anisotropy has thus been achieved either through

photochemical reduction [127, 131-133] or by thermal methods [121]. Apart from these, sonochemical assisted synthesis [134] and microwave irradiation [135] techniques have also been used for the synthesis of 2D silver nanoplates. In fact, one of the best procedures for obtaining control over the shape of the nanoparticles is by using a template, which includes hard templates like porous alumina [136], polycarbonate membranes [137], carbon nanotubes [138] and soft templates like micelles [139, 20].

In one of the reports, Prof. Murphy has shown that shape control of nanoparticles can be achieved by seed mediated growth in the presence of a micelle [140]. For the synthesis of gold nanorods the process involved 2 basic steps, a) first spherical gold nanoparticles were obtained by usual sodium borohydride reduction and b) arrested growth of the nanoparticles in a rod like micellar environment was achieved by the use of Ag^+ ion acting as the inhibitor. With increase in the concentration of the seed there has been a concomitant shift in the position of longitudinal part of the plasmon band of gold nanoparticles which is characteristic of shape anisotropy (here nanorods). In addition to this growth of Au nanorods have also been achieved by ion irradiation into a core-shell structure of $Au@SiO_2$ [141]. By irradiating ensembles of these particles having various core-shell diameters it was possible to obtain arrays of gold nanorods. Much work has also been carried out on the anisotropic growth of silver nanodisks and nanoprisms. Examples of methods like seed-mediated CTAB-directed growth of silver nanoplates [119], template-mediated synthesis of silver nanodisks using polystyrene [122] have been in use. Silver nanodisks were also formed by sonicating silver ions and hydrazine dissolved in reverse micelles consisting of bis (2-ethyl-hexyl)sulfosuccinate (AOT), isooctane, and water [123] Furthermore, it was demonstrated that silver nanoprisms could be synthesized by boiling silver nitrate dissolved in *N*,*N*-dimethyl formamide that contained a polymer such as poly(vinyl pyrrolidone) (PVP) [125]. Thermal transformation of silver colloids into sharp edged triangular nanoplates has also been carried out [121].

Thus, it has become quite comprehensible that synthesis of anisotropic nanostructures has been the centre of attention for researchers for a long time. Apart from the existing innumerable chemical methods, Sastry and coworkers have developed indigenously the role of agents of biological origin to develop anisotropic nanostructures

and indeed the anisotropy has been recognized for potential industrial applications. The moment one speaks of structures of biological origin, that opens up a wide area of crystal growth and mineralization. Crystals, one of the things that have mesmerized mankind most, have evolved in nature for years through volcanic eruptions, weathering of rocks, and so on. The moment biology gets attached to the engineering of mineral crystals, be it a microorganism or a herb, researchers term it scientifically as " Biomineralization" and the inspiration to design/ mimic such structures to the microscopic level has come from none other than nature herself. Hence, a brief note shall be provided in the following section about the process of biomineralization.

1.6 Biomineralization: A different perspective

As the name suggests " biomineralization" signifies the synthesis of inorganic mineral crystals of purely biological origin. This is definitely one of the fields of study which has seen the marriage from inorganic chemistry, materials science, molecular biology, genetics and geology. Nature relies upon simple mineral crystals to systematically recreate a host of different complex life forms such as gastropods, coccoliths etc. Numerous environmental and biological phenomena like water turbulence, desiccation, predation have always threatened the life of inferior origin. Thus, these creatures like gastropods have come up with their own defence mechanism for survival. One such defence mechanism of mollusks is the secretion of calcium carbonate shell whereby the entire body can be protected inside the shell thereby closing the aperture and thus protecting the underlying soft tissues [142]. Some more examples include corals and diatoms, the structure of which is composed of calcium carbonate and silica respectively. Magnetotactic bacteria, which are known to navigate along the earth's magnetic field, contain fine magnetic nanoparticles as is evidenced from the images shown in Figure 1.4. Thus nature has created her own designs and has provided the organisms some mechanism for their survival.

Calcium carbonate ($CaCO_3$) is one of the most abundant biominerals found in nature. There are in total six polymorphs of $CaCO_3$ having typical morphologies: calcite (the most stable, though not necessarily the most common having a rhombohedral crystal structure), aragonite (the strongest and metastable; usually are needle shaped), and

vaterite (the highest energy configuration and unstable at room temperature; polycrystalline spheres) [143,144]. Calcite has trigonal/rhombohedral symmetry, aragonite has orthorhombic symmetry whereas vaterite has hexagonal symmetry. In addition to this three other forms- amorphous calcium carbonate (ACC), monohydrate and hexahydrate calcium carbonate are also known. Very few examples are known where the organism utilizes ACC in its entire lifetime.

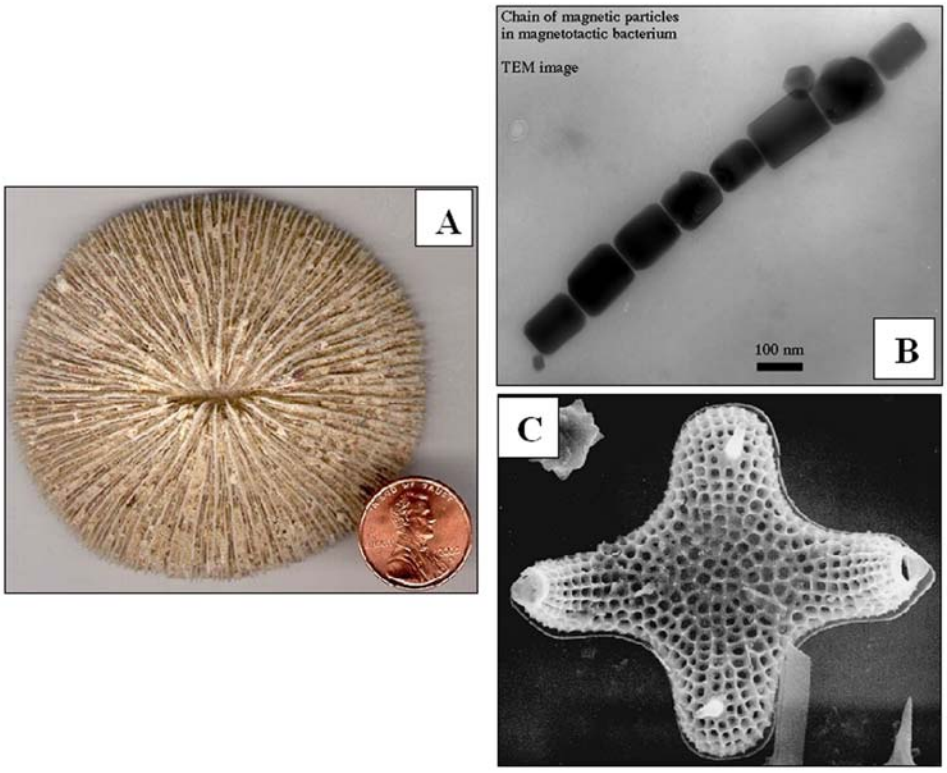

Figure 1.4: *Photographs (TEM and SEM) depicting the wonderful mineral forms present in A) corals, B) magnetotactic bacteria and C) diatoms. (Ref: http://www.ucmp.berkeley.edu/chromista/bacillariophyta.html and www.biophysics.uwa.edu.au respectively)*

However some of the crustaceans are believed to utilize ACC as the transient phase to crystalline calcite, which are present in their exoskeletons. Since ACC is unstable and dissolves rapidly in water, the cyclic usage of this phase in the cuticles (exoskeleton) along with large amounts of phosphorous proves to be advantageous [145]. There has been innumerable number of processes where $CaCO_3$ has been synthesized in the lab in order to recreate nature's design which will be further dealt in details in a later chapter.

Apart from calcium carbonate, another inorganic material, which has been of tremendous enthusiasm, is calcium hydroxyapatite or calcium phosphate [$Ca_{10}(PO_4)_6(OH)_2$; HAP]. This has been of importance as they form the main constituent of vertebrate bones and teeth along with collagen fibres [146]. The characteristics of apatite material are dependent on the size and shape of the particles, crystallinity and water [147], no wonder any deficiency of these lead to serious bone defects. The ideal Ca/ P ratio in bones is 1.67, however substitution of the divalent anions like CO_3^{2-} and HPO_4^{2-} for PO_4^{3-} result in the change of the ratio, which depends on the age, and bone site. Generally, it has been observed that the Ca/ P ratio increases with age suggesting increase of carbonate species. Thus keeping these points in mind this thesis in one later chapter will elaborate some very common recipes of biological origin for the synthesis of some mineral crystals.

1.7 The motivation behind this thesis work

As it was aptly said by Prof. Feynman that "There is still plenty of room at the bottom ", the work mentioned in this thesis is the inspiration of a variety of work carried out in our lab by Sastry and co workers. Since the last decade there have been various protocols for the synthesis of gold nanoparticles in aqueous as well as organic phase. Nanoparticles have also been assembled on a variety of substrates such as those provided by Langmuir Monolayers [148], surface modified polymers [149] and so on. It was shown by Sastry and co workers that benzene and anthracene in the organic phase binds strongly with gold nanoparticles at the interphase [150]. In the meantime we came across an inorganic molecule commonly known as "Keggin ions" (from the name of the inventor), which had unique properties like photoreduction. Thus, we exploited both the properties as mentioned above for the formation of truly constrained gold nanosheets at the organic-water interphase.

Keggin ions form a subset of polyoxometalates and have the general formula $(XM_{12}O_{40})^{(8-n)-}$, where 'M' stands for W or Mo and 'X' stands for heteroatoms such as P, Si, Ge with *n* being the valency of X [151]. The reactivity of the Keggin structure is governed by its electronic structure. On reduction they are generally coloured mainly

blue as is depicted from the Figure 1.5A, producing the so-called heteropoly blues (HPB), which have a broad absorption at - 700 nm and is characteristic of intervalent metal transition. Polyoxometallates are generally prepared by the condensation reaction occurring upon acidification of solutions of MoO_4^{2-} or WO_4^{2-} and form colourless solution. The structure has an overall T_d symmetry that is composed of a XO_4 tetrahedron surrounded by twelve MO_6 octahedra as is shown in the schematic of Figure 1.5 B and C. Reduction of polyoxometallates proceeds without substantial change of their structure with addition of a certain characteristic number of electrons.

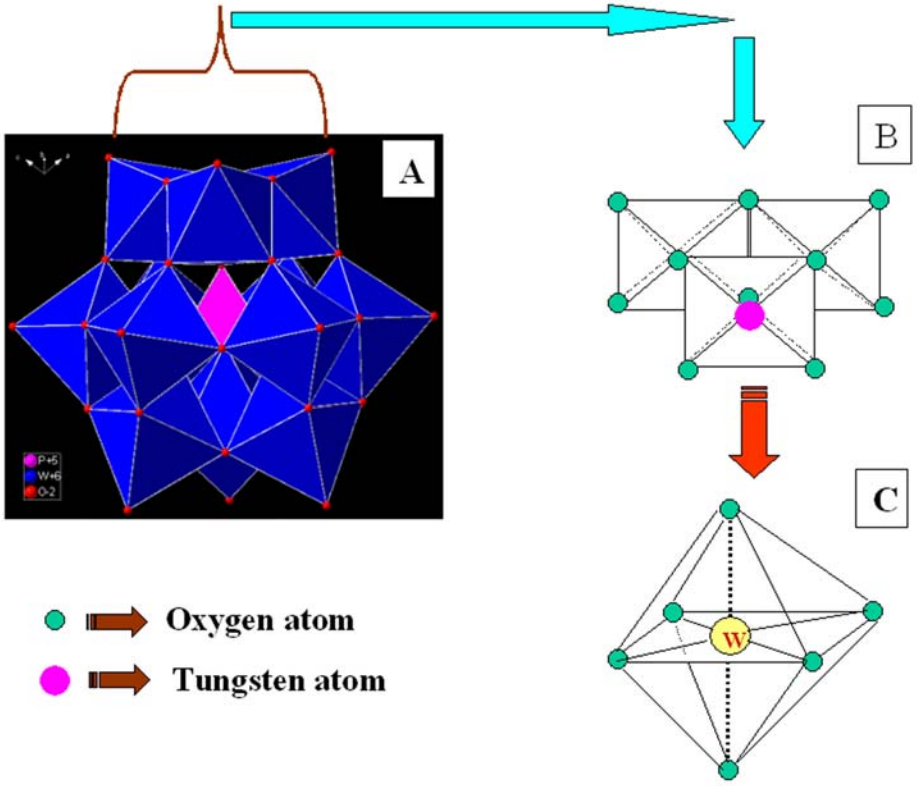

Figure 1.5: *A) A pictorial representation of Keggin ions. (Ref: http://www.liv.ac.uk/researchintelligence/graphics/15/catalysts_01.gif).*
B) Schematic showing the arrangement of one of the 4 WO_6 octahedron that are tetrahedrally arranged around PO_4 ion. C) A 3D schematic of the formation of WO_6 octahedron showing the presence of a central W atom and edge shared O atoms.

Berzelius in 1826 prepared phosphomolybdic acid [152], however, it was only in 1933 when *Keggin* reported the structure of this anion by analysis of 32 powder X-ray lines [153]. Keggin ions have a wide range of application, the earliest and the most widely

used as of today also is the gravimetric determination of elemental P or Si through the formation of heteropoly blues [154]. Substituted Keggin ions have also been used for the voltametric determination of Ga (III) ions [155]. They have been used as solid electrolytes for fuel cell applications and also as inorganic resist materials [156]. Apart from these applications in materials science, they bear anti-tumour, anti-viral and anti-bacterial nature that serve for the preparation of an inorganic drug [157]. Since most of these polyoxoanions have d^0 configuration for the central metal atom, hence they should behave as non-magnetic, however some molecules like polyoxovanadates (IV) with their very large clusters behave as tiny magnets [158]. Phosphotungstic acid-based membranes have been directly used for application in methanol-fuel cells [159]. The first contrary to the original d^0 "closed frame" structure of the Keggin ion was reported by Bino and group who showed that by incorporation of Fe ion they formed an "open-shell" structure [160]. Very often biological samples like bacterial cell walls are stained with phosphotungstic acid to be able to be viewed under a high voltage electron microscope [161].

Since these Keggin ions bear a high negative charge, they can electrostatically bind with positive metal ions. They combine with Ca^{2+} ions to form a complex which subsequently form star-shaped calcium carbonate crystals [162]. We have even shown that Ag^{+}- Keggin composite structure can be used for the growth of silver assemblies [163]. Core-shell nanostructures have also been achieved using Keggin ion as the UV-switchable reducing agent [164]. Thus, with this prior knowledge we made an attempt to study the interaction of amino-acids with Keggin ions. Since at the pH of the Keggin ions (pH~ 2.5-3) most of the amino acids will be protonated and hence should interact with the Keggin ion. Phosphomolybdates are reduced easily than the corresponding tungstates [165], hence our trial in the same experiment with the Phosphomolybdates led to a completely different result altogether.

As mentioned earlier in a previous note, crystal growth and biomineralization is another area which has engrossed researchers for quite sometime. Sastry and co workers have shown in the recent past that nanoparticles [166], semiconductors [167] and minerals [168] can be synthesised by use of eukaryotic organisms like fungi. This piece of work has been totally enthralling as the properties of the materials formed are

completely dictated by the enzymatic effect of the microorganisms. The simplicity as well as the efficiency of this method made us look further in this direction by using the synthesis of mineral crystals of heavy metal ions as a technique for bioremediation. We even made attempts to mimic such mineral growth by use of plant extracts and seeds. We have been able to identify the nature of the dominant protein, which is responsible for the growth of such mineral structures, and are yet at the primary stage to ascertain the exact mechanism taking place for the formation of such complex superstructures.

1.8 Chapter-wise description of work carried out in this thesis

The work carried out in this thesis lays emphasis on the use of different organic-inorganic hybrid structures to obtain flat nanostructures of gold. We have made an attempt to synthesise and assemble metal nanoparticles onto the Keggin-amino acid template which forms fibre-kind of structures. Stress has also been given on the methods to form various anisotropic nanostructures. The protocol mentioned for the formation of anisotropic nanostructures is entirely different from the existing modes of preparation. Finally we have shown methods of purely biological origin for the growth of mineral crystals at room temperature. The exquisite morphology that has evolved from these methods has strengthened our belief in the underlying potential of the nature, be it a plant extract or a microorganism.

The thesis consists of six chapters. ***Chapter I*** is an introduction to the thesis and gives a brief review about the formation of nanoparticles with some processes for their formation and stability, then moving on to 2D and 1D hybrid nanostructures and subsequent assembly of nanoparticles on these structures. The chapter also briefly discusses our protocols for synthesizing different nanocomposites.

Chapter II describes the experimental characterization techniques that have been used for the characterization of the work. UV-visible Spectroscopy, Fourier Transform Infrared Spectroscopy (FTIR), Transmission Electron Microscopy (TEM), Scanning Electron Microscopy (SEM), X-Ray Diffraction (XRD), Energy Dispersive Analysis of X-ray (EDAX), Atomic Force Microscopy (AFM), X-Ray photoemission spectroscopy (XPS) and conductivity measurements are some of the techniques which have been extensively used to justify the formation of nanoparticles. Isothermal Titration

Calorimetry (ITC) has also been used to quantitatively study the formation of nanocomposites. To have an idea of the proteins present in the biocomposites, SDS-Polyelectrolyte Gel Electrophoresis (PAGE) has also been carried out. The physical principles on which the different techniques are based and their application to understanding the various aspects of formation of the nanocomposites has been delineated.

Chapter III discusses the synthesis of flat nanosheets of gold and platinum at the liquid-liquid interface using photochemically charged Keggin ions. Anthracene is the smallest unsubstituted aromatic hydrocarbon with a positive electron affinity (0.53 eV) and can exist in a stable valence anion state [169]. This suggests that conceptually it is possible that anthracene can accept electrons and stay in its excited state leading to the formation of anthracene anions. Here we have accomplished facile electron transfer to anthracene molecules present in an organic phase by exposure to photochemically reduced Keggin ions. Addition of this organic phase to an equimolar solution of chloroauric acid resulted in the formation of flat sheets of gold at the interface. The thickness of the gold nanosheets has been shown to be very thin, since the reducing surface is truly two-dimensional as was very similar to that obtained by Dr. Sastry's group during the reduction of gold ions at the hexadecylaniline Langmuir monolayers. Similar reaction carried out in the presence of chloroplatinic acid resulted in the formation of rings of platinum at the liquid-liquid interface. The thin films were cast onto carbon-coated copper grids and glass slides and were characterized by Transmission Electron Microscope (TEM) and X-ray Diffraction (XRD) measurements respectively. In a very similar approach 2D nanosheets were obtained at the liquid-liquid interface containing Keggin ions and $HAuCl_4$ in the aqueous medium and octadecylamine in an organic medium. Preferential electrostatic binding at the interface resulted in the formation of a constrained environment leading to thin sheets of gold along with spherical gold nanoparticles. This strategy opens up an exciting methodology of synthesizing flat nanostructures at the liquid-liquid interface.

Chapter IV discusses the programmed assembly of nanomaterials using various organic-inorganic hybrid superstructures. Nanotectonics is one such term that collectively describes the assembly of various inorganic nanoparticles into materials having higher

order architecture. We show in this chapter that the amino acid lysine can electrostatically combine with Keggin ions (a class of polyoxometallates) to result in cross-fibre like hybrid superstructures. These fibres then have been used for the assembly of gold nanoparticles by utilizing the UV-switchable reducing property of Keggin ions. It has also been shown that similar results are obtained for the assembly of silver nanoparticles when arginine is used as the amino acid. We have tried to extend this protocol to other polyoxometallates wherein phosphomolybdic acid-lysine composite was used to reduce chloroauric acid. This resulted in the growth of anisotropic gold nanoparticles. However, when the same reaction was carried out in a dialysis bag similar structures were not formed, which ascertained that lysine is the shape-modulating agent in our procedure.

Chapter V describes some biological processes for the synthesis of inorganic mineral crystals. Earlier in this group, it has been shown that microorganisms in a fixed environment may be used to synthesize mineral crystals via a truly biogenic pathway. As a continuation this novel protocol, we have shown that microorganisms like fungi sustained the toxic environment and the detoxification of heavy metal ions like Cd^{2+} and Pb^{2+} occurred by a process of metal carbonate formation. A thorough examination of the mineral crystals by Scanning Electron Microscopy (SEM) indicated that the morphology of the metal carbonates of Ca, Cd and Pb were mainly governed by proteins present in the reaction medium. That the source of CO_2 is the fungus grows makes this process a truly biomimetic one. In a very similar approach, polymorph selectivity of metal carbonates was accomplished by the reaction of aqueous solution of metal ions with germinating chickpea seeds. The germinating seeds release CO_2 into an aqueous solution of $CaCl_2$ transforming it into vaterite, an unstable form of $CaCO_3$. In a different set of experiment we tried to grow mineral crystals using plant extract, traditionally known to heal bone fractures. In this work, we have analyzed the extract of the stem of *Cissus quadrangularis* from the point of view of its putative ability to promote mineral growth. CO_2 was allowed to pass into the stem extract of *Cissus quadrangularis* which resulted in the formation of phase pure calcite crystals. The plant contains a high percentage of calcium probably due to its thick cell wall, which makes it very suitable for growth of mineral crystals. The presence of phosphorous in the plant can also be exploited for synthesizing

hydroxyapatite, thus utilizing the traditional knowledge of bone-fracture healing in advanced technique of new material synthesis.

Chapter VI summarizes the work presented in the thesis and looks towards further work in this area of research. The protocols developed by us have been compared with reference to other protocols currently in trend, and the pros and cons have been brought out.

1.9 References

[1] El-Sayed, M. A. *Acc. Chem. Res.* **2001**, *34,* 257.

[2] http://www.physics.usyd.edu.au/ugrad/tsp/talks/2005/LaurieField.pdf

[3] Scho¨ n, G.; Simon, U. *Colloid Polym. Sci.* **1995**, *273*, 202.

[4] Hirai, H.; Wakabayashi, H.; Komiyama, M. *Chem. Lett.* **1983**, 1047.

[5] Burin, A. L.; Cao, H.; Schatz, G. C.; Ratner, M. A. *JOSA B* **2004**, 21, 121.

[6] Hans M.L.; Lowman A.M. *Current Opinion in Solid State and Material Science* **2002**, *6*, 319

[7] Charles, S. C.; Popplewell, J. In Ferromagnetic Materials; Wohlharth, E. P., Ed.; North-Holland: Amersterdam, 1980; Vol. 2.

[8] Thomas, J. M. *Pure Appl. Chem.* **1988**, *60*, 1517.

[9] Mie, G. *Ann. Phys* **1908**, *25*, 377

[10] Pashley, R. M.; Karaman, E. M. *Applied Colloid and Surface Chemistry* John Wiley & Sons, Ltd **2004**, pg. 141.

[11] Koch, C.C. *Adv. Mater. Sc.* **2003**, *5*, 99.

[12] Li, J.; Lu, C.; Maynor, B.; Huang, S.; Liu, J. *Chem. Mater*. **2004**, 16, 1633.

[13] Stellacci, F.; Bauer, C.A.; Meyer-Friedrichsen, T.; Wenseleers, W.; Alain, V.; Kuebler, S.M.; Pond, S.J.K.; Zhang, Y.; Marder, S.R.; Perry, J.W. *Adv. Mater.* **2002**, *14,*194.

[14] Liu, C.; Zou, B.; Rondinone, A. J.; Zhang, Z.J. *J. Am. Chem. Soc.* **2001**, *123,* 4344.

[15] Chen , J.-F.; Wang, Y.-H.; Guo, F.; Wang, Xin-Ming; Zheng, C. *Ind. Eng.*

Chem. Res. **2000**, *39,* 948.

[16] Motte, L.; Billoudet, JJ F.; Pileni, M. P. *J. Phys. Chem.* **1995***, 99,* 16425.

[17] (a) Bunker, C. E.; Harruff, B. A.; Pathak, P.; Payzant, A.; Allard, L. F.; Sun, Y.-P. *Langmuir* **2004,** *20,* 5642. (b) Garcia-Martinez, J. C.; Scott, Robert W. J.; Crooks, Richard M. *J.Am.Chem.Soc***. 2003**, *125*, 11190.

[18] Zhang, S. *Nature Biotech.* **2003**, *21*, 1171.

[19] Tanev, P. T.; Chibwe, M.; Pinnavaia, T. J. *Nature* **1994**, *368*, 321.

[20] Jun, Y. N.; Dabbs, D. M.; Aksay, I. A.; Erramilli, S. *Langmuir* 1994, *10*, 3377.

[21] Buining, P. A.; Liz-Marzan, L. M.; Philipse, A. P. *J. Colloid Interface Sci.* **1996**, *179***,** 318.

[22] Zhang, L.; Coffer, J. L. *Chem. Mater.* **1997,** *9,* 2249.

[23] Palkar, V.R. *Nanostruc. Mater.* **1999**, *11*, 369.

[24] Hernandez, B. A.; Chang, Ki-Seog; Fisher, E. R.; Dorhout, P. K. *Chem. Mater.* **2002,** *14,* 480.

[25] Sharma, Pramod K.; Varadan, V. V.; Varadan, V. K. *Chem. Mater.* **2000,** *12,* 2590.

[26] Hoar, T. P.; Schulman, J. H. *Nature* **1943**, *152*, 102.

[27] Boutonnet, M.; Kizling, J.; Stenius, P.; Maire, G. *Colloids Surf.* **1982**, *5*, 209.

[28] Liu, C.; Rondinone, A. J.; Zhang, Z. J. *Pure Appl. Chem.* **2000**, *72*, 37.

[29] O'Connor, C. J.; Seip, C. T.; Carpenter, E. E.; Li, S.; John, V. T. *Nanostruct. Mater.* **1999**, *12*, 65.

[30] Pang, Y.-X.; Bao, X. *J. Mater. Chem.* **2002**, *12*, 3699.

[31] Song, K. C.; Kim, J. H. *Powder Technol.* **2000**, *107*, 268.

[32] Moulik, S. P.; De, G. C.; Panda, A. K.; Bhowmik, B. B.; Das, A. R. *Langmuir* **1999,** *15,* 8361.

[33] The Chemistry of Nanomaterials: Synthesis, Properties and Applications Volume 1 ed. By C.N.R. Rao, A. Muller, A.K. Cheetham published by Wiley-VCH GmbH & Co. 2004 Page 114.

[34] Suslick, K. S.; Fang, M.; Hyeon, T. *J. Am. Chem. Soc.* **1996**, *118*, 11960.

[35] Mizukoshi, Y.; Oshima, R.; Maeda, Y.; Nagata, Y. *Langmuir* **1999**, *15*, 2733.

[36] Grinstaff, M.W.; Cichowlas, A.A.; Choe,S. B.; Suslick, K. S. *Ultrasonics* **1992***, 30*,

168.

[37] Koltypin, Yu.; Katabi, G.; Cao, X.; Prozorov, R.; Gedanken, A. *J. Non Cryst. Solids* **1996**, *201*,159.

[38] Suslick, K.S.; Fang, M.; Hyeon, M.T.; Cichowlas, A.A. *Mater. Res. Soc. Symp. Proc.*, **1994***, 351*, 443.

[39] Zhu, Y.; Li, H.; Koltypin, Y.; Hacohen, Y. R.; Gedanken, A. *Chem Commun*., **2001**, 2616.

[40] Kumar, E. V.; Mastai, Y.; Gedanken, A. *Chem. Mater.* **2000**, *12*, 3892.

[41] Jeevanandam, P.; Koltypin, Y.; Gedanken, A. *Nano Lett.* **2001**, *1*, 263.

[42] Xia, X.; Shen, L.L.; Guo, J. P. et.al. *J. Nanosci. Nanotechnol,* **2002**, *2,* 45.

[43] Huang, H. H.; Ni, X. P.; Loy, G. L.; Chew, C. H.; Tan, K. L.; Loh, F. C.; Deng, J. F.; Xu, G. Q. *Langmuir* **1996**, *12*, 909.

[44] Henglein, A. *J. Phys. Chem. B.* **2000**, *104*, 2201.

[45] Mandal, S.; Selvakannan, PR.; Pasricha, R.; Sastry, M. *J. Am. Chem. Soc.***2003,** *125*, 8440.

[46] Mulvaney, P.; Giersig, M.; Henglein, A. *J. Phys. Chem.* **1992**, *96*, 10419.

[47] Henglein, A.; Giersig, M. *J. Phys. Chem. B*. **2000**, *104*, 5056.

[48] Kim, F.; Song, J. H.; Yang, P. *J. Am. Chem. Soc.* **2002,** *124*, 14316.

[49] Yonezawa, T.; Sutoh, M.; Kunitake, T. *Chem. Lett.* **1997**, 619.

[50] Tan, Y.; Dai, X.; Li, Y.; Zhu, D. *J. Mater. Chem.* **2003**, *13*, 1069.

[51] Gui, Z.; Fan, R.; Mo, W.; Chen, X.; Yang, L.; Hu, Y. *Mater. Res.Bull.* **2003**, *38*, 169.

[52] Chen, D.-H.; Hsieh, C.-H. *J. Mater.Chem.* **2002**, *12*, 2412.

[53] Sondi, I.; Goia, D. V.; Matijevic, E. *J. Colloid Interface Sci.* **2003**, *260*, 75.

[54] Turkevich, J.; Stevenson, P. S.; Hillier, J. *Discuss. Faraday Soc.* **1951**, *11*, 58.

[55] Brust, M.; Walker, M.; Bethell, D.; Schiffrin, D. J.; Whyman, R. *Chem. Commun.* **1994**, 801.

[56] Selvakannan, PR.; Mandal, S.; Pasricha, R.; Adyanthaya, S.D.; Sastry, M. *Chem. Commun.***2002**, 1334.

[57] Colvin, V. L.; Goldstein, A. N.; Alivisatos, A. P. *J. Am. Chem. Soc.***1992**, *114*, 5221.

[58] (a) Gole, A.; Sainkar, S. R.; Sastry, M. *Chem. Mater.***2000**, *12*, 1234. (b) Bandyopadhyay, K.; Patil, V.; Vijayamohanan, K.; Sastry, M. *Langmuir* **1997**, *13*, 5244. (c) Sastry, M. Colloids and Colloid Assemblies: Synthesis, Modification, Organization and Utilization of Colloid Particles ed. F. Caruso, Wiley-VCH, Berlin Chapter 12. **2003**, 369-397. (d) Sastry, M. Handbook of Surfaces and Interfaces of Materials, Ed. H.S. Nalwa, Nanostructured Materials, Micelles and Colloids, Academic Press, Volume 3, Chapter 2, 2001, 87-119.

[59] Ganguly, P.; Paranjape, D.V.; Sastry, M. *J.Am.Chem.Soc.* **1993**, *115*, 793.

[60] Leon, M.Clemente; Coronado, E.; Delhaes, P.; Gomez-Garcia, C.J.; Mignotaud, C. *Adv.Mater.*, **2001**, *13*, 574.

[61] Riccio, A.; Lanzi, M.; Antolini, F.; De Nitti, C.; Tavani, C.; Nicolini, C. *Langmuir* **1996**, *12*, 1545.

[62] Patino, J.M.R.; Nino, M.R.R.; Sanchez, C.C. *Ind.Eng.Chem.Res.***2002**, *41*, 2652.

[63] Ebara, Y.; Mizutani, K.; Okahata, Y. *Langmuir* **2000**, *16*, 2416.

[64] Sastry, M.; Ramakrishnan, V.; Pattarkine, M.; Gole, A.; Ganesh, K.N. *Langmuir* **2000**, *16*, 9142.

[65] Tabor, D. *J.Colloid Interface Sci.* **1980**, *75*, 240.

[66] Pockers, A. *Nature* **1891**, *43*, 437.

[67] Langmuir, I. *J.Am.Chem.Soc.* **1917**, *39*, 1848.

[68] Meldrum, F.C.; Kotov, N.A.; Fendler, J.H. *Langmuir*, **1994**, *10*, 2035.

[69] Tian, Y.; Fendler, J.H. *Chem.Mater*. **1996**, *8*, 969.

[70] Meldrum, F.C.; Kotov, N.A.; Fendler, J.H.; *J.Phys.Chem.***1994**, *98*, 4506.

[71] Kotov, N.A.; Zavala, G.; Fendler, J.H. *J.Phys.Chem.* **1995**, *99*, 12375.

[72] (a) Zhi-cheng, L.; Wei-dong, R.; Nan, J.; Lu-quad, R.; Qian, C.; Bing, Z. *Journal of Bionic Engineering* **2006,** *3*, 59. (b) Morawetz, K.; Reiche, J.; Kamusewitz, H.; Kosmella, H.; Ries, R.; Noack, M.; Brehmer, L. *Colloids and Surfaces A: Physicochem. Eng.Aspects* **2002,** 198–200, 409.

[73] Mass´e, P.; Ravaine, S. *Colloids and Surfaces A: Physicochem. Eng. Aspects* **2005,** 270–271, 148.

[74] (a) Swami, A.; Kumar, A.; Selvakannan, PR.; Mandal, S.; Pasricha, R.; Sastry, M. *Chem. Mater.***2003**, *15*, 17. (b) Selvakannan, PR.; Swami, A.; Srisathiyanarayanan,

D.; Shirude, P. S.; Pasricha, R.; Mandale, A. B.; Sastry, M. *Langmuir* **2004,** *20*, 7825.

[75] Köhler, J. M.; Fritzsche, Wolfgang "Nanotechnology: An Introduction to Nanostructuring Techniques" ed. Wiley-VCh

[76] Peng, X. G.; Manna, L.; Yang, W. D.; Wickham, J.; Scher, E.; Kadavanich, A.; Alivisatos, A. P. *Nature* **2000**, *404*, 59.

[77] Kan, S. H.; Mokari, T.; Rothenberg, E.; Banin, U. *Nat. Mater.* **2003**, *2*, 155.

[78] Pchelyakov, O.P.; Bolkhovityanov, Yu.B.; Dvurechenskii, A.V.; Nikiforov, A.I.; Yakimov, A.I.; VoigtlaÈnder, B. *Thin Solid Films* **2000,** *367,* 75.

[79] Castro, M.; Cuerno, R.; Va´zquez, L.; Gago, R. *Phys. Rev. Lett.* **2005**, *94*, 016102.

[80] Bai, J.B. *Materials Letters* **2003**, *57,* 2629.

[81] Hassenkam , T.; Nørgaard , K.; Iversen, L.; Kiely, C.J.; Brust, M.; Bjørnholm, T. *Adv. Mater.* **2002**, *14*, 1126.

[82] Stupp, S. I.; LeBonheur, V.; Walker, K.; Li, L. S.; Huggins, K. E.; Keser, M.; Amstutz, A. Science **1997**, *276*, 384.

[83] Wagner, R.S.; Ellis, W.C. *Appl. Phs.Lett.* **1964**, *89*, 4.

[84] Duang, X.F.; Lieber, C.M. *J. Am. Chem. Soc.* **2000**, *122*, 188.

[85] Masuda, H.; Satoh, M. *Jpn. J. Appl. Phys.* **1996**, *35*, L126

[86] Foss. C. A.; Hornyak, Jr. G. L.; Stockert, J. A.; Martin C. R. *J. Phys. Chem.* **1994**, *98*, 2963.

[87] Zheng, M.; Li, G.; Zhang, X.; Huang, S.; Lei, Y.; Zhang, L. *Chem. Mater.* **2001**, *13*, 3859.

[88] Zong, R.-L.; Zhou, J.; Li, Q.; Du, B.; Li, B.; Fu, M.; Qi, X.-W.; Li, L.-T.; Buddhudu, S. *J. Phys. Chem. B.***2004**, 108, 16713.

[89] Sapp, S.A.; Mitchell, D. T.; Martin, C.R. *Chem. Mater.* **1999**, *11*, 1183.

[90] Cao, H.; Xu, Y.; Hong, J.; Liu, H.; Yin, G.; Li, B.; Tie, C; Xu, Z. *Adv. Mater.* **2001**, *13*, 1393.

[91] Zhang, D.; Qi, L.; Ma, J.; Cheng, H. *Chem. Mater.***2001,** 13, 2753.

[92] Sedla´k, Milosˇ; Co¨lfen M. A. *Chem. Phys.* **2001**, *202*, 587.

[93] (a) Qi, L.; Co¨lfen, H.; Antonietti, M. *Angew. Chem., Int. Ed.* **2000**, *39*, 604. (b) Qi,

L.; Co¨lfen, H.; Antonietti, M. *Chem. Mater.* **2000**, *12*, 2392.

[94] Co¨lfen H. *Macromol. Rapid Commun.* **2001**, *22*, 219.

[95] Zhang, D.; Qi, L.; Ma, J.; Cheng, H. *Chem. Mater.* **2001**, *13*, 2753.

[96] Kabanov, A. V.; Kabanov, V. A. *Adv. Drug Deliv. Rev.* **1998**,*30,* 49.

[97] Co¨lfen, H.; Antonietti, M. *Langmuir* **1998**, *14*, 582.

[98] www.internationalpaper.com/PDF/PDFs_for_Papers/**History**%20of%20**Lithography**.pdf

[99] Stamou, D.; Musil, C.; Ulrich, W.-P.; Leufgen, K.; Padeste, C.; David, C.; Gobrecht, J.; Duschl, C.; Vogel, H. *Langmuir* **2004**, *20,* 3495.

[100] Noy, A.; Miller, A. E.; Klare, J. E.; Weeks, B. L.; Woods, B. W.; DeYoreo, J. J. *Nano Lett.* **2002,** *2*, 109.

[101] Ding, L.; Li, Y.; Chu, H.; Li, X.; Liu, J. *J. Phys. Chem. B.* **2005**, *109*, 22337.

[102] Li, J.; Lu, C.; Maynor, B.; Huang, S.; Liu, J. *Chem. Mater.***2004,** *16*, 1633.

[103] Keren, K.; Krueger, M.; Gilad, R.; Ben-Yoseph, G.; Sivan, U.; Braun, E. *Science (Washington, D.C.)* **2002**, *297*, 72.

[104] Braun, E.; Eichen, Y.; Sivan, U.; Ben-Yoseph, G. *Nature (London)* **1998**, *391*, 775.

[105] Ford, W.; Harnack, O.; Yasuda, A.; Wessels, J. *Adv. Mater*. **2001**, *13*, 1793-1797.

[106] Richter, J.; Seidel, R.; Kirsch, R.; Mertig, M.; Pompe, W.; Plaschke, J.; Schackert, H. K. *Ad*V. *Mater*. **2000**, *12*, 507.

[107] Monson, C. F.; Woolley, A. T. *Nano Lett.* **2003**; *3*, 359.

[108] Seeman, N.C. *Nature* **2003**, *421*, 427.

[109] Berti, Lorenzo ; Alessandrini, Andrea; Facci; Paolo *J. Am. Chem. Soc.* **2005**, 127, 11216.

[110] Griffin, F.; Ongaro, A.; Fitzmaurice, D. *Analyst* **2004** , *129* ,1171.

[111] (a) Dujardin, E.; Peet, C.; Stubbs, G.; Culver, J. N.; Mann, S. *Nano Lett.***2003,** *3*, 413. (b) Stubbs, G. *Semin. Virol.* **1990**, *1*, 405.

[112] Knez, M.; Bittner, A. M.; Boes, F.; Wege, C.; Jeske, H.; Maib, E.; Kern, K. *Nano Lett.* **2003,** *3*, 1079.

[113] Hybrid Organic-Inorganic Composites ed. by J.E. Mark, C. Y-C. Lee and P.A. Bianconi. Published As American Symposium Series, by American Chemical Society, Washington, DC **1995,** pg.1.

[114] Okada, A.; Usuki, A.; Kawasumi, M.; Kurauchi, T.; Kamigaito, O. *Polym. Prepr.* **1987**, *28*, 447.

[115] Buffet, Ph.; Borel, J-P. *Phys.Rev.* **1976**, *A13*, 2287.

[116] Narayanan, R.; El-Sayed, M. A. *J.Am.Chem.Soc.* **2004**, *126*, 7194.

[117] Liao, H.; Hafner, J. H. *J. Phys. Chem. B* **2004**, *108,* 19276.

[118] Tsuji, M.; Hashimoto, M.; Nishizawa, Y.; Tsuji, T. *Materials Letters* **2004**, *58*, 2326.

[119] Aslan, K.; Lakowicz, J. R.; Geddes, C.D. *J. Phys. Chem. B* **2005,** *109*, 6247.

[120] Wang, L.; Chen, X.; Zhan, J.; Chai, Y.; Yang, C.; Xu, L.; Zhuang, W.; Jing, B. *J. Phys. Chem. B* **2005**, *109*, 3189.

[121] Sun, Y.; Mayers, B.; Xia, Y. *Nano Lett* **2003**, *3*, 675.

[122] Hao, E.; Kelly, K. L.; Hupp, J.T.; Schatz, G.C.*J. Am. Chem. Soc.* **2002**, *124*, 15182.

[123] Maillard, M.; Giorgio, S.; Pileni, M.P. *Adv. Mater* **2002**, *14*, 1084.

[124] Chen, S.; Fan, Z.; Carroll, David L. *J. Phys. Chem. B* **2002**, *106,* 10777.

[125] Pastoriza-Santos, I.; Liz-Marza´n, L. M. *Nano Lett* **2002**, *2*, 903.

[126] Metraux, G.S.; Cao, Y.C.; Jin, R.; Mirkin, C.A. *Nano Lett.* **2003**, *3*, 519.

[127] Jin, R.; Cao, Y.; Mirkin, C.A.; Kelly, K. L.; Schatz, G.C.; Zheng, J.G. *Science* **2001**, *294*,1901.

[128] Jin, R.; Cao, Y.; Hao, E.; Metraux, G.S. *Nature* **2003**, *425*, 487.

[129] Shahbazyan, T. V.; Perakis, I. E.; Bigot, J.-Y. *Phys. Rev. Lett.* **1998**, *81*, 3120.

[130] Perner, M.; Bost, P.; Lemmer, U.; Plessen, G. von; Feldmann, J.; Becker, U.; Mennig, M.; Schmitt, M.; Schmidt, H. *Phys. Rev. Lett.* **1997**, *78*, 2192.

[131] Zhou, Y.; Wang, C. Y.; Zhu, Y. R.; Chen, Y. *Chem. Mater.* **1999,** *11,* 2310.

[132] Callegari, A.; Tonti, D.; Chergui, M. *Nano Lett.* **2003**, *3*, 1565.

[133] Maillard, M.; Huang, P.; Brus, L. *Nano Lett.* **2003**, *3*, 1611.

[134] Jiang, Li-Peng; Shu, X.; Zhu, J-M.; Zhang, J-R; Zhu, Ju-J; Chen, H-Y *Inorg. Chem.* **2004**, *43*, 5877.

[135] Tsuji, M.; Hasimoto, M.; Nishizawa, Y.; Tsuji, T. *Chem. Lett.* **2003**, *32*, 1114.

[136] (a) Martin, B. R.; Dermody, D. J.; Reiss, B. D.; Fang, M. M.; Lyon, L. A.; Natan, M. J.; Mallouk, T. E. *Adv. Mater.* **1999**, *11*, 1021. (b) Van Der Zande, B. M. I.; Bohmer, M. R.; Fokkink, L. G. J.; Schonenberger, C. *Langmuir* **2000**, *16*, 451.

[137] (a) Martin, C. R. *Chem. Mater*. **1996**, *8*, 1739. (b) Cepak, V. M.; Martin, C. R. *J. Phys. Chem. B*. **1998**, *102*, 9985. c) Schonenberger, C.; Vander Zande, B. M. I.; Fokkink, L. G. J.; Henny, M.; Schmid, C.; Kruger, M.; Bachtold, A.; Huber, R.; Birk, H.; Staufer, U. *J. Phys. Chem. B* **1997**, *101*, 5497.

[138] Coleman, K. S.; Hutchison, J. L.; Green, M. L. H. *Chem. Commun.***1999**, 699.

[139] (a) Pileni, M. P.; Gulik-Krzywicki, T.; Tanori, J.; Filankembo, A.; Dedieu, J. C. *Langmuir* **1998**, *14*, 7359. (b) Pileni, M. P.; Ninham, B. W.; Gulik-Krzywicki, T.; Tanori, J.; Lisiecki, I.; Filankembo, A. *Adv. Mater.* **1999**, *11*, 1358.

[140] Jana, Nikhil R.; Gearheart, L.; Murphy, C. J. *Adv. Mater.* **2001**, *13*, 1389.

[141] Roorda, S.; van Dillen, T.; Polman, A.; Graf, C.; van Blaaderen, A.; Kooi, B. J. *Adv. Mater.* **2004**, *16*, 235.

[142] http://depts.washington.edu/fhl/zoo432/argyle/Protection.htm

[143] McGrath, K. M. *Adv. Mater.* **2001**, *13*, 989.

[144] (a) Falini, G.; Albeck, S.; Weiner, S.; Addadi, L. *Science* **1996**, *271*, 67. (b) DeOliveira, D. B.; Laursen, R. A. J. *Am. Chem. Soc.* **1997**, *119*, 10627

[145] Raz, S., Testeniere, O.; Hecker, A.; Weiner, S.; Luquet, S. *Biol. Bull.* **2002**, *203*, 269.

[146] Cao, M.; Wang, Y.; Guo, C.; Qi, Y.; Hu, C. *Langmuir* **2004,** *20,* 4784.

[147] Shchukin, D. G.; Sukhorukov, G. B.; Mohwald, H. *Chem. Mater.* **2003,** *15,* 3947.

[148] (a) Fendler, J. H.; Meldrum, F. C. *Adv. Mater.* **1995**, *5,* 607. (b) Sastry, M. *Curr. Sci.* **2000**, *78*, 1089.c) Sastry, M.; Mayya, K. S.; Patil, V.; Hegde, S. G. *J. Phys. Chem. B* **1997**, *101*, 4954.

[149] (a) Freeman R. G.; et al. *Science* **1995**, *267*, 1629. (b) Shipway, A. N.; Katz, E.; Willner, I. *ChemPhysChem*. **2000**, *1*, 18.

[150] Kumar, A.; Mandal, S.; Mathew, S. P.; Selvakannan, P. R.; Mandale, A. B.; Chaudhari, R. V.; Sastry, M. *Langmuir* **2002**, *18*, 6478.

[151] Huheey, J. E. *Inorganic Chemistry*, **(Third Edition)**, 698.

[152] Berzelius, J. J. *Poggendoflfs Ann. Phys. Chem.* **1826,** *369*, 380.

[153] (a) Keggin, J. F. *Nature (London)*, **1933,** *131*, 908; (b) *Proc. R. SOC. London Ser. A* **1934**, *144*, 75.

[154] Osmond, F. *Bull. Soc. Chim. Fr.* **1887**, *47*, 745.

[155] (a) Himeno, S.; Kitazumi, I.; Sano, K-I *Analytical Sciences*, **1999**, *15*, 35.

[156] Okamoto, H.; T. Iwayanagi, K. Mochiji, H. Umezaki, T. Kudo *Appl. Phys. Lett.* **1986**, *49*, 298.

[157] Yamase, T. *J. Mater. Chem.* **2005**, *15*, 4773.

[158] Mu¨ller, A.; Peters, F. *Chem. Rev.* **1998,** *98,* 239.

[159] Staiti, P.; Arico, A.S.; Baglio, V.; Lufrano, F.; Passalacqua, E.; Antonucci, V. *Solid State Ionics* **2001,** 145, 101.

[160]. Bino, A.; Ardon, M.; Lee, D.; Spingler, B.; Lippard, S. J. *J. Am. Chem. Soc.***2002**, *124*, 4578.

[161] Glauert, A. M. *The Journal Of Cell Biology* **1974,** *63*, 717.

[162] Rautaray, D.; Sainkar, S. R.; Sastry, M. *Langmuir* **2003**, 19, 10095.

[163] Mandal, S.; Rautaray, D.; Sastry, M. *J. Mater. Chem.***2003**, *12*, 3002.

[164] Mandal, S.; Selvakannan, PR.; Pasricha, R.; Sastry, M. *J. Am. Chem. Soc.***2003,** *125*, 8440.

[165] Papaconstantinou, E. *Chem. Soc. Rev.***1989**, *18*,1.

[166] Mukherjee, P.; Senapati, S.; Mandal, D.; Ahmad, A.; Khan, M.I.; Kumar, R.; Sastry, M. C*hemBioChem* **2002**, *3*, 461.

[167] Ahmad, A.; Mukherjee, P.; Mandal, D.; Senapati, S.; Khan, M. I.; Kumar, R.; Sastry, M. *J. Am. Chem. Soc*. **2002,** *124*, 12108.

[168] (a) Rautaray, D.; Ahmad, A.; Sastry, M. *J. Am. Chem. Soc.***2003,** *125*, 14656. (b) Rautaray, D.; Sanyal, A.; Adyanthaya, S. D.; Ahmad, A.; Sastry, M. *Langmuir* **2004,** *20*, 6827.

[169] Song, J. K.; Li, N. K.; Kim, S. K. *Angew. Chem. Int. Ed*. **2003**, *42*, 213.

CHAPTER II

Characterization techniques

The different characterization techniques used in the course of the research work along with their guiding principles and their specifications are discussed in this chapter.

2.1 Introduction

Metal nanoparticles in the true sense are often present as colloidal solutions which are not perceptible to our normal naked eye. However special instrumental techniques have developed over the decades in order to characterize the nanoparticles. Property measurements and behavioural characterization have thus always been a challenging task to various researchers via different spectroscopic and microscopic techniques. This chapter thus bring about the basic principles of the various characterization techniques that have been used in the present thesis work. Synthesis of nanoparticles, nanosheets, anisotropic nanostructures through various chemical methods and mineral growth via compounds of biological origin have been the focus of the thesis which has been aptly characterized by UV-Vis spectroscopy, Fourier Transform Infrared Spectroscopy (FTIR), Scanning Electron Microscopy (SEM), Transmission Electron Microscopy (TEM), Atomic Force Microscopy (AFM), Isothermal Titration Calorimetry (ITC), X-Ray Photoelectron Spectroscopy (XPS), X-Ray Diffraction (XRD), Conductivity and Gel-electrophoresis measurements.

2.2 UV-Vis spectroscopy

2.2.1 Basic principles

Absorption spectroscopy in the visible region has long been an important tool to the analyst [1]. Appearance of colour arises from the property of the colored material to absorb selectively and reflect its complementary colour which falls within the visible region of the electromagnetic spectrum. Absorption of energy leads to a transition of electron from ground state to excited state which is governed by the following equation

$$\Delta E = h\nu = h\, c/\lambda$$

where h represents Planck's constant, ν is the frequency of radiation, c is the velocity of light and λ is the corresponding wavelength. Thus from the equation it seems that the UV-energy is quantized and hence a single discrete line should be obtained from a single electronic spectrum. However this is not obtained, as excitation of electronic energy

levels would also involve excitation of the embedded vibrational and rotational energy levels of an atom, thus giving rise to a broad absorption band [2]. The intensity of the absorption band depends on three factors namely a) transition probability, b) population of states and c) concentration or path length. Calculation of transition probability requires an exact knowledge of the wave-functions of the initial and the final states and is generally governed by *selection rules*. Through the deduction of selection rules (eg. *Laporte's selection rule*) it is possible to predict whether a transition will be allowed or forbidden. Population of states is also an important factor when intensity is concerned, as absorption from the most populated state will give rise to the most intense spectrum. If we consider *N* no. of molecules to be divided into the excited (final state) and ground states (initial state) named as f and i respectively, then statistically following Boltzmann distribution it can be shown that

$$\frac{N_f}{N_i} = \exp\left(-\Delta E / kT\right)$$

Where $\Delta E = E_{final} - E_{initial}$

T is the Temperature in Kelvin and k is Botzmann's constant

Almost all relationships between intensities of incident and transmitted radiation and the concentration and path-length is governed by Beer-Lambert's law which is written as

$$I = I_0 \exp\left(-\kappa c l\right)$$

Where I= Intensity of the emitted radiation,

I_0= Intensity of the incident radiation,

κ= constant

c= concentration and

l= path length

The equation can be recast into $\log (I_0/ I) = A = \kappa c l$,

Where the ratio log (I_0/ I)=A is known as the Absorbance or the optical density and κ, the constant generally represented as ε, known as the molar absorption coefficient.

Absorbance at a particular wavelength is thus due to an electronic transition which can occur via the following means:

a) Transition between the bonding and antibonding levels of n, π or σ electrons.

b) Charge-transfer transitions which include ligand-metal, ligand-ligand and metal-metal intervalent transitions.

c) d-d transitions which are generally weak in intensity and are forbidden with respect to centrosymetric rule.

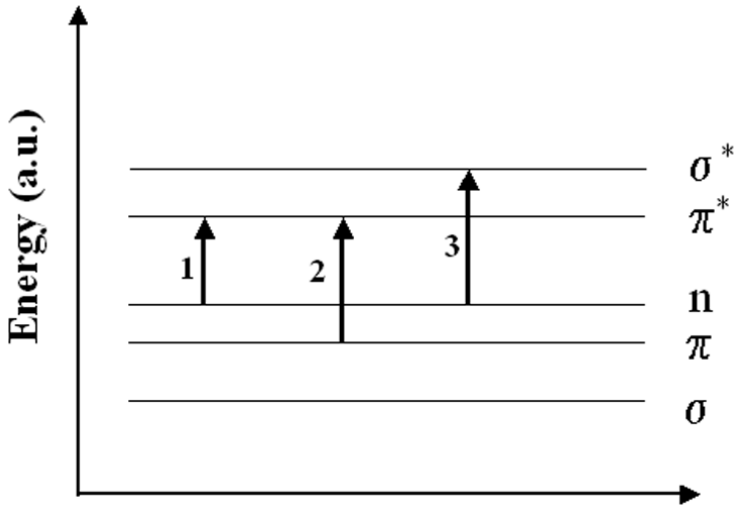

Figure 2.1: *Schematic of the energy levels of the various possible electronic transitions.*

Out of the possible electronic transitions, n-π^* and π-π^* transition is the most intense and obtained in case of compounds having either lone pair of electrons or an unsaturated carbon atom (double bonds or conjugated systems) as is shown in the schematic of Figure 2.1. The energy required for these transitions is relatively low as compared to the other σ-σ^* and n-σ^*, hence their absorption is red-shifted and falls well within the visible range of the electromagnetic spectrum.

As was discussed in the previous chapter, when the size of a metal becomes less than the electronic mean free path, then the surface free electrons vibrate coherently with the frequency of the incident radiation giving rise to a phenomenon known as " Surface Plasmon Resonance". Gustav Mie, a German physicist, along with Danish physicist Lorenz provided a complete analytical solution to the Maxwell's equations for scattering of electromagnetic waves by small spherical particles which is today better known as Mie theory [3]. He showed that the extinction coefficient (C_{ext}) behaves as

$$C_{ext} = \frac{24\pi^2 R^3 \varepsilon_m^{3/2}}{\lambda} \frac{\varepsilon''}{(\varepsilon'+2\varepsilon_m)^2 + \varepsilon''^2}$$

Where R is the radius of the particle in cm, ε' and ε'' are the real and imaginary parts of the dielectric constant of the particle and ε_m is the dielectric constant of the medium. Thereby after a series of calculations we obtain the relationship between the plasma frequency and the no. of electrons as

$$\omega_p^2 = Ne^2/ m \varepsilon_0$$

where, N is the concentration of free electrons in the metal, m, the effective mass of the electron and ε_0 is the dielectric constant.

In today's spectrophotometer both deuterium and tungsten lamp is used as the source for characterization in the UV and visible regions respectively. However one xenon arc lamp can also be used which can serve the purpose for both UV and visible region. In such a dual beam spectrophotometer, light from either the visible or the ultraviolet source enters the grating monochromator before it reaches the filter. Broadband filters contained in a filter wheel are automatically indexed into position at the required wavelengths to reduce the amount of stray light and unwanted orders from the diffraction grating. The light from the source is alternatively split into one of two beams by a rotating mirror called a chopper as is shown in the schematic of Figure 2.2, one beam is passed through the sample and the other through the reference. Some double-beam instruments have two detectors, and the sample and reference beam are measured at

the same time. In other instruments, the two beams pass through a beam chopper which blocks one beam at a time.

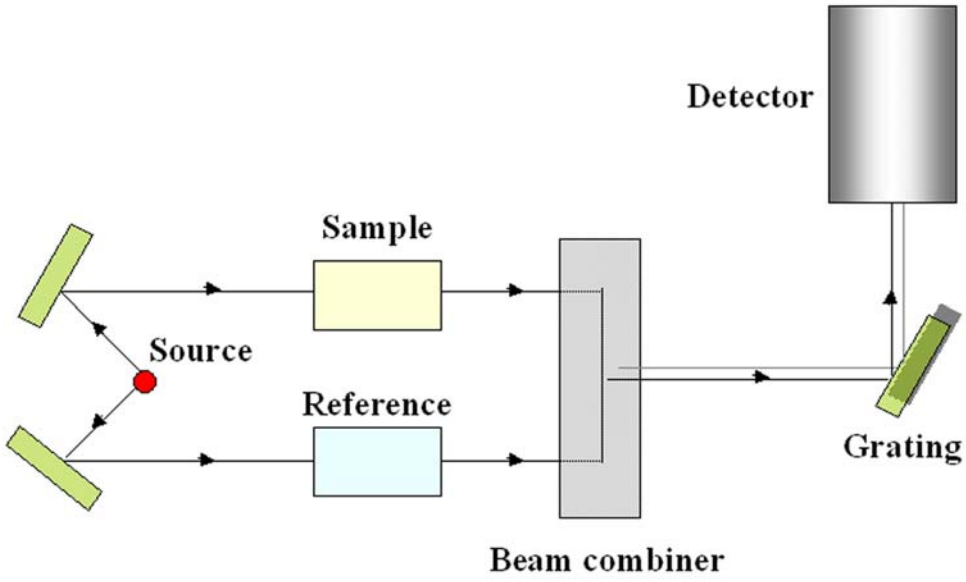

Figure 2.2: *A pictorial representation of the principle of UV-Vis spectrophotometer.*

The detector, which is often a photodiode, alternates between measuring the sample beam and the reference beam. UV-Vis spectroscopy has been widely used during the characterization of the formation of metal nanoparticles and all the experiments have been performed on a Jasco V-570 UV/Vis/NIR spectrophotometer operated with a resolution of 2 nm. UV-Vis spectroscopy of the nanosheets were carried on a Hewlett-Packard HP 8542A diode array spectrophotometer operated at a resolution of 2 nm.

2.3 Fourier Transform Infrared (FTIR) spectroscopy

2.3.1 Instrumentation

Modern spectrometers working in the infrared region generally use the Fourier transform technique for spectral detection and analysis. The essential part of an FTIR instrument is the Michelson's interferometer, which consists of static and a movable mirror as shown in Figure 2.3. The source is generally a Nernst filament consisting of a spindle of rare-earth oxides. The beam is then guided and made to pass through a beam

splitter (a part of the interferometer, a component which reflects about half of the radiation that hits it and transmits the rest). The beam thus divided into 2 parts recombine again either constructively or destructively depending on the path difference created by the movable mirror. An actual signal thus consists of radiation spanning a large number of wavenumbers and the total intensity is thus an integration from the individual contributions.

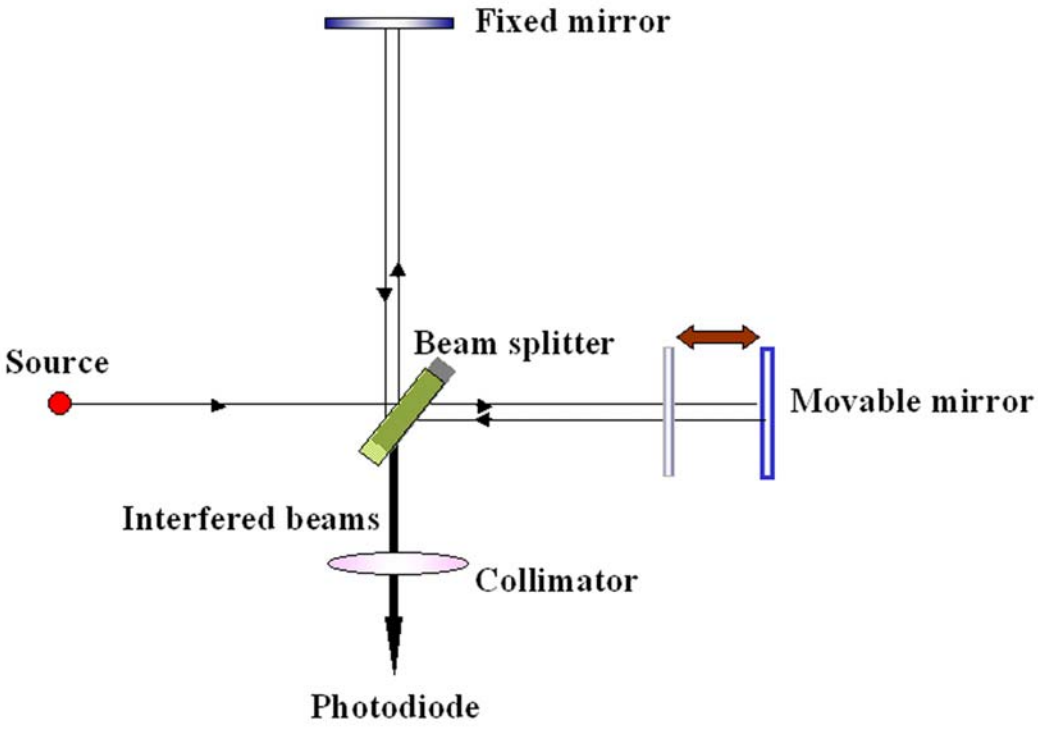

Figure 2.3: *Schematic showing the basic principle behind Michelson's interferometer.*

Due to changes in the relative position of the moving mirror to the fixed mirror, an interference pattern is generated. The resulting beam then passes through the sample and is eventually focused on the detector. When this IR beam is directed through the sample, the amplitudes of a set of waves are reduced by absorption if the frequency of this set of waves is the same as one of the characteristic frequencies of the sample. The interferogram contains information over the entire IR region to which the detector is responsive. A mathematical operation known as Fourier transformation converts the interferogram (a time domain spectrum displaying intensity versus time within the mirror scan) to the final IR spectrum, which is the familiar frequency domain spectrum showing

intensity versus frequency. The detector commonly used in the FTIR instruments is the pyroelectric substance, deuterated triglycine sulfate (DTGS). Other photoconductive detectors include indium antimonide (InSb) or mercury cadmium telluride (MCT), which are highly sensitive and have faster response time.

2.3.2 Basic principle

Infrared spectroscopy deals with the energy changes corresponding to vibrational transitions in a molecule. If we take an example of a molecule consisting of two atoms, then when they come together to form a bond, they experience an attractive force between the nucleus and the electron cloud; at the same time they impart a repulsion due to the like charges present in both the nuclei as well as the electron cloud. Thus there is a compromise where the system stabilises at distance when both the atoms are at equilibrium distance (r_{eq}). Any distortion to the bond length implies a change in the internuclear distance, thus this compression and extension of the bond can be thought to be analogous to that of a spring obeying Hooke's law. Thus we may write

$$F= -k (r- r_{eq})$$

Where F is the restoring force, k the force constant and r, the internuclear distance. Classically this is an example of a simple harmonic model whose oscillation frequency, ω

$$\omega_{osc}= \frac{1}{2\pi}\sqrt{\frac{k}{\mu}}\ cm^{-1}$$

Where μ= reduced mass and k the force constant.

At temperatures above absolute zero, all the atoms in molecules are in continuous vibration with respect to each other. When the frequency of a specific vibration is equal to the frequency of the IR radiation directed on the molecule, the molecule absorbs the radiation. Each atom has three degrees of freedom, corresponding to motions along any of the three Cartesian coordinate axes (x, y, z). A polyatomic molecule of n atoms has 3n total degrees of freedom. Additionally, 3 degrees of freedom correspond to rotation of the entire molecule. Therefore, the remaining (3n – 6) degrees of freedom are true, fundamental vibrations for nonlinear molecules. Linear molecules possess (3n – 5)

fundamental vibrational modes because only 2 degrees of freedom are sufficient to describe rotation. Among the (3n – 6) or (3n – 5) fundamental vibrations (also known as normal modes of vibration), those that produce a net change in the dipole moment may result in an IR activity. Thus any linear molecule having 3 atoms should theoretically possess 4 normal modes of vibration (symmetric stretching and bending and asymmetric stretching and binding). Hence it is possible to identify the presence of functional groups in a molecule. For example the two bands at 2920 and 2850 cm^{-1} are assigned to the antisymmetric and symmetric methylene (CH_2) stretching vibrations respectively and two weak bands at about 2960 and 2875 cm^{-1} to the asymmetric/degenerate and symmetric methyl (CH_3) stretching vibrations respectively [4]. Another typical example of the N-H stretching vibrations band, which appear for the free amine at 3333 cm^{-1}. This band shifts to 3198 cm^{-1} on salt formation of primary amine [5]. Similarly –C=O (carbonyl) frequency at ~1720 cm^{-1} is shifted to either side depending on the electronegativity of the attached atom or groups of atom. FTIR is thus an indispensable tool in the detection of the presence of capping agents, their interaction with the formed nanoparticles and so on. Almost all samples for FTIR measurements have been drop-coated onto Si (111) wafers and air-dried, however some samples have been taken in the form of powder and mixed with the standard KBr powder. The FTIR measurements of these samples were carried out on a Perkin Elmer Spectrum One FTIR spectrometer operated in the diffuse reflectance mode at a resolution of 4 cm^{-1}. A total of 256 scan yielded a good signal to noise ratio of the IR spectra.

2.4 Scanning electron microscopy (SEM)

The scanning electron microscope (SEM) is a type of electron microscope that is capable of inspecting topographies of sample surface and offer three-dimensional high resolution images of the sample surface.

2.4.1 Instrumentation

A schematic of the working of a SEM is shown in Figure 2.4. It consists of an electron gun, the lenses to guide the beam into the sample chamber and the detector.

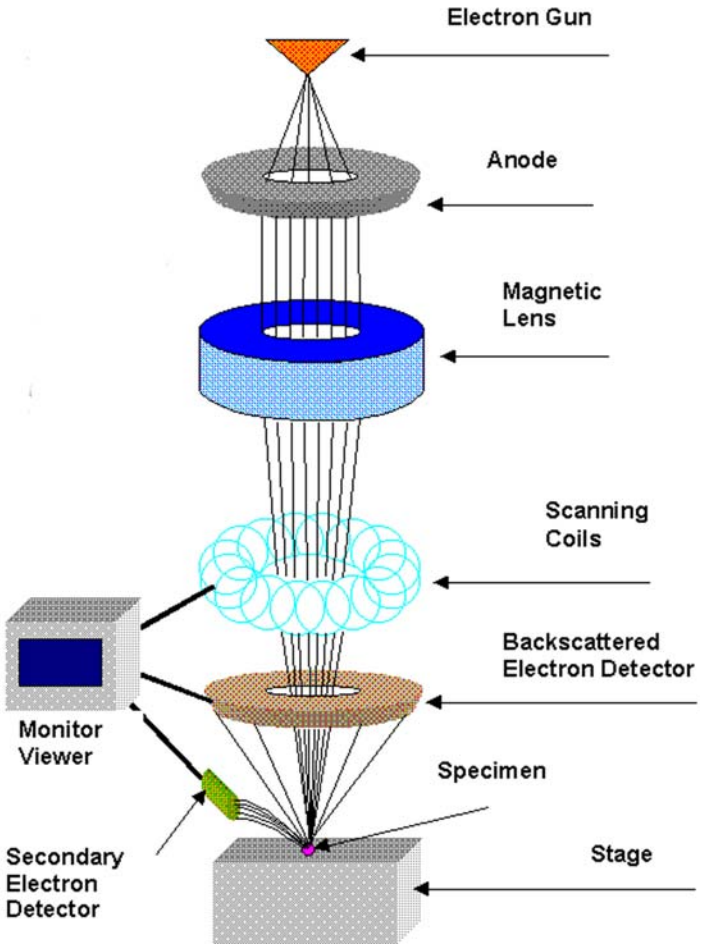

Figure 2.4: *Schematic showing the working of a Scanning Electron Microscope. (Ref: http://www.rpi.edu/dept/materials/COURSES/NANO/shaw/Page5.html)*

a) The electron beam comes from a heated filament, usually tungsten hairpin gun is used which functions as the cathode. A high voltage applied to the loop heats up the filament. Other filaments like LaB_6 and field emission guns are also used.

b) The stream is condensed by the first condenser lens. This lens is used to both form the beam and limit the amount of current in the beam. It works in conjunction with the condenser aperture to eliminate the high-angle electrons from the beam.

c) This beam is attracted through the anode, condensed by the condenser lens, and focused as a very fine point on the sample by the objective lens. The scan coils are

energized (by varying the voltage produced by the scan generator) and create a magnetic field which deflects the beam back and forth in a controlled pattern. These set of coils then "scan" or "sweep" the beam in a grid fashion (like a television), dwelling on points for a period of time determined by the scan speed (usually in the microsecond range).

d) When the beam strikes the sample (and dwells for a few microseconds), various type of interactions occur between the sample and the electron beam and are detected with various instruments.

e) The electron beam thus after hitting the sample, produces secondary electrons from the sample. These electrons are collected by a secondary detector or a backscatter detector, converted to a voltage, and amplified. The amplified voltage is applied to the grid of the CRT and causes the intensity of the spot of light to change. The image consists of thousands of spots of varying intensity on the face of a CRT that correspond to the topography of the sample. Most SEMs are equipped with Evarhart-Thornley (E-T) detector.

One important point to note that while running the SEM, the column must be in vacuum due to various reasons which is generally provided by a roughing pump or a diffusion pump or in some special cases an ion pump.

2.4.2 Basic principle

2.4.2.1 ***Specimen-Beam interaction*****:** There are various processes in which a sample interacts with the incident electron beam. A cartoon of the various processes is shown in Figure 2.5. Backscattered electrons produced by an incident electron colliding with an atom in the specimen, which is nearly normal to the incident's path. The incident electron is then scattered "backward" 180 degrees. The production of backscattered electrons varies directly with the specimen's atomic number or “specimen interaction volume”. Specific interaction volume is the volume inside the specimen in which interactions occur while being struck with an electron beam.

This volume depends on the following factors:

(a) Atomic number of the material: higher atomic number materials absorb or stop more electrons and so have a smaller interaction volume.

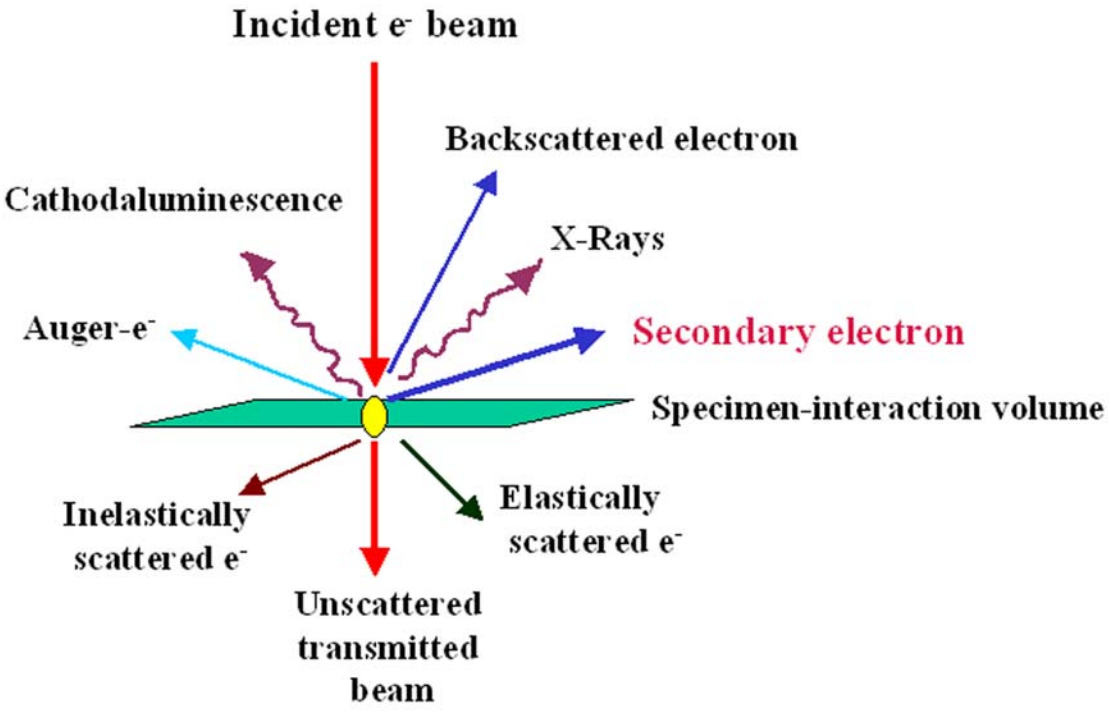

Figure 2.5: *A cartoon showing the possible effects after sample-electron beam interaction.*

(b) Accelerating voltage being used; higher voltages penetrate farther into the sample and generate larger interaction volumes.

(c) Angle of incidence for the electron beam; the greater the angle (further from normal) the smaller the volume.

This differing production rates causes higher atomic number elements to appear brighter than lower atomic number elements. Secondary electrons are produced when the low-lying electrons are knocked from the sample surface by the electrons. These electrons which are knocked out have very less kinetic energy (~ 5eV) are known as " secondary electrons", hence only those electrons which are knocked from the surface of the sample are able to reach the detector. These electrons are collected by a secondary detector or a backscatter detector, converted to a voltage, and amplified.

2.4.2.2 *Energy Dispersive Analysis of X-rays (EDAX)*

Energy Dispersive analysis of X-rays (EDAX) is a chemical microanalysis technique. It is also sometimes referred to as EDX or EDS analysis. It is a technique to identify the elemental composition of the specimen or for an area of interest. It works as an integrated feature with the SEM and cannot function on its own. During EDAX analysis the specimen is bombarded with the incident electron beam. When a voltage of 10-20 keV is used in the SEM, the incident electrons knock out the inner core level electrons of the sample. The electrons from the higher energy levels fill up the vacancy thus created. During this transition X-ray is emitted which is plotted as no. of counts (intensity) with respect to the binding energy. The detector generally used in EDAX analysis is different from SEM and is the Lithium drifted Silicon detector, known as SiLi detector. This detector must be operated at liquid nitrogen temperatures. The photoelectron emitted is drawn into the Si detector, which creates electron-hole pairs. These electron-hole pairs are attracted towards the opposite ends of the detector by a strong electric field. The SiLi detector is often protected by Beryllium window, hence it protects detection of soft X-rays of elements having low atomic number.

An EDAX spectrum also shows the nature of X-rays emitted which means that a transition from the L-level to the K-level is known as the K-alpha peak, transition from M-level to K-level is known as the K-β peak and so on. This is shown in the cartoon of Figure 2.6. In this thesis we have extensively used SEM for observing the morphology of hybrid-composites and the minerals synthesized via various methods. SEM measurements were performed on a Leica Stereoscan-440 scanning electron microscope instrument equipped with a Phoenix EDAX attachment. Samples for SEM and EDAX analysis from the solutions at different stages experiments discussed in this thesis were prepared by solution-casting films onto Si (111) wafers.

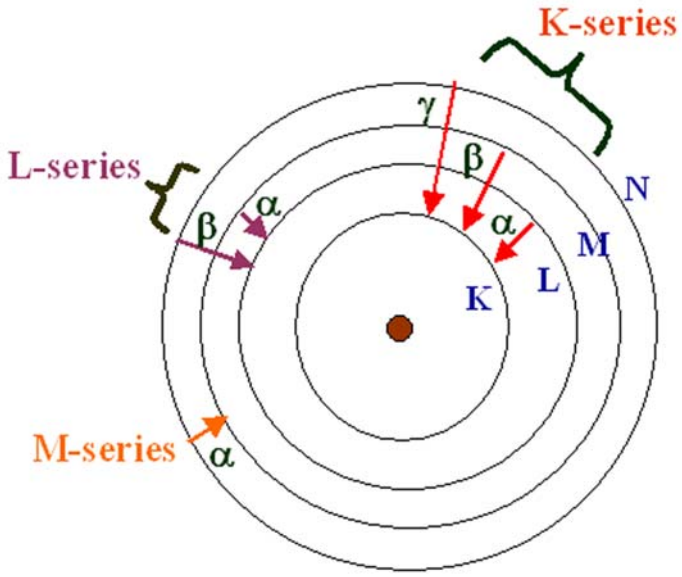

Figure 2.6: *Schematic showing the possible transition lines as obtained from an EDAX spectrum.*

2.5 Transmission electron microscopy (TEM)

2.5.1 Instrumentation and principle

The transmission electron microscope (TEM) operates on the same basic principles as the light microscope but uses electrons instead of light. In TEM analysis, a thin specimen is illuminated with electrons in which the electron intensity is uniform over the illuminated area. As the electrons travel through the specimen, they are either scattered by a variety of processes or they may remain unaffected by the specimen. The end result is that a nonuniform distribution of electrons emerges from the exit surface of the specimen that contains all the structural and chemical information about the specimen. Electron microscope is constructed to display this nonuniform distribution of electrons in two different ways. A "light source", typically a tungsten or LaB_6 filament at the top of the microscope emits the electrons that travel through vacuum in the column of the microscope as shown in Figure 2.7. Instead of glass lenses focusing the light in the light microscope, the TEM uses electromagnetic lenses to focus the electrons into a very thin beam. The electron beam then travels through the specimen. Depending on the density of the material present, some of the electrons are scattered and disappear from the beam. At the bottom of the microscope the unscattered electrons hit a fluorescent screen,

which gives rise to a "shadow image" of the specimen with its different parts displayed in varied darkness according to their density. The image can be studied directly by the operator or photographed with a camera.

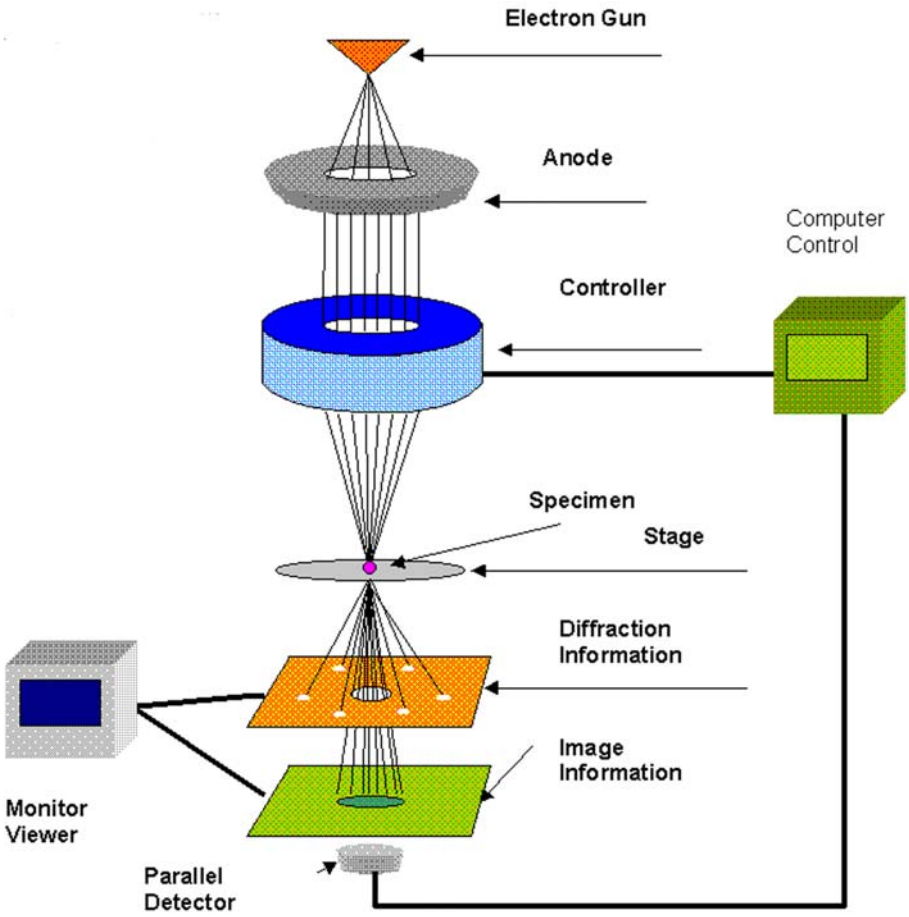

Figure 2.7: *A pictorial representation of the Transmission Electron Microscope. (Ref: http://www.rpi.edu/dept/materials/COURSES/NANO/shaw/Page5.html)*

When we form images in TEM, we either form an image using the central spot, or we use some or all of the scattered electrons. In the case of **bright-field imaging** an aperture is inserted into the back focal plane of the objective lens, thus blocking out most of the diffraction pattern except that which is visible through the aperture whereas in **dark-field imaging** one or more of the diffracted beams is allowed to pass through and the direct beam is blocked by the aperture. Some useful information like planar defects, stacking faults can be obtained through dark-field imaging. Bright field imaging depends

on the mass-thickness of the sample. Areas of the sample that are thicker will have fewer transmitted (unscattered) electrons, hence will appear darker. In selected area electron diffraction (SAED), an aperture is used to define the area from which a diffraction pattern is formed in a TEM specimen. The resulting patterns contain information about the lattice spacing measurement and sample orientation.

In this thesis TEM measurements have been performed to study the formation of nanosheets and other anisotropic nanostructures. The TEM measurements were done on a JEOL model 1200EX instrument operated at an accelerating voltage of 120 kV. Samples for TEM analysis were prepared by drop-coating the sample onto carbon-coated copper grids and allowing the solvent to evaporate.

2.6 Atomic Force Microscopy (AFM)

2.6.1 Instrumentation and basic principle

The atomic force microscope (AFM), or scanning force microscope (SFM) was invented in 1986 by Binnig, Quate and Gerber [6]. An AFM consists of a sharp tip mounted at the end of a tiny cantilever spring which is moved by a mechanical scanner on the surface to be imaged. An atomically sharp tip is scanned over a surface with feedback mechanisms that enable the piezo-electric scanners to maintain the tip at a constant force (to obtain height information), or height (to obtain force information) above the sample surface. Tips are typically made from Si_3N_4 or Si, and extended down from the end of a cantilever as is shown in the schematic of Figure 2.8. Since the cantilever obeys Hook's law for small displacements, hence the interaction between the tip and the sample can be found out. The movement of the tip or sample is performed by an extremely precise positioning device made from piezo-electric ceramics, most often in the form of a tube scanner. The scanner is capable of sub-angstrom resolution in x-, y- and z-directions. The z-axis is conventionally perpendicular to the sample. However the interaction force between the tip and the sample is very small, of the order of 10^{-9} N. Nowadays the nanoscope AFM system employs an optical based detection system whereby a laser detector is placed at the behind of the reflective cantilever. Any difference in the intensity of light observed at the laser photodetector is the result of the

scanning of the tip on the contours of the sample surface. The photodetector then converts the change in light intensity into voltage.

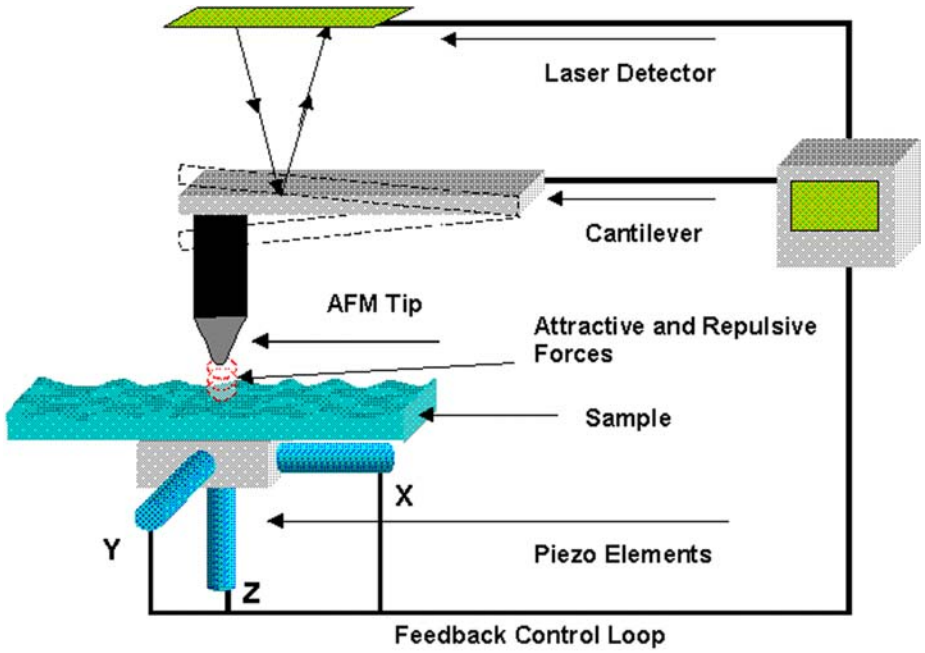

Figure 2.8: *Schematic showing the working of an Atomic Force Microscope. (Ref: http://www.rpi.edu/dept/materials/COURSES/NANO/shaw/Page5.html)*

There are 3 modes of imaging; the contact mode, tapping mode and the non-contact mode. **Contact mode** is the most common method of operation of the AFM. As the name suggests, the tip and sample remain in close contact as the scanning proceeds. By "contact" we mean in the repulsive regime of the inter-molecular force curve. The deflection of the cantilever when it scans the sample surface is compared to some desired value in the DC feedback amplifier. If there is a difference in the value, the feedback amplifier sends a voltage to the piezo to take the sample to the desired value. Thus the application of voltage is a measure of the height of the features present on the sample. Adsorbed gases consisting primarily of water vapour form a layer over the sample surface at ambient conditions, hence when the probe comes in contact with the contaminant layer, the cantilever is pulled to the sample surface due to surface tension. This can distort sample surfaces or damage the tip. In the **tapping mode** the cantilever is made to vibrate in its resonant frequency Thus the tip oscillates with a high amplitude

and 'taps' or touches the sample only at intermittent time intervals. The detector thus measures the oscillation amplitude of the tip. In the **non-contact mode** the tip remain 50 - 150 Angstrom above the sample surface. Attractive Van der Waals forces acting between the tip and the sample are detected, and topographic images are constructed by scanning the tip above the surface.

Samples of the gold nanotriangles synthesised chemically and shown in one of the later chapters formed were cast onto Si (111) substrate and analyzed by Atomic force microscope (AFM) in the contact mode on a VEECO Digital Instruments multimode scanning probe microscope equipped with a Nanoscope IV Controller.

2.7 X-ray diffraction (XRD)

2.7.1 Basic principle

X-rays, which are electromagnetic radiation with wavelengths of the order of 10^{-10} m, are typically generated by bombarding a metal target with high-energy electrons. The electrons decelarate as they undergo elastic and inelastic collisions and generate radiation with a continuous range of wavelengths known as Bremsstrahlung. After the discovery of X-ray by Roentgen, Laue in 1912 suggested that the X-rays can be diffracted when passed through a crystal. Thus a technique came into existence which had immense potential for detection of samples.

Diffraction of x-rays occurs in a crystal, as the distance between the planes of the crystal is comparable to the wavelength of x-rays. When x-rays strike a crystal, it interacts with the arrays of atoms (electrons) and undergoes elastic and inelastic scattering. It is the elastically scattered beam that we are interested as that contains the information about the arrangement of the atoms in the crystal lattice. The diffracted coming from a set of planes either combine constructively or destructively depending on the phase difference. They follow a relation as was given by Bragg and is commonly known as Bragg's law where,

$$2d \sin\theta = n \lambda$$

where θ= angle of incidence

d= interplanar distance

λ= wavelength of X-rays (1.54A^0 for Cu K_α)

and n= order of reflection (integer values of 1, 2, 3…).

This suggests that only for integral value of n, the equation satisfies the appearance of bright spots on the screen that is constructive interference occurs. Bragg's diffraction pattern is schematically shown in Figure 2.9.

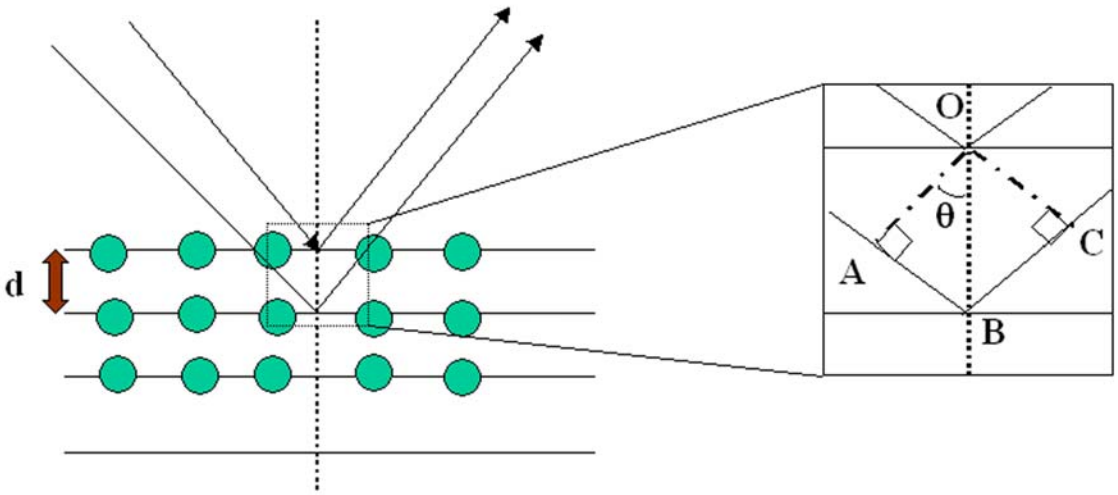

Path difference= AB+BC
AB=BC=d cos (90-θ)= d sin θ

Hence AB+BC=2d sin θ= n λ

Figure 2.9: *Pictorial representation of Bragg's law.*

An alternative method to Laue's technique is the powder diffractometer in which monochromatic x-rays are focused on pellet or slide mounted on rotating stage. Since sample is powder, all possible diffractions are recorded simultaneously from hypothetical randomly oriented grains. Mount is then rotated to ensure all diffractions are obtained. Powder diffraction technique is used to identify a sample of a solid substance by comparison of the position of the diffraction line and the corresponding intensity with a large data bank. The intensity of the diffraction line depends on the scattering strengths of the individual atoms which in turn depends on the electron density. The phase difference between the *hkl* reflections of 2 atoms, one of which is located at the origin and the other located at the coordinates (*xa*, yb, zc) is given by,

$$\phi_{hkl} = 2\pi (hx+ky+lz)$$

The total intensity is thus the integration of the scattering strengths of all the atoms taken together. Hence the **structure factor** of a unit cell containing n atoms with scattering factors f_n is given by;

$$F_{hkl} = \Sigma f_j \exp \{ i (\phi_{hkl})$$

Thus the intensity is proportional to F_{hkl}^2.

For practical reasons the diffractometer measures an angle twice that of the theta angle. All the XRD data presented here in the thesis were carried out on a Philips PW 1830 instrument operating at a voltage of 40 kV and a current of 30 mA with Cu Kα radiation. Most of the XRD samples were made by drop coating the sample on a glass plate, however in some cases, like those prepared through biological methods, the samples were centrifuged and dried to obtain powder.

2.8 X-ray photoelectron spectroscopy (XPS)

X-ray photoelectron spectroscopy (XPS), also known as Electron Spectroscopy for Chemical Analysis (ESCA), is a widely used technique for obtaining chemical information of various material surfaces. XPS was developed in the mid 1960s by Professor K. Siegbahn and his research group [7]. The incident photon knocks out the electron from the core level, it is one of the best surface sensitive techniques as the electrons emitted from underneath layers undergo inelastic collision and hence cannot reach the detector. The released electron retains all the energy from the striking photon. It can then escape from the atom provided it has the energy greater than the work-function of the metal.

2.8.1 Basic principle and instrumentation

XPS is based on the well-known photoelectric effect first explained by Einstein in 1905. The ejected photoelectron has kinetic energy as given by

$$KE = hv - BE - \Phi$$

where, hν = energy of photons , BE= Electron Binding Energy ,
KE= Electron Kinetic Energy, Φ = Work Function.

The XPS instrument measures the kinetic energy of all collected electrons. The electron signal includes contributions from both the photoelectron and Auger electron lines. It might happen that an electron from the higher energy state fills up the vacancy created by the knocking photon. This transition leads to the release of X-rays which again knock out one more electron from the upper state. This emerging electron is called the " Auger" electron. Photoelectron line energies are thus dependent on photon energy whereas Auger electron line energies are not dependent on photon energy. For each and every element, there will be a characteristic binding energy associated with each core atomic orbital i.e. each element will give rise to a characteristic set of peaks in the photoelectron spectrum at kinetic energies determined by the photon energy and the respective binding energies. The basic requirements for a XPS instrument as shown in Figure 2.10 are:

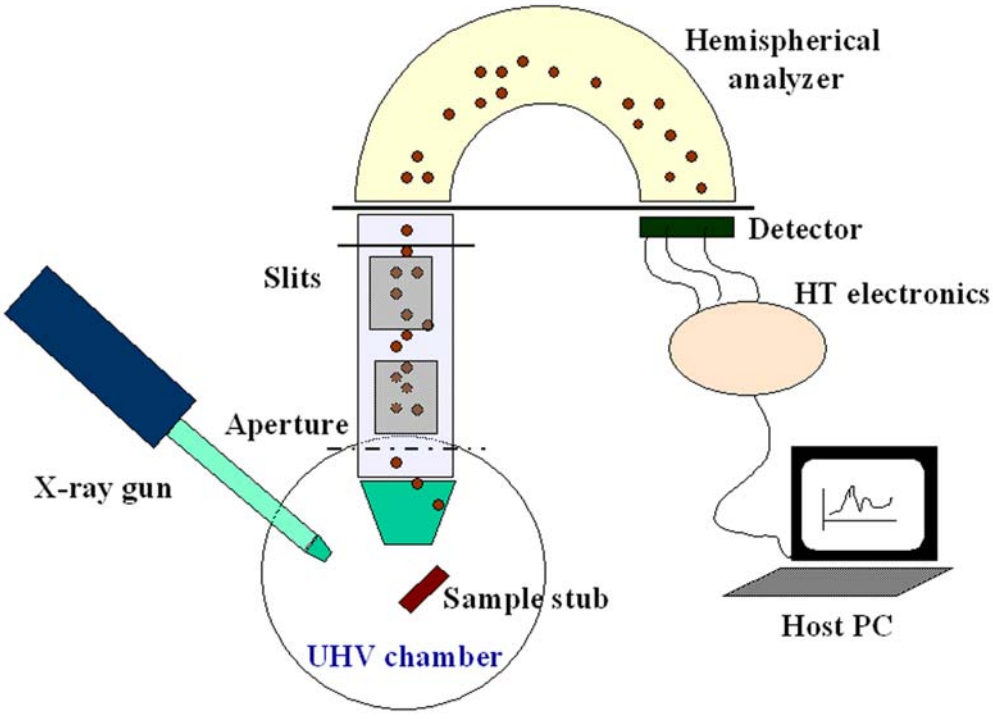

Figure 2.10: *Schematic showing the working of an X-ray Photoelectron spectrometer.*

(1) X-ray source of fixed-energy radiation (usually Mg Kα with hν = 1253.6 eV or Al Kα with hν = 1486.6 eV)

(2) Concentric hemispherical analyser (CHA), which uses an electric field between two hemispherical surfaces to allow electrons of a particular kinetic energy (so called the Pass energy), and thereby measure the flux of emitted electrons of a particular energy.

(3) A high vacuum environment (to enable the emitted photoelectrons to be analysed without interference from gas phase collisions)

A closer look at the spectra from the core levels of *p, d and f levels* (example Au 4f or Ag 3d) shows the presence of a photoemission doublet. The reason for the formation of the doublet is the mixing of the spin and the angular momentum, commonly known as the spin-orbit coupling, it can be the Russell- Saunders (*l-s*) coupling or the *j-j* coupling. As for example since the value of *l* for d orbital is 2 hence the coupling will result in the *j value of* 5/2 (2+1/2) and 3/2 (2-1/2). Thus there will be 2 states of $d_{5/2}$ and $d_{3/2}$, the intensity of which depends on the multiplicity.

$$\text{Multiplicity} = 2j+1$$

Hence, for $d_{5/2}$, multiplicity = 2*(5/2)+1=6 and

for $d_{3/2}$, multiplicity = 2*(3/2)+1=4

Thus the ratio of the intensities of the peak will be 6:4 or 3:2 or 1.5:1.

XPS measurements of drop coated films on Si (111) substrates from different nanoparticle solutions were carried out on a VG MicroTech ESCA 3000 instrument at a pressure of better than $1x10^{-9}$ Torr. The general scan and the C1s, W 4f, Pt 4f Au 4f and Ca 2p core level spectra from different samples were recorded with un-monochromatized Mg Kα radiation (photon energy = 1253.6 eV) at pass energy of 50 eV and electron takes off angle (angle between electron emission direction and surface plane) of 60^0. The overall resolution was ~1 eV for the XPS measurements. The core level spectra were background corrected using the Shirley algorithm [8] and the chemically distinct species resolved using a non-linear least squares fitting procedure. The core level binding energies (BE) were aligned with the adventitious carbon binding energy of 285 eV.

2.9 Isothermal Titration Calorimetry (ITC)

Every molecular interaction is followed by either a release or absorption of energy and ITC is an ultra-sensitive technique to detect any minute changes in the heat of interaction. Each ITC experiment provides a complete thermodynamic profile of the interaction including the binding constant (Ka), the number of binding sites (*n*), enthalpy (ΔH), entropy (ΔS), and free energy (ΔG). The basic essence of ITC lies in the extremely sensitive measurement of the time derivative of heat change during ligand binding to a substrate, bond cleavage and formation, solvation dynamics, conformational and configurational changes and molecular reorganizations which is otherwise transparent to the observer. ITC has been used with success in the study of protein-protein interactions [9], protein-DNA association [10], DNA-DNA [11] and peptide-antibody [12] interactions. Many reports have also appeared in the literature on ITC investigation of association of polyelectrolytes in aqueous solution [13], micellization and related percolation phenomenon [14], direct determination of pK_a of thiols [15] etc. A photograph of the VP-ITC instrument is shown in Figure 2.11. The VP-ITC system is an ultrasensitive isothermal titration calorimeter that uses a cell feedback network (CFB) to differentially measure and compensate for heat produced or absorbed between the sample and reference cell.

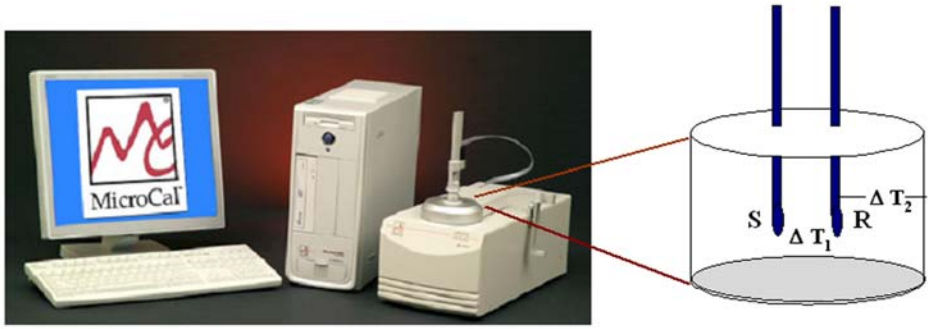

R= Reference Cell

S= Sample Cell

Figure 2.11: *A photograph showing the ITC instrument. The figure on the right hand side shows the presence of a sample and a reference cell. (Ref: http://www.microcal.com/index.php?id=14)*

A thermoelectric device measures the temperature difference between the two cells (ΔT_1 as shown in the schematic of Figure 2.11) and a second device measures the temperature difference between the cells and the jacket (ΔT_2). During operation, a very small constant power is supplied to a heater on the reference cell. The amount of power supplied to the sample cell (feedback power) is continuously adjusted so that its temperature is always identical to that of the reference cell. If, for example, an exothermic reaction occurs in the sample cell, then the feedback power to the sample cell will automatically be reduced to null the temperature difference caused by the heat released in the sample cell. The precise amount of heat released by the exothermic process can then be determined since it is exactly equal to the reduction in the amount of feedback heat necessary to reestablish the temperature null between the cells [16].

Isothermal titration calorimetric (ITC) measurements were carried out to characterize the interaction between Keggin ions and the various amino acids in a Micro Cal VP-ITC instrument operated at 298 K. As described above the calorimeter consisted of two cells: a reference cell filled with pure solvent (water) and a sample titration cell filled with 1.47 ml of 10^{-3} M of the required sample. Exothermicity or endothermicity is obtained as a result of injection of the ligand contained in the syringe into the sample cell. The raw data obtained is integrated to obtain a curve referred to as the " binding isotherm", which allows extraction of the various thermodynamic parameters.

2.10 Gel electrophoresis

Electrophoresis is the migration of charged molecules in solution in response to an electric field. Their rate of migration depends on the strength of the field; on the nett charge, size and shape of the molecules and also on the ionic strength, viscosity and temperature of the medium in which the molecules are moving. As an analytical tool, electrophoresis is simple, rapid and highly sensitive. **SDS-PAGE** (**s**odium **d**odecyl **s**ulfate **p**oly**a**crylamide **g**el **e**lectrophoresis) is a technique used in biochemistry and molecular biology to separate proteins according to their size (length of polypeptide chain or molecular weight). The equipment required for electrophoresis consists basically of two items, a power pack and an electrophoresis unit. The solution of proteins to be analyzed is first mixed with SDS, an anionic detergent which denatures secondary and

non–disulfide–linked tertiary structures, and applies a negative charge to each protein in proportion to its mass. Without SDS, different proteins with similar molecular weights would migrate differently due to differences in folding, as differences in folding patterns would cause some proteins to better fit through the gel matrix than others. The denatured proteins are subsequently applied to one end of a layer of posubmerged in a suitable buffer. An electric current is applied across the gel, causing the negatively-charged proteins to migrate across the gel. Depending on their size, each protein will move differently through the gel matrix: short proteins will more easily fit through the pores in the gel, while larger ones will have more difficulty. After a set amount of time (usually a few hours), the proteins will have differentially migrated based on their size; smaller proteins will have traveled farther down the gel, while larger ones will have remained closer to the point of origin. Thus proteins may be separated roughly according to size (and therefore, molecular weight). Following electrophoresis, the gel may be stained (most commonly with Coomassie Brilliant Blue or silver stain), allowing visualisation of the separated proteins, or processed further (e.g. Western blot). After staining, different proteins will appear as distinct bands within the gel. It is common to run "marker proteins" of known molecular weight in a separate lane in the gel, in order to calibrate the gel and determine the weight of unknown proteins by comparing the distance traveled relative to the marker. The R_f is calculated as the ratio of the distance migrated by the molecule to that migrated by a marker dye-front.

In this thesis, we have used a vertical gel system. Vertical slab gel units are commercially available and routinely used to separate proteins in acrylamide gels. The gel is formed between to glass plates that are clamped together but held apart by plastic spacers. Gel dimensions are typically 12 cm x 14 cm, with a thickness of 0.5 to 1 mm. A plastic comb is placed in the gel solution and is removed after polymerization to provide loading wells for samples. When the apparatus is assembled, the lower electrophoresis tank buffer surrounds the gel plates and affords some cooling of the gel plates. The electrophoresis is carried out in an appropriate buffer, which is essential to maintain a constant state of ionization of the molecules being separated [17]. The protein fraction responsible for the control of mineral morphology was analyzed by 10 % SDS-PAGE carried out at pH 8.2 according to the procedure published by Laemmli [18].

2.11 Conductivity measurement

Conductivity is the ability of a material to conduct electric current. The principle by which instruments measure conductivity is: two plates are placed in the sample, a potential is applied across the plates (normally a sine wave voltage), and the current is measured. It is the inverse of resistance, if the current applied is I and the voltage is V, the conductance C= I/ V. Since the charge on ions in solution facilities the conductance of electrical current, the conductivity of a solution is proportional to its ion concentration. Most conductivity meters have a two-electrode cell available in either dip or flow-through styles. The electrode surface is usually platinum, titanium, gold-plated nickel, or graphite. The electrical resistivity, ρ of any material is given by;

$$\rho = R \times \frac{L}{A}$$

where R= resistance,

L= length of the specimen (column of liquid between the electrode in case of aqueous solution0

and A= Cross-sectional area

Hence, $1/\rho = \text{Conductivity} = (1/R) \times \frac{A}{L}$

Conductivity is generally expressed in siemens and the ratio (L/A) is known as the cell constant. Conductivity meters and cells should be calibrated to a standard solution before using. The conductivity of Absolute pure water is around 0.055 μS/cm at 298K. The conductance of a mixture consisting of equal volumes of 10^{-3} M phosphotungstic acid and 10^{-3} M lysine solutions during the formation of lysine-PTA complex was monitored using a Pico-conductivity meter (Lab India).

2.12 References

[1] Denney, R.C; Sinclair, R. *Visible and Ultraviolet Spectroscopy*. *Analytical Chemistry by open learning series*, John Wiley and Sons, USA.

[2] Banwell, C. N.; McCash, E. M. *Fundamentals of Molecular Spectroscopy* Fourth

edition ed. Tata Mc-Graw-Hill Publishing Company limited.

[3] Mie, G.; *Ann. Phys*., **1908**, *25*, 377.

[4] Ralph G. Nuzzo, Florence A. Fusco, David L. Allara *J. Am. Chem. Soc.***1987**, *109*, 2358.

[5] Bardosova, M.; Tregold, R.H.; Ali-Adib, Z. *Langmuir* **1995**, 11, 1273.

[6] Binnig, G; Quate, CF; Gerber, C *Physical Review Letters* **1986**, *56*, 930.

[7] Siegbahn, K. *et al.; Nova Acta Regiae Soc. Sci. Upsal.. Ser. IV* **1967***, 20*, 1.

[8] Shirley, D. A. Phys. Rev. B **1972**, 5, 4709.

[9] Pierce, M. M.; Raman, C. S.; Nall, Barry T. *METHODS* **1999**,*19*, 213.

[10] Milev,S.; Gorfe, A. A.; Karshikoff, A.; Clubb, R. T.; Bosshard, H. R.; Jelesarov, I. *Biochemistry* **2003**, *42,* 3481.

[11] Goobes, R.; Kahana, N.; Cohen, O.; Minsky, A. *Biochemistry* **2003**, *42,* 2431.

[12] Wenk, M. R.; Seelig, J. *Biochemistry* **1998**, *37,* 3909.

[13] Bangar R., B.; Winnik, F. M.; Morishima, Y. *Langmuir* **2001,** *17,* 4416.

[14] Hait, S. K.; Moulik, S. P.; Palepu, R. *Langmuir* **2002,** *18,* 2471.

[15] Tajc, S. G.; Tolbert, B. S.; Basavappa, R.; Miller, B. L. *J.Am.Chem.Soc.* **2004**,*126*, 10508.

[16] Chellani, M. *Application Notes* **1999**, 14.

[17] Wilson, K.; Walker, J. "*Practical Biochemistry*" (5th Edition) Cambridge University Press.

[18] Laemmli, U. K. *Nature* **1970**, *227*, 680.

CHAPTER III

Synthesis of gold and platinum nanosheets at the liquid-liquid interface

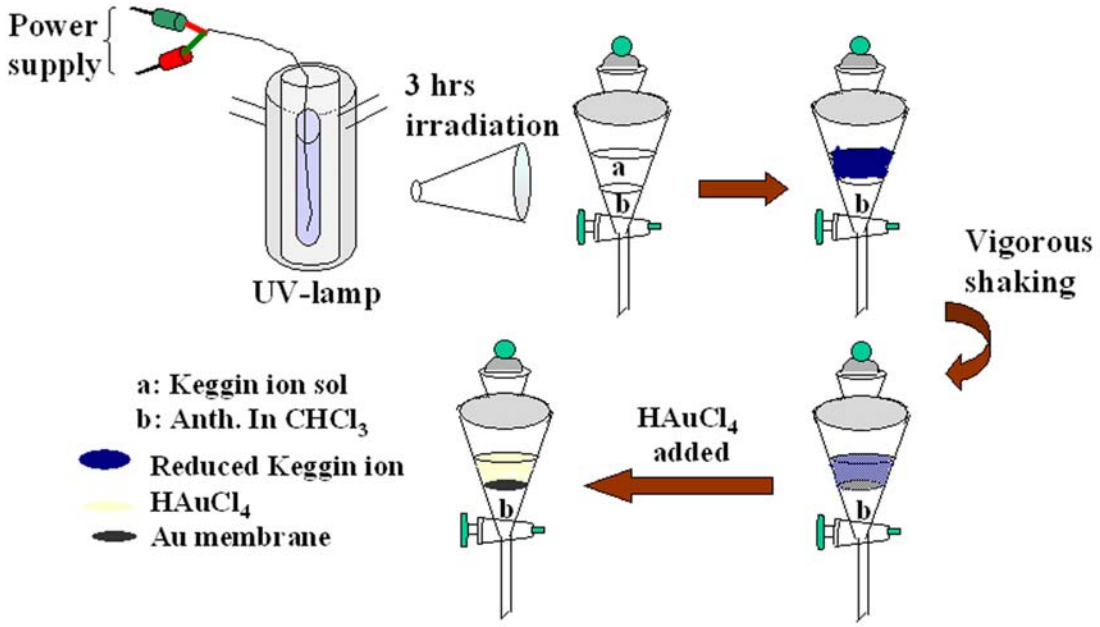

This chapter discusses the synthesis of flat nanosheets of gold and platinum at the liquid-liquid interface using aqueous photochemically charged Keggin ions. Here, we have accomplished facile electron transfer to anthracene molecules present in an organic phase by exposure to photochemically reduced Keggin ions. Addition of this organic phase to an equimolar solution of chloroauric acid resulted in the formation of flat sheets of gold at the interface. The reaction applies similarly to platinum also. In a very similar approach, 2D nanosheets were obtained at the liquid-liquid interface containing Keggin ions and $HAuCl_4$ in the aqueous medium and octadecylamine (ODA) in an organic medium.

Part of the work presented in this chapter has been published:

1) Sanyal, A.; Sastry, M. *Chem. Commun.* **2003**, 1236.

3.1 Introduction

Significant research in nanotechnology has been devoted to developing simple and reliable protocols for the synthesis of nanomaterials having various sizes and morphologies. During the middle of 19th century nanostructured metallic colloids were mainly been synthesized by the "top-down" approach, which included mechanical breakdown of bulk structures into smaller and smaller parts. Methods such as lithography, ball-milling technique etc. were in vogue, which enabled semiconductor based industries in developing newer and smaller circuits. However, methods following this technique slowly lost prominence due to the inherent drawbacks that prevented from going below a certain size regime. The other approach, the "bottom-up" method then subsequently gained a lot of acceptance and is still very much in use among contemporary researchers. This approach includes wet-chemical methods like coprecipitation [1], sol-gel synthesis [2], template-mediated synthesis [3] and so on. Synthesis of gold hydrosols (gold nanoparticles dispersed in water) dates back to the middle of 19th century when Michael Faraday [4] synthesized the gold sol and is still enjoying importance as a fascinating topic of research. Such chemical based protocols include reduction of metallic salts into zerovalent metals by use of suitable reducing agents and thereafter capping with stabilizers like donor ligands, polymer-coat or surfactants to prevent them from agglomeration. Turkevich for the first time synthesized gold nanoparticles by chemical reduction of $AuCl_4^-$ ions with sodium citrate, which has become a standard protocol for the synthesis of nanoparticles [5-7].

Apart from the prominent plasmon-resonance properties of gold nanoparticles, the latter finds excellent application in catalysis [8], DNA detection [9], cellular imaging [10] and biochemical sensors [11]. This immense spectrum of usage is mainly due to the easy to synthesize, excellent biocompatibility and noncytotoxic nature of gold nanoparticles [12]. Thus, researchers have been stimulated with the synthesis of gold nanoparticles with desired shape and size selectivity. Other than synthesis of gold hydrosols there have been reports of synthesis of gold nanoparticles in organic solvents [13, 14] wherein aqueous chloroaurate ions, after being phase transferred into non-polar organic solvents by use of tetraalkylammonium ions, are reduced and capped by alkanethiol or alkylamine moieties [13]. This protocol commonly known as 'Brust protocol', was later on tailored by a single

step method, whereby using a novel molecule called hexadecylaniline in which all the three different steps were condensed into a single step [14a]. In the recent past, there has been growing interest in developing new methodologies for the synthesis of gold nanoparticles of varying shapes such as nanorods [15-17], nanowires [18,19] and nanoprisms [20-22]. Such synthesis has been motivated due to the presence of multiple plasmon resonance property especially in the near infrared region, which makes these nanostructures excellent candidates for biomedical applications and in self-cleaning windows [23].

An interesting possibility for introducing shape anisotropy in gold nanoparticles is to synthesize them in constrained environments such as those provided by Langmuir-Blodgett films [24] or at well-defined two-dimensional interfaces. Sastry *et.al* have investigated the latter approach recently and have shown that gold nanosheets and nanoribbons can be grown at the air-water interface by the spontaneous reduction of choloroaurate ions present in the subphase by 4-hexadecylaniline Langmuir monolayers [25]. This chapter entails the synthesis of gold and platinum nanosheets by photochemically excited Keggin ions and anthracene anions bound at a liquid-liquid interface. Keggin ions form a subset of polyoxometalates and have the general formula $(XM_{12}O_{40})^{(8-n)-}$, where 'M' stands for W or Mo and 'X' stands for heteroatoms such as P, Si, Ge with *n* being the valency of X [26]. Anthracene is the smallest unsubstituted aromatic hydrocarbon with a positive electron affinity (0.53 eV) [27] and can exist in a stable valence anion state [26]. We have accomplished electron transfer to anthracene molecules present in chloroform by exposure to photochemically reduced aqueous phosphotungstate [PTA, Keggin ions, $(PW_{12}O_{40})^{3-}$] ions. We have also synthesized similar type of nanostructures by restraining the reduction to be preferential at the interface between ODA in toluene and a mixture of chloroauric acid and Keggin ions.

3.2 Synthesis of gold nanosheets at a liquid-liquid interface

In a typical experiment, to 15 ml of deaerated 10^{-3} M aqueous solution of phosphotungstic acid ($H_3PW_{12}O_{40}$, from Aldrich Chemicals and used as-received) 1 ml of propan-2-ol was added and this solution was irradiated by UV light (pyrex filter, > 280 nm, 450 W Hanovia medium pressure lamp) for 4 h as shown in the scheme of Figure

3.1. After irradiation, the solution colour turned to dark blue which is characteristic of the excited state of the polyoxometallates. To the UV-irradiated PTA solution, 15 ml of 10^{-3} M anthracene in chloroform was added and the solution vigorously stirred (steps 2 and 3). It was observed that after vigorous stirring the dark blue colour of the excited Keggin ions gradually faded, suggesting oxidation of the Keggin ions. Following steps 2 and 3, the chloroform layer was carefully separated from the biphasic mixture and to this, 15 ml of 10^{-3} M aqueous solution of $HAuCl_4$ was added (step 4, Figure 3.1). After vigorous stirring of this biphasic solution for 15 minutes, a bluish-black film was observed to form at the water-chloroform interface (step 5, Figure 3.1). The aqueous layer was carefully removed and the film present on the surface of chloroform was carefully lifted onto carbon-coated transmission electron microscopy (TEM) grids and Si (111) wafers for further analysis.

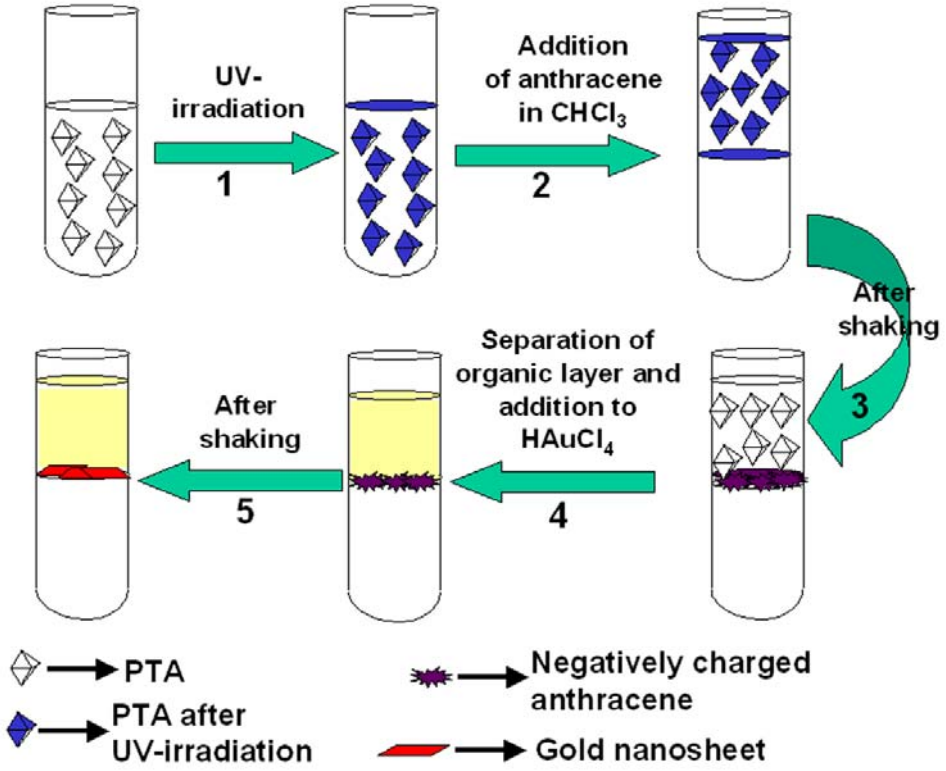

Figure 3.1: *Scheme showing the various steps that leads to the formation of the gold nanosheet at the liquid-liquid interface between anthracene in chloroform and aqueous chloroauric acid.*

3.2.1 UV-Vis spectroscopy measurements

UV-Vis spectra were recorded at different stages of the reaction. Curve 1 in Figure 3.2 shows the UV-Vis spectrum of the solution containing aqueous PTA solution before irradiation. The solution was colourless as was evidenced from the absence of any peak in the visible region of the electromagnetic spectrum. This is due to the charge-transfer transition that occurs between the donor oxygen ion and the tungsten metal which has a vacant d- orbital and is in +6 (d^0) oxidation state [28]. This class of polyoxometallates can be photochemically reduced (step 1 in ' scheme', Figure 3.1), hence the PTA solution was irradiated for appx. 4 hours and the UV-Vis spectrum was recorded after irradiation, which is shown as curve 2 in Figure 3.2.

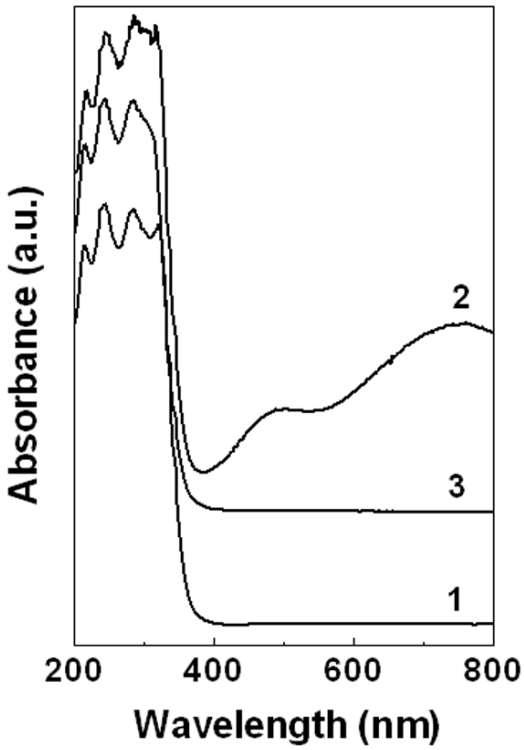

Figure 3.2: *UV-vis spectra recorded from 1: 10^{-3} M aqueous PTA solution before UV irradiation; 2: 10^{-3} M aqueous solution of PTA after UV-irradiation; 3: UV-irradiated aqueous PTA solution after stirring with 10^{-3} M anthracene in chloroform.*

The spectrum showed an intense absorption around 500 and 760 nm which was the signature of the dark blue coloured solution. The peak is due to the intervalent metal

transition between one tungsten atom (d^1 state) and another tungsten atom (d^0 state) and the *d-d* transition [28]. The colour of the reduced state is stable only for a few hours, which suggests easy aerial oxidation of the reduced state to the original ground state. Curve 3 in Figure 3.2 shows the UV-Vis spectrum of the aqueous reduced PTA solution after reaction with anthracene in $CHCl_3$. The graph looks almost similar to the graph of PTA solution before irradiation (Curve 1 in Figure 3.2), which suggests that probably the extra charge on the PTA molecule has been transferred to the anthracene moiety thereby converting it into the stable anion form. This was possible owing to the positive electron affinity and a stable anion form of the anthracene molecule.

3.2.2 Transmission Electron Microscopy (TEM) studies

Figure 3.3 shows representative TEM pictures recorded from different regions of the Au-anthracene film formed at the liquid-liquid interface.

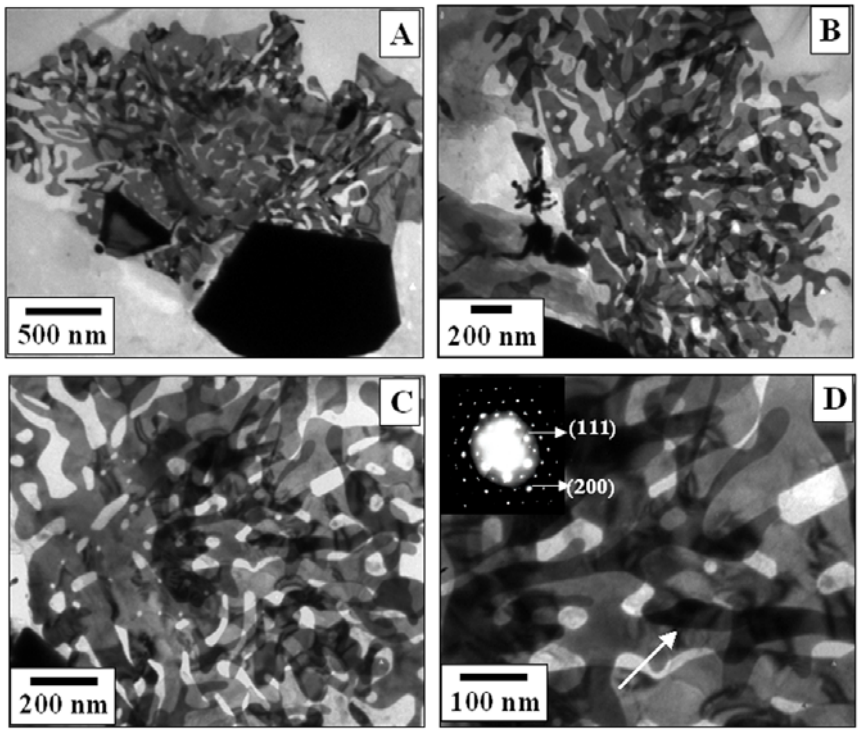

Figure 3.3A-D: *Representative TEM images at different magnifications recorded from the gold nanoparticles/nanosheets grown at the liquid-liquid interface .The inset in Figure 3.3D shows the Selected Area Electron Diffraction (SAED) pattern recorded from the gold nanosheet indicated by an arrow.*

In addition to a very small number of quasi-spherical particles, the TEM images (Figure 3.3A and B) clearly show that the film surface is covered with a large concentration of thin sheets of gold. The morphology of the individual gold nanoparticles range from spherical to ellipsoidal to triangular while their size was measured to be in the regime of 10 to 80 nm. The characteristic feature of the TEM pictures is the presence of sheets of gold, one of which is indicated by an arrow in Figure 3.3D. The presence of clear strain features and fractal-like formation is probably due to the buckling of the sheets (Figure 3.3C). This also suggests that the sheets are extremely thin and are overlapping with each other. The large anisotropy in the morphology of the gold nanostructures is clearly a consequence of the localized reduction of the gold ions by anthracene anions occurring at the liquid-liquid interface (step 5, Figure 3.1). The selected area electron diffraction (SAED) pattern recorded from the gold nanosheet identified by the arrow in Figure 3.3D is shown in the inset of Figure 3.3D and has been indexed with reference to the structure of fcc gold.

3.2.3 XRD and AFM measurements

Figure 3.4A shows the X-ray diffraction pattern recorded from the anthracene anion layer after reaction with aqueous $AuCl_4^-$ ions (step 5, Figure 3.1). A number of sharp Bragg reflections can be seen which can be indexed based on the fcc structure of gold (PCPDF File No. 040784, *a=b=c=4.078*). It is clear that the blue-black film formed at the interface between chloroform and water consists of particles of crystalline gold. This can only occur by reduction of the aqueous $AuCl_4^-$ ions by anthracene anions thus clearly establishing that electron transfer had occurred from UV-irradiated Keggin ions and anthracene (steps 2 and 3, Figure 3.1). Keggin ions are known to exhibit strong and characteristic Bragg reflections in the 2θ regions scanned in Figure 3.4B [29]. However, it was observed that such strong and characteristic Bragg reflection peaks were not obtained in case of the blue-black film. This suggests that there are hardly any interfacially bound Keggin ions, which might have acted as the reducing agent for the formation of gold nanosheets.

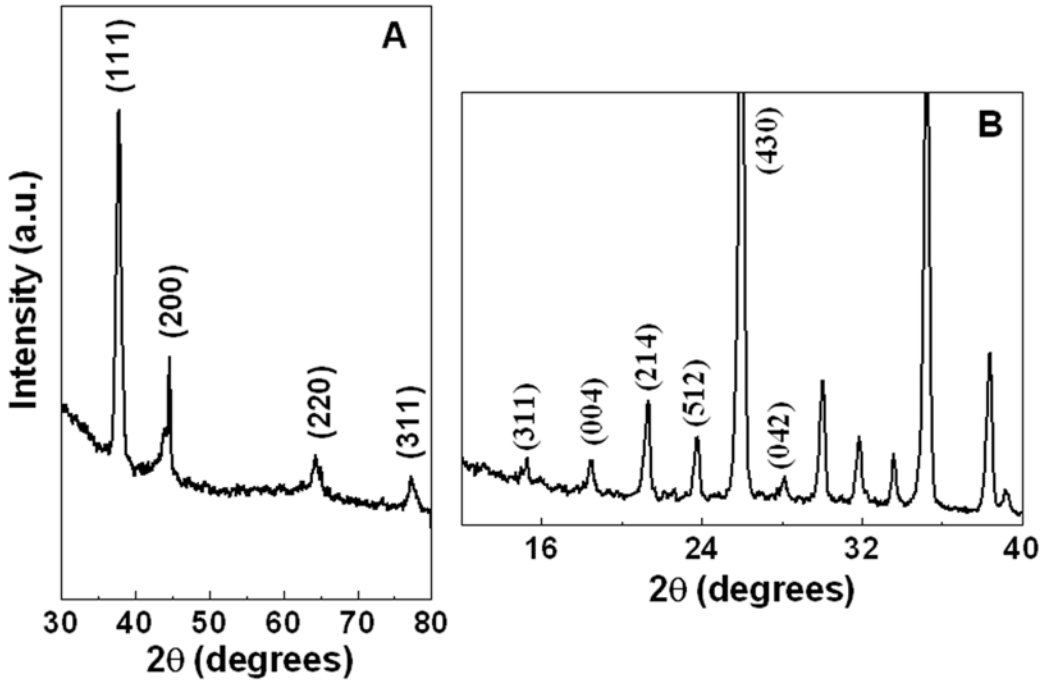

Figure 3.4: *A) XRD pattern recorded from gold nanoparticles/nanosheets grown at the liquid-liquid interface using anthracene anions. B) XRD pattern of pure Keggin ion. The Bragg reflections have been marked and belong to the unit lattice of PTA of lattice parameters a= 20.91, b= 13.13 and c=19.00 (PCPDF File no. 38-0178)*

An estimate of the thickness of the nanosheets was done by AFM of films deposited on Si (111) wafers (Figure 3.5). The thickness of the sheets ranged from 30-300 nm and a relatively thick sheet of ca. 280 nm is shown in Figure 3.5A. The large anisotropy in the morphology of the gold nanostructures is clearly a consequence of the localised reduction of the gold ions by anthracene anions occurring at the liquid-liquid interface (step 5, Figure 3.1).

The thickness of the gold nanostructure would be limited by the fact that the reducing surface is truly two-dimensional as argued for similar structures obtained by Sastry and co-workers during the spontaneous reduction of gold ions near hexadecylaniline Langmuir monolayers [25]. The surface of the sheet is not uniform as is evident from the x-z profile shown in Figure 3.5B which confirms that the thickness varies from as small as 30 nm to as thick as 300 nm.

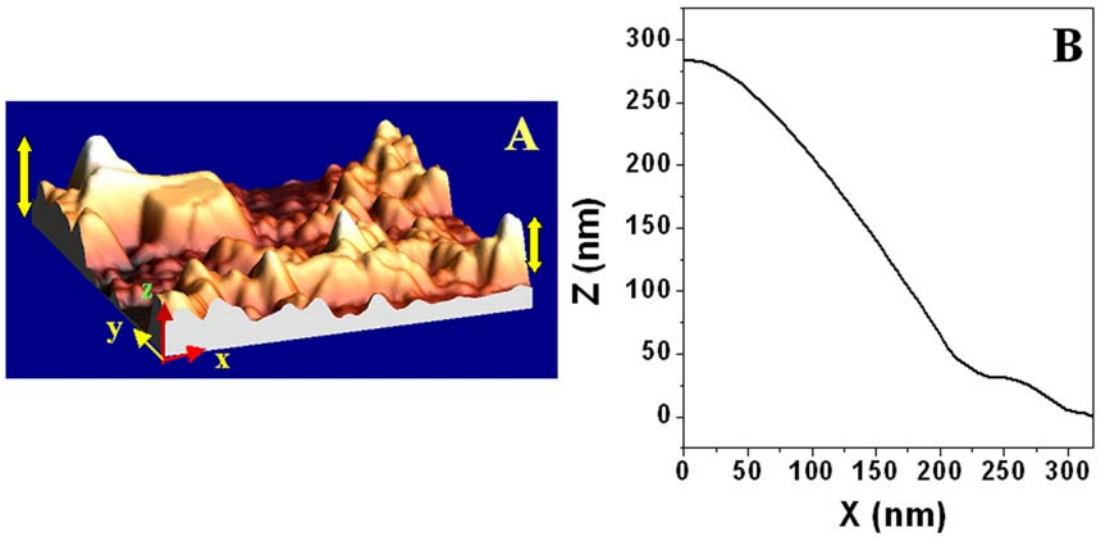

Figure 3.5: *A) Contact mode AFM image of the gold nanosheet grown at the liquid-liquid interface. B) Height profile showing the non-uniformity of the formed gold nanosheet.*

3.2.4 X-Ray Photoelectron Spectroscopy (XPS) & SEM measurements

To understand the nature of the gold nanosheet formed, a chemical analysis of the sheet lifted onto Si (111) wafers was carried out using XPS technique. Figure 3.6 represents the C 1s and Au 4f core level spectra recorded from the gold nanosheet placed on a Si (111) wafer. Curves 1 and 2 in Figure 3.6A represent the chemically distinct species of the C1s peak and have been obtained through deconvolution. The components are probably due to the hydrocarbon chain from the anthracene molecule and due to the trapped solvent chloroform present in the gold nanosheet at binding energy 285 and 288.4 eV respectively. Figure 3.6B shows the Au4f core level spectrum with the binding energy centred at 84.4 eV. The spectrum has been decomposed into 2 spin-orbit pairs corresponding to $4f_{7/2}$ and $4f_{5/2}$ (splitting factor ~ 3.98eV), which suggest that along with reduced Au, some amount of unreduced gold is also present at the interface.

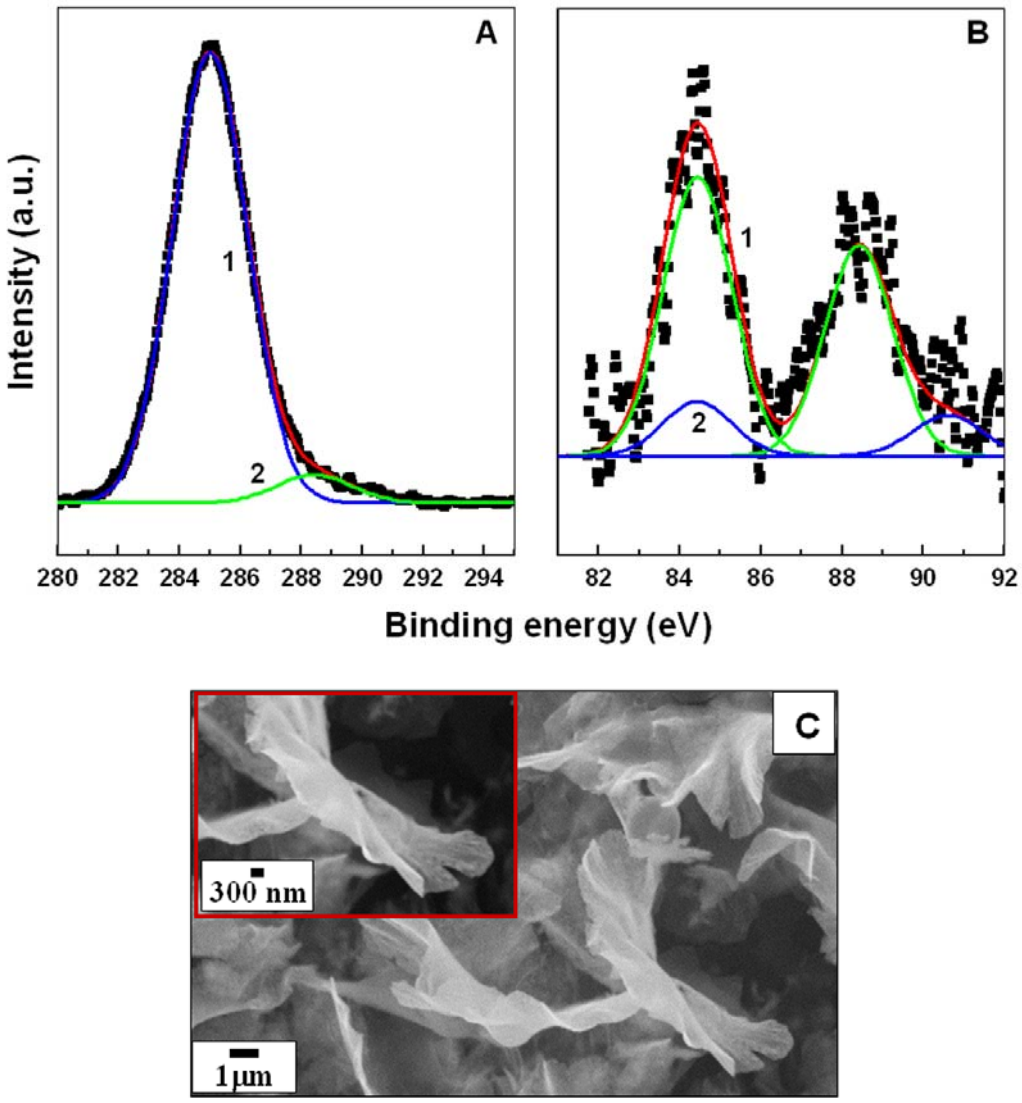

Figure 3.6*: A) C 1s core level spectrum recorded from film of gold nanosheet taken carefully on a Si (111) substrate together with the chemically distinct stripped components (curves 1 and 2). B) Au 4f core level spectrum recorded from the gold nanosheet with two pairs of deconvoluted curves. C) Representative SEM image of the gold nanosheet synthesized at the liquid-liquid interface. The inset in C shows a magnified image of one sheet having fringes.*

One additional SEM image of Figure 3.6C very aptly exhibits the nature of the gold nanosheet. The thickness of the sheet is probably due to the restricted reduction of gold ions at the 2D liquid-liquid interface as is evident from the highly magnified SEM image (inset of Figure 3.6C) showing a single sheet on top of the other.

3.2.5 Summary

To summarise, it has been demonstrated that thin nanosheets of gold may be formed by the reduction of aqueous chloroaurate ions at a liquid-liquid interface bearing anthracene anions. The anthracene anions have been created by electron transfer from Keggin ions that were reduced by irradiation with UV light. A control experiment was performed wherein aqueous chloroauric acid solution was vigorously stirred with a chloroform solution of anthracene bypassing steps 1-3 in our protocol (scheme in Figure 3.1). No reduction of the $AuCl_4^-$ ions was observed clearly indicating that electron transfer from UV-irradiated Keggin ions to anthracene is the crucial step in obtaining a two-dimensional reducing interface. This strategy opens up the exciting possibility of using anthracene anions in the synthesis of nanomaterials of variable morphology.

3.3 Synthesis of platinum nanosheets at the liquid-liquid interface

In a very similar approach, we tried synthesizing platinum nanosheets at the liquid-liquid interface using anthracene and Keggin ions. The reaction was carried out in a similar manner except that aqueous chloroplatinic acid solution was used. After the formation of the film of anthracene anion and its corresponding addition to chloroplatinic acid, the reduction of the $PtCl_6^{2-}$ ions to Pt^0 was not as fast as compared to that in the previous case for Au^0. This might be due to the lower reduction potential of the $PtCl_6^{2-}$/ Pt^0 couple as compared to that for the reduction of gold. However, a similar black film was obtained at the interface, which was lifted onto carbon coated Cu grids for TEM, and silicon wafers for further analysis.

3.3.1 Transmission Electron Microscopy (TEM) studies:

Figure 3.7A-D show representative TEM images of the platinum sheets formed at the interface of anthracene in chloroform and chloroplatinic acid.

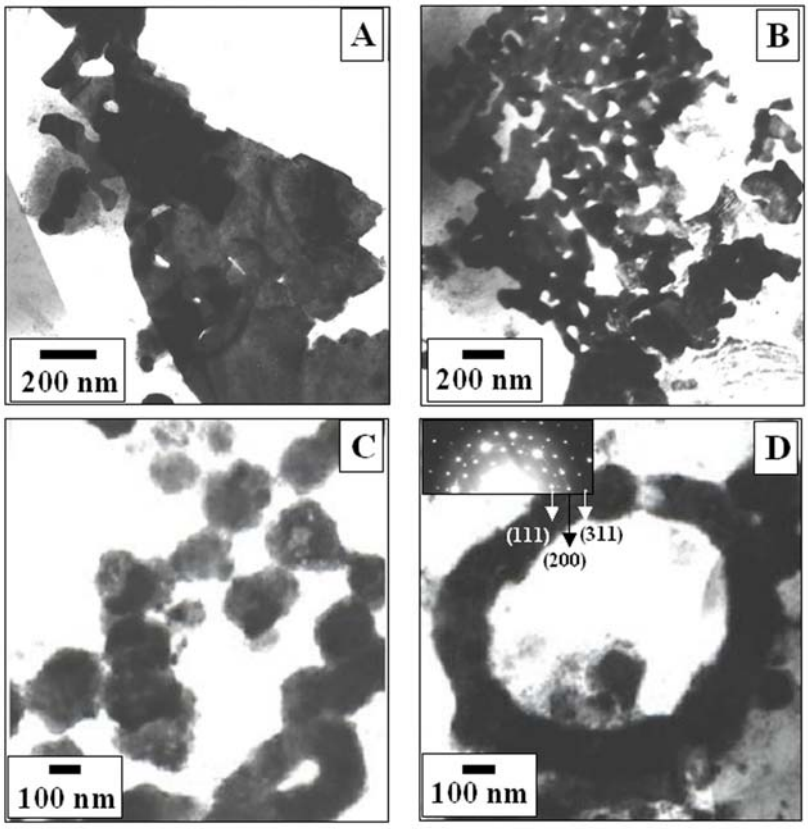

Figure 3.7: *Representative TEM images of the platinum nanoparticles/ nanosheets grown at the interface of $CHCl_3$ and water taken at different magnifications (Figure A-D). The inset shows the selected area electron diffraction (SAED) pattern from the ring in Figure D.*

The sheets formed are very thin and look similar to the gold nanosheets shown in Figure 3.3A-D. However, it appears that the film essentially consists of a single large sheet (Figure. 3.7A), along with some individual nanoparticles strewn here and there (Figure 3.7C). This suggests that the reduction is not yet complete and some particles have clustered together and are in the process of formation of sheet (Figure 3.7C). The inset of Figure 3.7D shows the selected area electron diffraction (SAED) pattern taken from the ring shaped cluster shown in Figure 3.7D. The spots have been indexed and match well with the fcc unit structure of Pt (PCPDF File No. 040802, $a=b=c=3.923$).

3.3.2 XPS measurements

In order to get an idea about the components present in the system, the Pt-anthracene films were deposited on Si (111) substrates and were analyzed by XPS. Figure 3.8 shows the C1s core level spectrum which has been decomposed into 3 chemically distinct components represented by curves 1, 2 and 3.

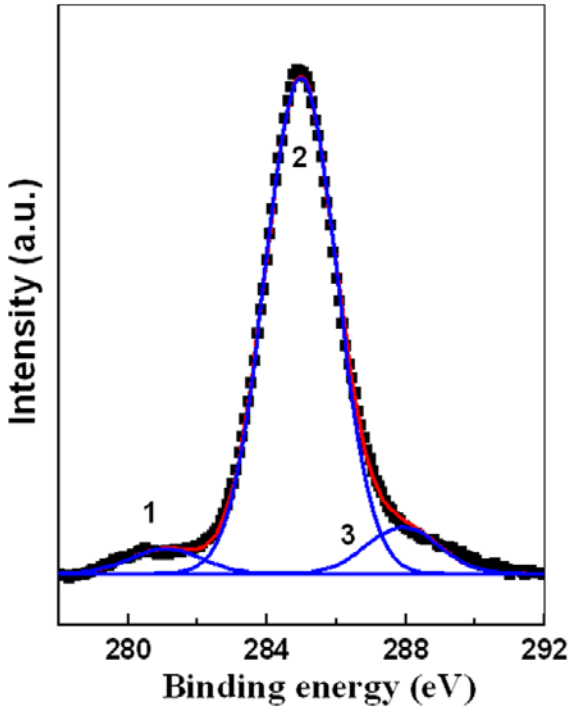

Figure 3.8: *C 1s core level spectrum recorded from a film of platinum nanosheet taken on a Si (111) wafer. The peak has been deconvoluted into 3 distinct chemical species (Curves 1, 2 and 3).*

The lower binding energy curve at 280.4 eV could be due to the presence of unreduced anthracene anion that might have been entrapped into the platinum film. Figure 3.9 shows the Pt 4f core level spectra which on deconvulation yielded 4 components, two components at 73 eV and 76.3 eV are assigned to metallic Pt(0) $4f_{7/2}$ and $4f_{5/2}$ respectively while the higher energy components at 75.4 eV and 78.6 eV correspond to unreduced Pt(+IV) $4f_{7/2}$ and $4f_{5/2}$ respectively, clearly indicating the presence of metal nanoparticles as well as Pt(IV) ion in the film.

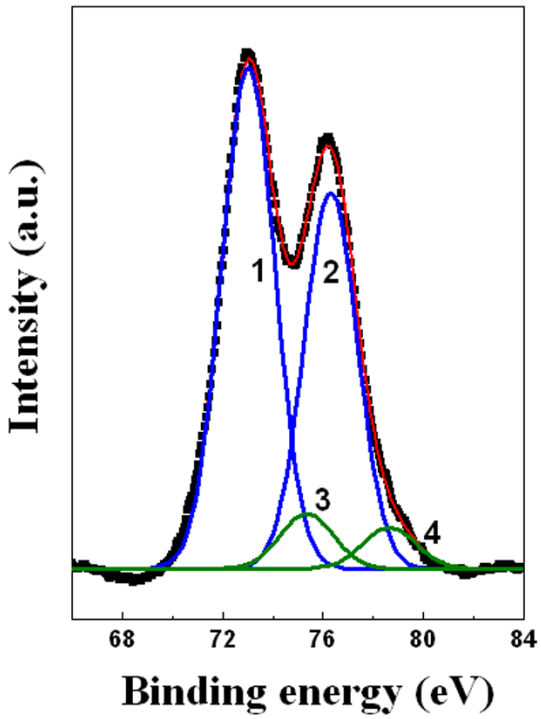

Figure 3.9: *Pt 4f core level spectrum deconvoluted into 2 pairs of spin-orbit pairs (Curves 1-4) recorded from the platinum film taken on a Si (111) substrate.*

3.3.3 Summary

In conclusion, it has been demonstrated that through a similar reaction approach platinum sheets can be obtained at the liquid-liquid interface. The photoreduced Keggin ions on vigorous shaking transfer their excess electrons to the anthracene moiety. The organic layer containing anthracene anions, thus, when added to aqueous chloroplatinic acid solution reduces the platinum ions at the liquid-liquid interface forming flat nanostructures. However, the reaction is not as fast as in the case of reduction of gold and some strewn particles of platinum are also obtained along with the sheet at the interface.

3.4 Synthesis of gold nanosheets at the interface of octadecyl amine (ODA) and Keggin ions

In a typical experiment, 10 ml of 10^{-3} M aqueous solution of phosphotungstic acid ($H_3PW_{12}O_{40}$, from Aldrich Chemicals and used as-received) was added to 10 ml of 10^{-3} M aqueous solution of $HAuCl_4$. To this 10 ml of 10^{-3} M solution of ODA in toluene was

added and the biphasic mixture was kept for 1hr. Then, 1 ml of propan-2-ol was added, the solution was deaerated and this solution was finally irradiated by UV light (pyrex filter, > 280 nm, 450 W Hanovia medium pressure lamp) for 3 h. After irradiation, the aqueous solution turned to dark blue in colour with a brownish tinge probably due to the simultaneous reduction of Au^{3+} ions, the colour of which has been partially obscured by the reduced Keggin colour. This is shown in the test-tube image of Figure 3.10. It was also observed that a dark red colour film was formed at the interface. This membrane was carefully lifted onto various substrates for further analysis.

Figure 3.10: *Test-tube showing the thin film of gold sheet formed at the interface of ODA in toluene and a mixture of $HAuCl_4$ and Keggin ion (PTA) after UV irradiation.*

3.4.1 UV-Vis spectra and Transmission Electron Microscopy (TEM) measurements

Figure 3.11 shows the UV-Vis spectra taken after irradiation from both the layers containing chloroauric acid and Keggin ions in the aqueous medium and ODA in toluene as the organic layer. It can be seen from Figure 3.11A that a sharp peak arises at 529 nm in the aqueous layer. This suggests that gold has been reduced by the photo-reduced

Keggin ions. However, the organic layer shows a broad peak centred around 541 nm as is seen in Figure 3.11B. It might be possible that the gold nanoparticles formed have been phase transferred into the organic medium by ODA and have clustered together, resulting in the broad peak in the UV-Vis spectrum of Figure 3.11B. A look into the TEM image of Figure 3.12 taken from the organic layer shows that the gold nanoparticles formed are indeed somewhat clustered together. The presence and subsequent clustering of gold nanoparticles in the organic medium have resulted in the shifted peak at 540 nm.

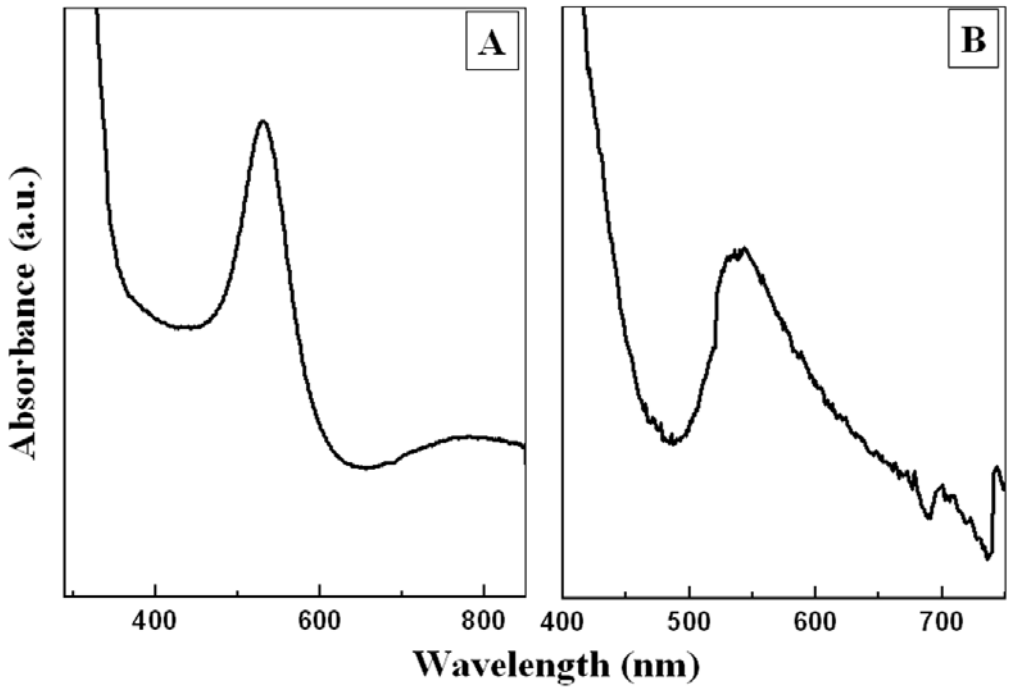

Figure 3.11: *UV-Vis spectra taken after irradiation for 3 hrs from the A) aqueous and B) organic layer containing 10^{-3} M each of PTA and $HAuCl_4$ in the aqueous layer and ODA in toluene in the organic layer.*

There have been previous reports by Weisbecker *et. al.* and K.Vijaya Sarathy *et. al.* where in the former case Self Assembled Monolayers (SAMs) were formed onto gold colloids via alkanethiols in 50 % ethanol solution [30, 31]. However, in the latter case quick phase transfer of gold nanoparticles synthesized in the aqueous phase into the organic phase by alkanethiols has been triggered by minute amounts of HCl.

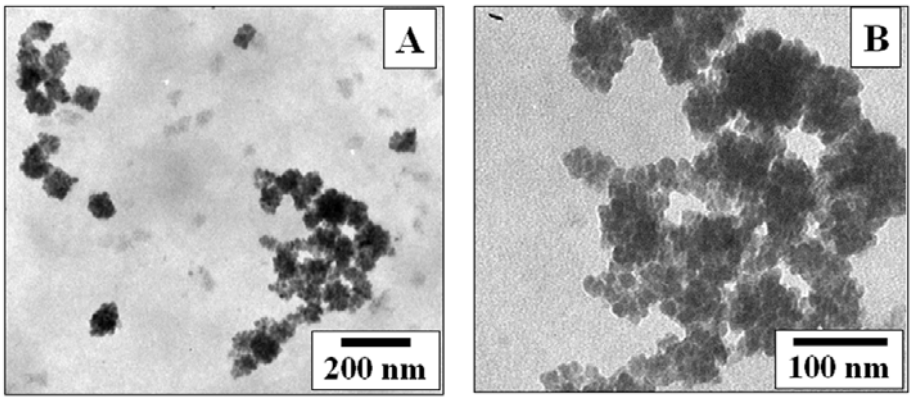

Figure 3.12: *A) and B) Representative TEM images taken from the organic layer of toluene containing gold nanoparticles that have been formed by the irradiation of 10^{-3} M aqueous $HAuCl_4$ and PTA solution and ODA in toluene. The particles in the organic phase seem to be partially clustered.*

There have been several reports by Rao *et al* where ultrathin nanocrystalline films of gold, alloys like Au-Ag, Au-Cu and compounds like CuO and CuS have been prepared [32]. In each of the experiments they have used an organometallic precursor in the organic medium and the reducing agent in the aqueous medium. Figure 3.13 shows representative TEM images of the membrane formed at the interface. The sheets are extremely thin and fragile and often separate out while lifting onto solid supports. It can be clearly seen from Figure 3.13A and B that flat nanostructures of gold have been formed. However, in addition to the flat sheet like structures gold nanoclusters are also present on top of these sheets. This can be clearly seen in Figure 3.13C and in the higher magnification image of Figure 3.13D. The inset of Figure 3.13D shows the selected area electron diffraction (SAED) pattern corresponding to the unit cell of fcc gold. The flat nanostructures are extremely thin, as the reaction has been constrained at the 2D liquid-liquid interface. It is most likely that ODA will preferentially bind to $HAuCl_4$ (size of molecule is small compared to PTA) at the interface, hence confined reduction occurs by the photo-reduced Keggin ions resulting in the formation of truly 2D nanostructures.

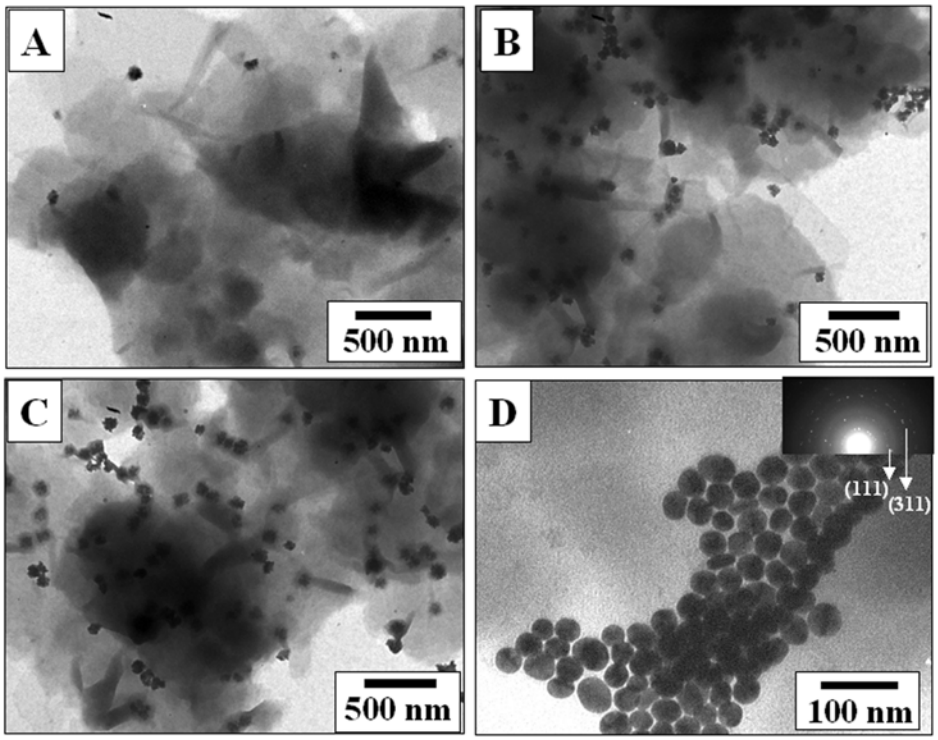

Figure 3.13: *A)-D) Representative TEM images taken from the gold nanosheet formed at the interface of $HAuCl_4$ and Keggin in aqueous solution and ODA in toluene medium. The inset shows the selected area electron diffraction pattern characteristic of fcc gold.*

3.4.2 Summary

In this brief work we have shown that flat nanostructures of gold can also be obtained by a completely different process whereby the reducing agent and the reductant acts in a restricted 2D environment. The sheets are often extremely thin which allows them to split into individual gold nanoparticles once the liquid-liquid interface is disturbed. However, since the reduction potential of Keggin ions is reasonably low (~-0.023V Vs SCE), the process should work well with the reduction of other metal ions.

3.5 Conclusion

In this chapter we have shown that thin nanosheets of gold may be formed by the reduction of aqueous chloroaurate ions at a liquid-liquid interface bearing anthracene anions. We have utilized a completely new methodology whereby electron transfer to the

reasonably electron rich species anthracene was carried out at room temperature by photoreduced Keggin ions. Owing to the excellent 2D network, similar to polymer structures, that the sheets possess, they can be studied and used further for separation techniques and immobilization. The process works well with platonic ions also. In another part of the work, we have shown that similar type of restricted growth of gold nanostructures is also possible by utilizing the electrostatic interaction of two charged species at the liquid-liquid interface.

3.6 References

[1] Chen, J. -F.; Wang, Y.-H.; Guo, F.; Wang, X.-M.; Zheng, C. *Ind. Eng. Chem. Res.* **2000**, *39,* 948.

[2] Tamil Selvan, S.; Hayakawa, T.; Nogami, M.; Kobayashi, Y.; Liz-Marza´n, L. M.; Hamanaka, Y.; Nakamura A. *J. Phys. Chem. B* **2002,** *106,* 10157.

[3] Garcia-Martinez, J. C.; Scott, R. W. J.; Crooks, R. M. *J. Am. Chem. Soc.* **2003**, *125*, 11190.

[4] Faraday, M. *Philos. Trans.* **1857**, *147*, 145.

[5] Turkevich, J.; Stevenson, P. C.; Hillier, J. *Disc. Faraday Soc.* **1951**, *11*, 55275.

[6] Turkevich, J.; Kim, G. *Science* **1970**, *169*, 873.

[7] Turkevich, J. *Gold Bull.* **1985**, *18*, 86291.

[8] Haruta, M.; Kobayashi, T.; Yamada, N. *Chem Lett*. **1997**, *405*,

[9] Elghanian, R.; Storhoff, J.J.; Mucic, R.C.; Letsinger, R.L.; Mirkin, C.A. *Science* **1997***, 277*, 1078.

[10] Wang, Y.; Xie, X.; Wang, X.; Ku, G.; Gill, K. L.; O'Neal, D. P.; Stoics, G.; Wang, L. V. *Nano Lett.* **2004**, *4*, 1689.

[11] Shafer-Peltier, K. E.; Haynes, C. L.; Glucksberg, M. R.; Van Duyne, R. P. *J. Am. Chem. Soc.* **2003**, *125*, 588.

[12] Jain, P. K.; Lee, K. S.; El-Sayed, Ivan H.; El-Sayed, Mostafa A**.** *J. Phys. Chem. B* **2006,** *110,* 7238.

[13] Brust, M.; Walker, M.; Bethell, D.; Schiffrin, D.J.; Whymann, R. *J.Chem.Soc. Chem.Commun.* **1994**, 801.

[14] (a) Selvakannan, PR.; Mandal, S.; Pasricha, R.; Adyanthaya, S.D.; Sastry, M. *Chem.Commun.* **2002**, 1334. (b) Mandal, S.; Selvakannan, PR.; Roy, D.; Chaudhari, R.V.; Sastry M. *Chem. Commun.* **2002**, 3002.

[15] Chang, J-Y; Wu, H.; Chen, H.; Ling, Y-C; Tan, W. *Chem. Commun.* **2005**, 1092.

[16] Tsujia, M.; Hashimoto, M.; Nishizawa, Y.; Tsuj, T. *Materials Letters* **2004**, *58*, 2326.

[17] Liao, H.; Hafner, J. H. *J. Phys. Chem. B* **2004,** *108,* 19276.

[18] Ongaro, A.; Griffin, F.; Beecher, P.; Nagle, L.; Iacopino, D.; Quinn, A.; Redmond, G.; Fitzmaurice, D. *Chem. Mater.* **2005**, *17*, 1959.

[19] Chunxin Ji and Peter C. Searson *J. Phys. Chem. B* **2003,** *107,* 4494.

[20] Me´traux, G. S.; Charles C., Y.; Jin, R.; Mirkin C. A. *Nano Lett.* **2003**, *3*, 519.

[21] Millstone, J. E.; Park, S.; Shuford, K. L.; Qin, L.; Schatz, G. C.; Mirkin, Chad A. *J. Am. Chem. Soc.* **2005**, *127*, 5312.

[22] Shiv Shankar, S.; Rai, A.; Ahmad, A.; Sastry, M. *Chem. Mater.* **2005,** *17,* 566.

[23] Xu, X.; Stevens, M.; Cortie, M. B. *Chem Mater.* **2004**, *16*, 2259.

[24] Pike, J.K.; Byrd, H.; Morrone, A.A.; Talham, D.R. *J.Am.Chem.Soc.* **1993**, *115*, 8497.

[25] Swami, A.; Kumar, A.; Selvakannan, PR.; Mandal, S.; Pasricha, R.; Sastry, M. *Chem.Mater.* **2003**, *15*, 17.

[26] Huheey, J. E. *Inorganic Chemistry*, **(Third Edition)**, 698.

[27] Schiedt, J.; Weinkauf, R. *Chem.Phys.Lett.* **1997**, *266*, 201.

[28] Papaconstantinou, E. *Chem. Soc. Rev.* **1989,***18*,1.

[29] Pe´rez-Maqueda, L. A.; Matijevic, E. *Chem. Mater.* **1998**, *10,* 1430.

[30] Weisbecker, C. S.; Merritt, M. V.; Whitesides, G. M. *Langmuir* **1996,** *12*, 3763.

[31] Sarathy, K. V.; Raina, G.; Yadav, R. T.; Kulkarni, G. U.; Rao, C. N. R. *J. Phys. Chem. B.***1997,** *101*, 9876.

[32] (a) Agrawal, V. V.; Kulkarni, G. U.; Rao, C. N. R. *J. Phys. Chem. B.*, **2005**, *109*, 7300. (b) Gautam, U. K.; Ghosh, M.; Rao, C. N. R. *Langmuir*, **2004,** *20*, 10775. (c) Agrawal, V. V.; Mahalakshmi, P.; Kulkarni, G. U.; Rao, C. N. R. *Langmuir*, **2006**, 22, 1846.

CHAPTER IV

Synthesis and assembly of metal nanoparticles using Keggin-amino acid hybrid structures

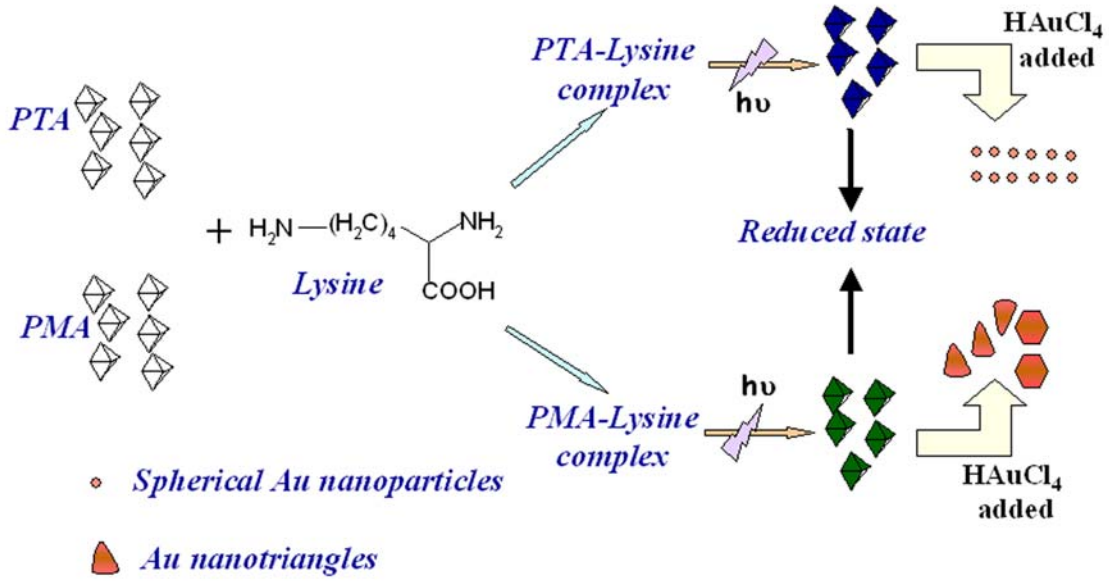

We observe strong interaction between the cationic amino acid lysine and the PTA anion that leads to the formation of crystalline lysine-phosphotungstate colloidal particles of interesting fibre-like morphology of micron dimensions. The fibres when irradiated and added to $HAuCl_4$ leads to the formation of linear assemblies of gold nanoparticles on the underlying lysine-PTA colloidal fibres acting as active templates. The electrostatic complexation of Keggin ion with various amino acids was also studied to bring out a plausible mechanism for the reaction. In another experiment following the reaction in a similar way by just altering the Keggin ion (phosphomolybdic acid taken), the formation of gold nanotriangles having a high degree of anisotropy has been shown.

Part of the work presented in this chapter has been published:

1) Sanyal, A.; Mandal, S.; Sastry, M. *Adv. Funct. Mater.* **2005**, *15*, 273. 2) Sanyal, A.; Sastry, M. *Langmuir* **2006**, (communicated).

4.1 Introduction

There is increasing scientific interest in materials chemistry in controlling the architecture, morphology and patterning of inorganic materials at dimensions from the nano- to macroscopic length scales by mimicking the process of biomineralization. Miniaturization of bulk structures is one of the exciting fields of contemporary research, as there exists a wealth of fascinating and superior properties that have great impact not only in terms of applicability but also in the basic understanding of physical and chemical properties of these nanostructures. Some of these pronounced properties, different from the bulk counterparts, include optical resonance, size-dependent excitation or emission, conductivity and magnetic properties. While particle size is an important factor in controlling the optical [1] and chemical properties of nanoscale matter [2], it is also recognized that the shape of nanoparticles adds an additional degree of freedom in modulating these properties [3]. Tuning the properties such as particle size and shape by use of suitable reducing agents has resulted in the synthesis of various shapes such as rods [4], wires [5], nanoplates [6-8], nanodisks [9-11] and nanoprisms [12-15] possessing significant anisotropy. Recently the synthesis of one-dimensional nanostructures such as nanotubes, nanowires, nanorods has stimulated intense interest due to the potential use of these nanostructures in advanced technologies [16-18]. For example, high-aspect ratio nanofibres from cheap and commonly available inorganic materials can be used as polymer filler materials for the alteration of a material's mechanical and rheological properties [19].

Nanotectonics is thus the emerging science that deals collectively with the synthesis and assembly of inorganic nanoparticles into higher-order superior architecture. One of the very efficient methods of such bottom-up approach is through template-mediated assembly which include incorporation of nanoparticles onto organized interiors such as tobacco mosaic virus (TMV) [20] carbon nanotubes [21,22], colloidal crystals [23], coated polymer beads [24] and bacterial membranes [25]. Synthesis of hierarchical ordered inorganic framework materials using different templates is of great importance because of their applications in catalysis [26] separation techniques [27] and materials chemistry. Synthesis of highly ordered technologically functional hierarchical materials finds application also in magnetic storage devices due to a property better known as giant

magneto-resistance and in nanobiology. Abalone shell is one such example of a layered structure in biology which is tougher than each of is constituents [28]. Of late, coordination polymers have emerged as a new class of organic-inorganic hybrid materials where some metal ion is linked to a bridging organic ligand at room temperature [29]. Over the last decade researchers have also used organic compounds as templates for the generation of inorganic structures and materials [30,31]. Several kinds of organic additives have been used as crystal modifiers to direct the nucleation and growth of barite from aqueous solution [32,33] Recently Qi and co-workers have synthesized one-dimensional nanostructures in reverse micelles of mixed surfactants [34,35]. Mann and co-workers have also prepared $BaCrO_4$ nanofilaments using AOT microemulsions [36]. Qi and co-workers have recently synthesized silver nanowires by mild chemical reduction of silver nitrate in aqueous solution of poly(methacrylic acid) [37] Yu *et al*. have shown the $BaCrO_4$ and $BaSO_4$ nanofibres can be synthesized using sodium polyacrylate [38]

Polyoxometallates (POM) are one of the most widely used inorganic components in the design of hybrid materials due to their potential application in catalysis, sorption, magnetism, and photochemistry. Matijevic *et al.* have shown that salts of Keggin ions with cesium [39], thorium and zirconium [40] cations can form uniform micron-sized spherical colloidal particles in aqueous medium. Keggin ions form a subset of polyoxometalates and have the general formula $(XM_{12}O_{40})^{(8-n)-}$, where 'M' stands for W or Mo and 'X' stands for heteroatoms such as P, Si, Ge with *n* being the valency of X [41] as was described in a previous chapter. The Keggin ions, accompanying cations and other components such as water are arranged in a well-defined secondary three-dimensional structure, the stability of which depends on the nature of counterions, amount of water etc [42]. Owing to the multifunctional properties of Keggin ions like large size, photochemical reducing capability, electron transfer, stability etc., they have been used in an extensive range of applications like catalysis [43], protonic conductors [44] and even as drug for antitumor and antibacterial activities [45]. Keggin ions undergo stepwise multielectron redox processes without undergoing a structural change [46]. They may be reduced electrolytically, photochemically and with suitable reducing agents. A fascinating thing about this is that the reduction occurs without appreciable disruption to

the original Keggin structure and with the addition of a particular number of electrons. The reduced form of these polyoxometallates is essentially coloured deep blue, hence often carrying the name of "heteropoly blues" [47]. Troupis, Hiskia and Papaconstantinou have shown that photochemically reduced polyoxometallates of the Keggin structure [$(PW_{12}O_{40})^{3-}$ and $(SiW_{12}O_{40})^{4-}$] when exposed to aqueous metal ions such as Ag^{+}, $AuCl_4^{-}$, Pd^{2+} and $PtCl_6^{2-}$ resulted in the formation of the corresponding metal nanoparticles of reasonable monodispersity [48]. Recently, Sastry and co-workers have used phosphotungstic acid (PTA) as a UV-switchable reducing agent for making phase-pure core-shell nanoparticles. They have also shown that semiconductor CdS nanoparticles and star-shaped $CaCO_3$ nanoparticles can be synthesized [49].

The above-mentioned work provided the impulse for exploring further the reactivity and interaction of Keggin ions with cationic species. There have been quite a few attempts to study the interaction of polyoxometallates with amino acids where scientists have tried to figure out the nature of binding and the related crystal structure [50]. In this chapter we look at such organic-inorganic hybrid structures by studying the interaction of Keggin ions with amino acids. Amino acids at the pH of the Keggin ion solution are expected to be positively charged which further boost the electrostatic complexation ability between the two species. We have observed strong interaction between cationic L-lysine and the PTA anion that leads to the formation of crystalline lysine-phosphotungstate colloidal particles of interesting fibre-like morphology of micron dimensions. Owing to the good photoreduction capability of Keggin ions we thereafter use these fibre- like structures as scaffolds for the assembly of gold nanoparticles. We further show, in this chapter, that both electrostatic charge as well as stereochemical arrangement with respect to amino acids is responsible for the formation of such long hybrid nanostructures. This supposition is well attested when the same reaction carried out in the presence of a different Keggin (phosphomolybdic acid) resulted in the formation of anisotropic gold nanotriangles.

4.2 The formation of phosphotungstic acid-lysine composite

4.2.1 Synthesis and assembly of gold nanoparticles on quasi-linear Keggin ion-lysine hybrid nanostructures

In a typical experiment, 20 ml of 10^{-3} M aqueous solution of phosphotungstic acid [PTA, $H_3(PW_{12}O_{40})$] obtained from Aldrich as a solid powder and used as-received was mixed in a test tube along with 20 ml of 10^{-3} M aqueous solution of lysine amino acid (L-lysine) and was kept for 1 hour (shown as step 'A' in the scheme of Figure 4.1 and test-tube 'A' in the inset of Figure 4.2).

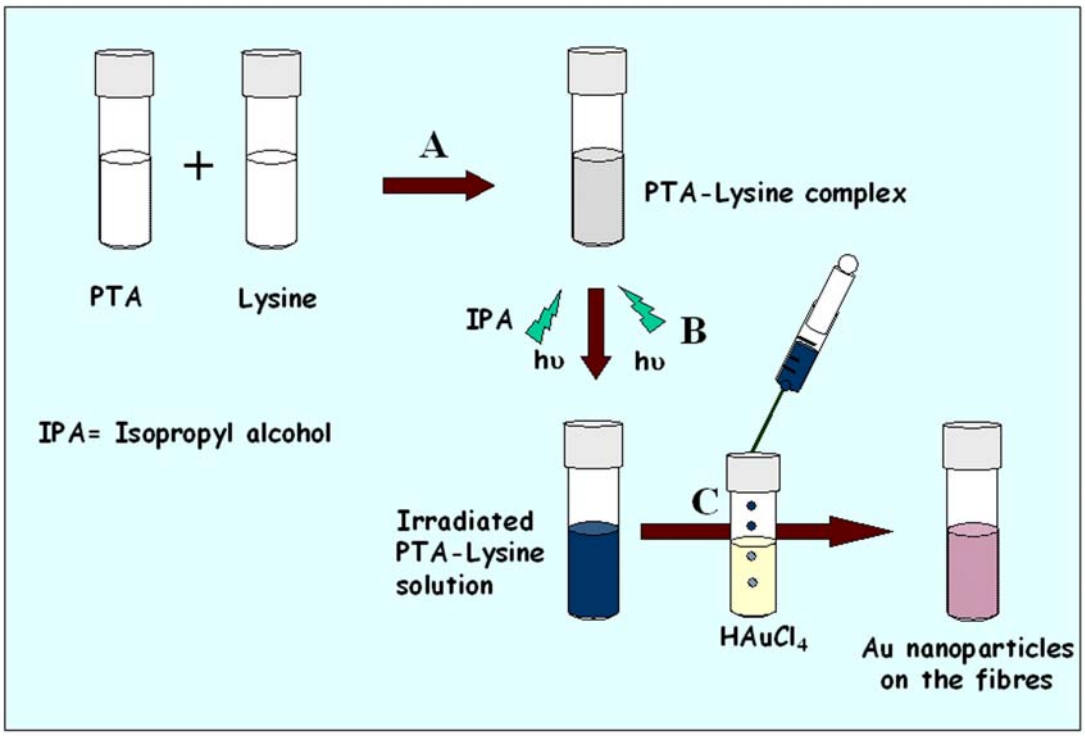

Figure 4.1: *Scheme showing the formation of Au nanoparticles on the PTA-Lysine template in steps (A)-(C): Step (A) PTA-Lysine solution mixed and kept for 1 hr. Step (B) PTA-Lysine complex irradiated for 3 hrs. Step (C) 5ml of irradiated PTA-Lysine (dark blue colour) solution was injected into 5 ml of $HAuCl_4$.*

To 30 ml deaerated aqueous solution of L-lysine and phosphotungstic acid, 2 ml of propan-2-ol was added and the mixture irradiated by UV light for 3 h (pyrex filter, > 280 nm, 450 W Hanovia medium pressure lamp). This leads to the reduction of $(PW_{12}O_{40})^{3-}$ ions present in the lysine-phosphotungstate (lysine-PTA) complex and can be seen as a

blue color appearing in the solution (step 'B' in the scheme of Figure 4.1 and test-tube 'B' in the inset of Figure 4.2). To 5 ml of 10^{-4} M $HAuCl_4$ solution, 5 ml of this irradiated L-lysine-PTA solution was added under continuous stirring for 10 minutes and then allowed to age for 2 h. The color of the solution changed from blue to pink indicating formation of gold nanoparticles (step 'C' in Figure 4.1 and test-tube marked 'C' in the inset of Figure 4.2). Samples were prepared for various characterization techniques like SEM, XPS, FTIR, TEM and XRD by drop-coating films on Si (111) wafers, copper grids and glass slides from the lysine-PTA solutions at different stages, viz. before UV-irradiation, after UV-irradiation and after formation of gold nanoparticles on the lysine-PTA template.

4.2.2 UV-Vis spectroscopy measurements

Figure 4.2 shows the UV-Vis spectra recorded from mixtures of aqueous solutions of 10^{-3} M PTA and 10^{-3} M lysine at different stages of treatment. Prior to UV-irradiation, it is observed that there is no absorption in the visible region of the electromagnetic spectrum (curve 1, Figure 4.2, and test-tube 'A' in the inset of Figure 4.2). This is due to the O-M charge-transfer bands in the near visible and UV region [47] which is also corroborated from the colourless nature of the solution. The UV-vis absorption spectrum recorded after UV-irradiation of the aqueous solution of lysine-PTA complex for 3 h is shown as curve 2 in Figure 4.2 (step B in the scheme of Figure 4.1 and test-tube 'B' in Figure 4.2). The UV-Vis spectrum of this solution shows the presence of a broad absorption band at 760 nm that is characteristic of one-electron reduced PTA $[PW_{12}O_{40}]^{4-}$. This absorption is due to the forbidden *d-d* transition and also due to the Intervalent Charge Transfer (IVCT) band that gives the solution a deep blue colour [47]. The UV-Vis absorption spectrum recorded after addition of aqueous solution to $HAuCl_4$ solution to the UV-irradiated lysine-PTA colloidal particle solution is shown as curve 3 in Figure 4.2 (test-tube 'C' in Figure 4.2).

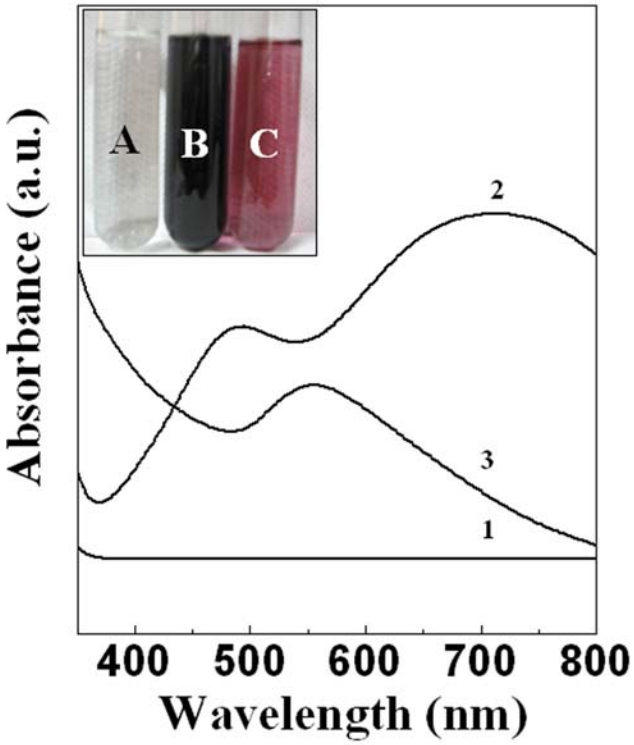

Figure 4.2: *UV-VIS spectra recorded from: curve 1– aqueous mixture of 10^{-3} M phosphotungstic acid and 10^{-3} M amino acid lysine solutions before UV irradiation; curve 2– after UV-irradiation of the lysine-PTA solution for 3 h; curve 3 – after addition of aqueous solution of 10^{-4} M $HAuCl_4$ into the UV-irradiated lysine-PTA solution. The inset shows the test-tubes of solutions containing 'A': PTA-lysine; 'B': UV-irradiated PTA-lysine and 'C': Irradiated PTA-lysine added to 10^{-3} M $HAuCl_4$.*

It is seen from this spectrum that a fairly sharp absorption band centered at 555 nm arises. This absorption band is characteristic of gold nanoparticles and arises due to excitation of surface plasmon resonance in gold nanoparticles [51].

4.2.3 Fourier Transform Infra-Red (FTIR) spectroscopy measurements

Figure 4.3 represents the Fourier transform infrared (FTIR) spectra in the region 600-1200 cm^{-1} for pure phosphotungstic acid (curve 1) and lysine-PTA solution after mixing of lysine with phosphotungstic acid (curve 2). Curve 1 shows the W-O asymmetric stretching vibration frequency at 952 cm^{-1}, W-O-W bending vibration at 874.5 cm^{-1} and the P-O asymmetric stretching vibration at 1073 cm^{-1} for pure phosphotungstic acid. After complexation of lysine with PTA (curve 2), we observe a

shifted W-O bond stretching vibration at 894 cm^{-1}, and a W-O-W bending vibration at 840 cm^{-1} indicating salt formation of phosphotungstic acid with lysine molecules. The position of these vibration bands is in good agreement with those obtained by Perez-Maqueda, Matijevic [39] and Sastry and co-workers [52] for PTA anions complexed with metal cations. Since the isoelectric point (pI) lysine is 9.7 and the pH of phosphotungstic acid (PTA) solution is 2.5, during mixing of the lysine and PTA solutions it is expected that the lysine molecules will be fully protonated.

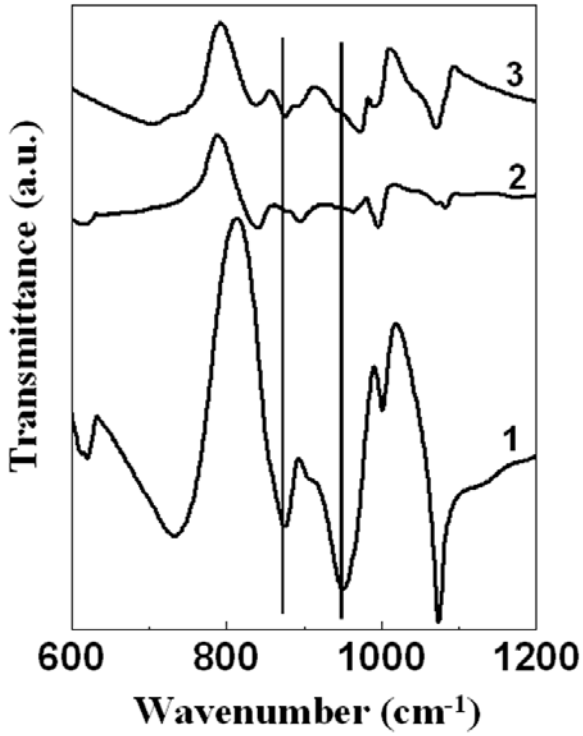

Figure 4.3: *FTIR spectra recorded from drop-coated films on Si (111) wafers of pure PTA solution (curve 1); lysine-PTA solution (curve 2) and after synthesis of gold nanoparticles by addition of 10^{-4} M $HAuCl_4$ solution to UV-irradiated lysine-PTA solution (curve 3).*

This would lead to strong electrostatic complexation of the cationic lysine and PTA anions in solution. Curve 3 in Figure 4.3 represents the FTIR spectrum recorded in the region 600-1200 cm^{-1} from the UV-irradiated gold-lysine-PTA colloidal particles after reaction with gold ions. Comparing curve 3 with curves 1 and 2, it is seen that the positions of the W-O asymmetric stretching and the W-O-W bending vibration bands occur at almost the same wavenumbers as that observed for pure PTA (curve 1).

4.2.4 Isothermal Titration Calorimetric and Conductivity measurements

In order to estimate the strength of the interaction between lysine and PTA, isothermal titration calorimetric (ITC) measurements were performed. ITC is an extremely powerful thermodynamic technique that has been used with much success in understanding biomolecular-binding processes [53-57]. However, this technique is yet to be used to study interactions between inorganic reactants and to our knowledge, this study is one of the first in this direction. Figure 4.4A shows the ITC titration curve recorded during injection of 10 μl of lysine ($4x10^{-2}$ M) from a syringe into 1.47 ml of PTA solution (10^{-3} M) taken in a sample cell. The upper frame of Figure 4.4A shows the raw data obtained in the ITC experiment showing clearly a strong exothermic reaction, where each peak in the figure is the result of a single injection. The exothermicity of the first few peaks is roughly the same since during the initial stages of reaction between lysine and PTA, a number of binding sites are vacant. As the injections progress, the number of binding sites decreases continuously until saturation occurs after roughly 25 injections. The plot shown in the lower frame of Figure 4.4A is the binding isotherm determined from the raw data, where the total heat per injection (kcal per mole of lysine injected) is plotted against the molar ratio of lysine to PTA in the titration cell, this data having been analyzed using Origin (***Microcal***) software (solid line fit to the data). The precise shape of the binding isotherm contains all the information necessary to completely characterize the binding reaction. The isotherm has been fitted using a two-site binding model whereby corresponding values of the binding constant (K= 355.3 M^{-1}), enthalpy (ΔH = -2519 kcal/mol) and stoichiometry (n = 1.5) have been estimated. It is observed that the value of binding constant (K) is 355.3 M^{-1}, thus indicating that the strength of binding between lysine and PTA is quite high. The value of n is 1.5, which means that for 2 PTA molecules, 3 lysine ligands are bound and essentially gives the stoichiometry of the reaction. The change in enthalpy (ΔH= -2519 kcal/mol) is also quite high further supporting the strong binding of lysine molecules with PTA.

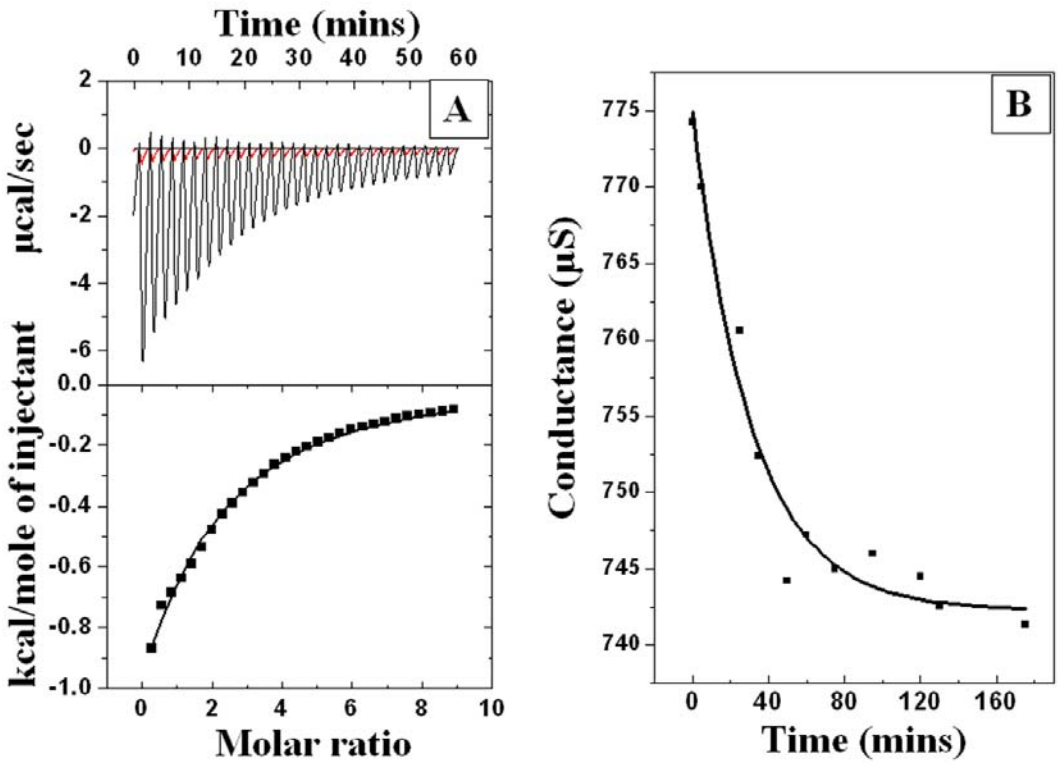

Figure 4.4: *(A) Upper frame - isothermal titration calorimetric data recorded during successive injections of 10 µl aqueous lysine solution into the titration cell containing 1.47 ml of aqueous phosphotungstic acid solution. The data in red corresponds to the ITC response recorded during titration of L-lysine against deionized water with pH adjusted to 3 using acetic acid. The lower frame shows the binding isotherm obtained by integration of the raw data shown in the upper panel after conversion to molar ratio of the reacting lysine and PTA in the titration cell. The solid line is based on a 2-site binding model for the lysine-PTA reacting species. (B) Solution conductivity measured as a function of time of mixing equi-volume aqueous solutions of 10^{-3} M lysine and 10^{-3} M phosphotungstic acid. The solid line corresponds to an exponential decay curve fitted to the experimental data points.*

During complexation of lysine with PTA anions, it is expected that the mobility of ions in solution would decrease. Figure 4.4B shows the conductance of the lysine-PTA reaction mixture measured as a function of time of reaction. It is seen that the solution conductivity decreases steadily and saturates after ca. 2 h of reaction and thus is an estimate of the optimum time of reaction for formation of lysine-Keggin ion colloidal particles (vide infra). The conductance value of 10^{-3} M aqueous PTA is 1.240 mS while that for 10^{-3} M lysine is 112.40 µS (data not shown in the graph).

4.2.5 X-Ray Photoelectron Spectroscopy (XPS) measurements

Figure 4.5 A-C show the X-ray photoemission spectroscopy (XPS) C1s, N1s and W 4f core level spectra recorded from a drop-coated film of the lysine-PTA solution on a Si (111) substrate respectively.

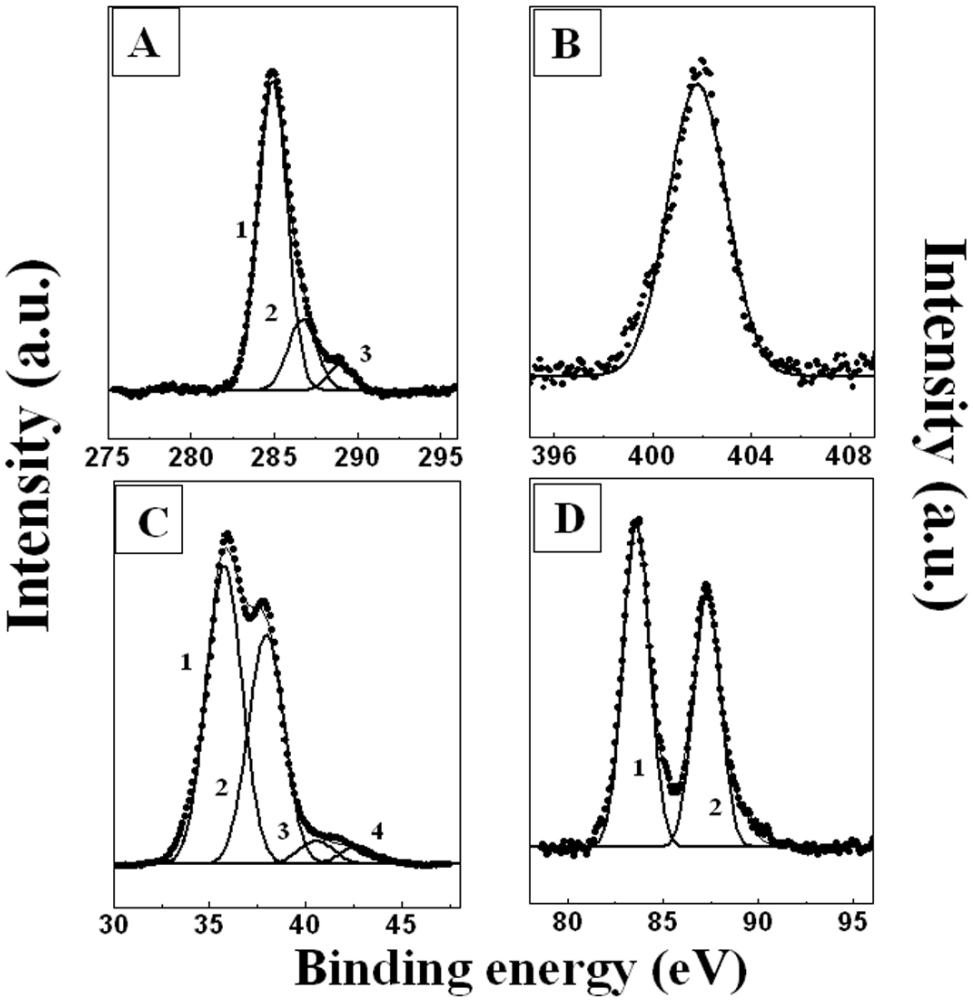

Figure 4.5: *(A) C 1s core level spectrum recorded from a drop-cast film of the lysine-PTA solution on a Si(111) substrate together the chemically distinct stripped components (1-3). (B) N 1s core level spectrum recorded from a drop-cast film of the lysine-PTA solution on a Si(111) substrate. (C) W 4f core level spectrum recorded from a drop-cast film of the lysine-PTA solution on a Si(111) substrate together with 2 chemically distinct spin-orbit pairs (1,2 & 3,4). (D) Au 4f core level spectrum recorded from the gold nanoparticles synthesized by the reaction of UV-irradiated lysine-PTA solution with aqueous 10^{-4} M $HAuCl_4$. Peaks 1 & 2 correspond to a single spin-orbit pair in the Au 4f spectrum.*

In Figure 4.5A, curves 1, 2 and 3 correspond to the chemically distinct C 1s core levels originating from the hydrocarbon chains, α-carbon and –COOH groups present in the lysine molecules in the lysine-PTA complex with binding energies of 285, 286.6 and 289 eV respectively. Figure 4.5B shows the N 1s core level spectrum with a peak centered at binding energy of 401.8 eV. This value is higher than the normal N 1s core level binding energy from alkylamines [58] indicating that the amine groups in lysine are protonated. It is observed that the ratio of the normalized areas of N 1s and –COOH carbon signals (area under curve 3 in Figure 4.5A; areas corrected for the ionization cross sections of the corresponding elements) is 1: 2.3 which is in good agreement with the number of carboxylic groups and amine groups present in the lysine molecule (1: 2). Figure 4.5C shows the W 4f spectrum recorded from the lysine-PTA film. This spectrum could be resolved into 2 spin-orbit pairs (splitting ~ 2.18 eV) with a $4f_{7/2}$ binding energy (BE) of 35.76 eV (curve 1 in Figure 4.5C). The presence of 2 pairs signify that W is likely to be present in two different oxidation states (W^{5+} and W^{6+}). Figure 4.5D shows the Au 4f core level spectrum recorded from a film of gold nanoparticles synthesized by reduction of $AuCl_4^-$ ions by UV-irradiated lysine-PTA solution. The Au 4f spectrum could be resolved into a single spin-orbit pair (splitting ~ 3.71 eV) with a $4f_{7/2}$ binding energy (BE) of 83.6 eV (curve 1 in Figure 4.5D). There was no evidence for additional components in the Au 4f spectrum, which indicates the complete reduction of the $AuCl_4^-$ ions by the UV-irradiated lysine-PTA colloidal particles.

4.2.6 Scanning Electron Microscopy (SEM) measurements

Figure 4.6A and B show representative scanning electron microscopy (SEM) images recorded at different magnifications from a drop-coated film of the mixture of aqueous solutions of PTA and lysine on a Si (111) substrate. Densely populated bundles of the lysine-PTA complex are seen on the surface of the substrate. The structures exhibit well-defined morphology that appears to be predominantly fibre-like. The bundles of nanofibres of lysine-PTA complex resemble crossed haystacks and most of the nanofibres seemed to grow from single starting points with a smooth growth front (Figure 4.6A). The nanofibres are roughly 100-150 μm in length and possess a high aspect ratio. It would be quite interesting to understand whether the stereochemistry of the amino acid

plays a major role in directing the morphology of the lysine-PTA nanofibre structure or not. Therefore this experiment was performed with D-lysine to check whether the morphology of lysine-PTA complex is a function of the stereochemistry of the amino acid.

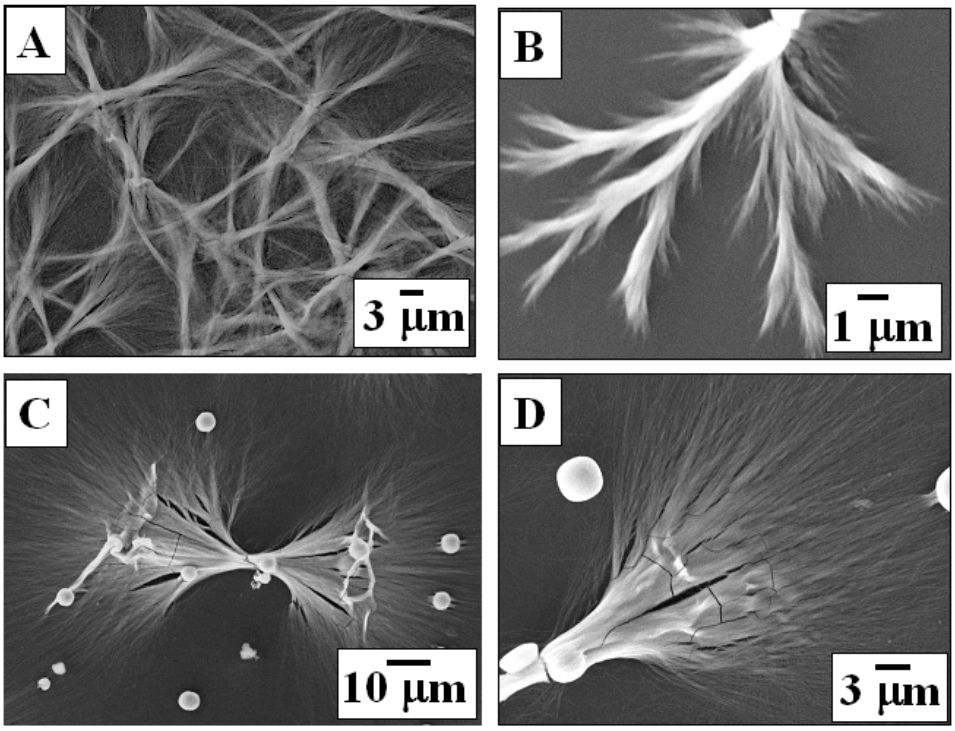

Figure 4.6: *Representative SEM images of drop-cast films of the amino acid-PTA solution on a Si(111) substrate before UV-irradiation using (A) L-lysine and (B) D-Lysine. (C) and (D) – Representative SEM images drop-cast films of the lysine-PTA solution on a Si(111) substrate after UV-irradiation.*

Figure 4.6B shows a representative SEM image of drop-coated film of D-lysine and PTA complex taken on a Si (111) substrate. The image shows no discernible change in the overall morphology of the nanocomposite structure relative to that formed with L-lysine as the counterion, i.e., similar fibre-like structures are formed independent of the chirality of the amino acid. The random, efficient complexation of the PTA anions with lysine molecules is thus not a stereochemically driven reaction but presumably due to strong electrostatic interaction. Representative SEM pictures recorded from drop-coated films of this UV-irradiated lysine-PTA solution on a Si (111) wafer are shown in Figure 4.6C and

D at different magnifications. Comparison of the low magnification images recorded before (Figure 4.6A) and after UV-irradiation (Figure 4.6C) indicates that there are no significant changes in the fibre-like structures after UV-irradiation. This is an important result since any perturbation to the fibre-like morphology of the lysine-PTA colloidal particles would be detrimental to their application in the generation of linearly assembled metal nanoparticle superstructures.

Representative SEM pictures recorded from drop-coated films on a Si (111) wafer of the lysine-PTA colloidal particles after UV-irradiation and reaction with $AuCl_4^-$ ions are shown in Figure 4.7A and B. Comparison of the low magnification images recorded before (Figure 4.6A and C) and after reaction of lysine-PTA with gold ions (Figure 4.7A and B) indicates that there is no disturbance to the fibre-like structure of the lysine-PTA colloidal particles after nanogold formation.

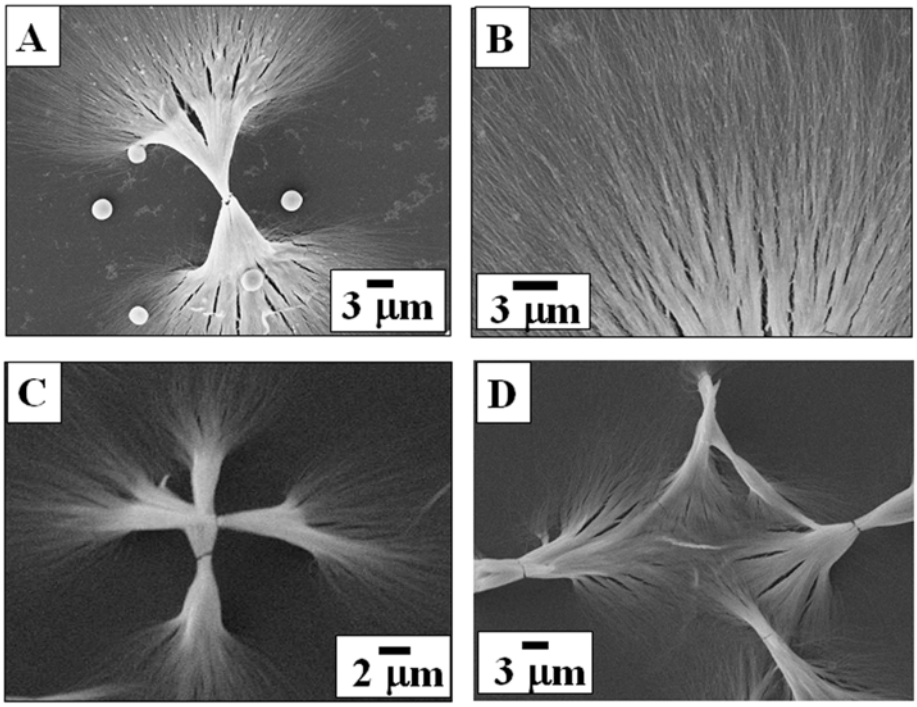

Figure 4.7: *(A) and (B) Representative SEM images of drop-cast films on a Si(111) substrate of gold nanoparticles synthesized by reaction of UV-irradiated lysine-PTA solution with aqueous 10^{-4} M $HAuCl_4$. (C) and (D): Representative SEM images of drop-cast films of the lysine-PTA solution on a Si (111) substrate after sonication and heat treatment (boiling).*

However at the resolution of the SEM images, the gold nanoparticles could not be discerned. From the SEM micrographs it is clear that the Keggin–lysine colloidal particles form fibre-like structures. These structures may be single colloidal particles or flocculates of smaller particles that have self-assembled into quasi-linear structures. In order to differentiate between these two possibilities, two control experiments were performed where the Keggin-lysine colloidal solutions were sonicated and boiled for half an hour separately. Figure 4.7C-D shows representative SEM images recorded at different magnifications from drop-coated films of the PTA-lysine colloidal solution after sonication and boiling on a Si (111) substrate respectively. Densely populated bundles of the lysine-PTA complex are seen on the surface of the substrate in both the cases (after sonication and boiling). The structures exhibit well-defined morphology that is predominantly fibre-like and very similar to the structures obtained from the as-prepared particles (Figure 4.6A and B) prior to heat/sonication treatment. Comparing the SEM images (Figures 4.7C, D and 4.6A, B), it is clear that the fibre-like structures are individual colloidal particles present in the solution and not due to flocculates. As would be expected of such single colloidal particles, they are sufficiently robust and resist breaking up during heat/ultrasound treatment.

4.2.7 X-Ray diffraction (XRD) measurements

The X-ray diffraction pattern recorded from this drop-coated film of the lysine-PTA complex solution on a glass substrate is shown as curve 2 in Figure 4.8. A number of sharp Bragg reflections are observed that are characteristic of the Keggin structure [39, 40]. For comparison, the XRD pattern recorded from pure PTA is shown in Figure 4.8 (curve 1). Comparing the two curves (curves 1 and 2) it is observed that along with the Keggin peaks, some extra peaks appear (indicated by "*"). These extra peaks might be due to lysine molecules present in the lysine-PTA complex. The X-ray diffraction pattern recorded from a drop-coated film of the gold nanoparticle solution synthesized by reduction of gold ions by UV-irradiated lysine-PTA complex solution is shown in the inset of the Figure 4.8. The Bragg reflections characteristic of fcc gold are identified in this XRD pattern clearly indicating that the gold particles are crystalline.

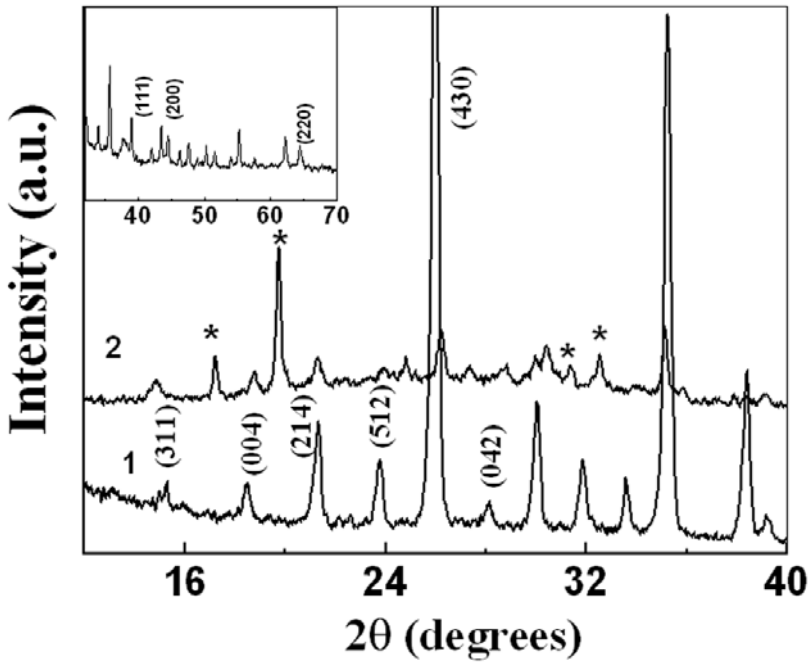

Figure 4.8: *XRD patterns recorded from drop-coated films on glass substrates of pure phosphotungstic acid solution (curve 1) and lysine-PTA solution (curve 2). The inset shows the XRD pattern recorded from gold nanoparticles synthesized by reaction of UV-irradiated lysine-PTA solution with aqueous $HAuCl_4$.*

Characteristic Bragg reflections from the Keggin ions are also observed indicating that UV-activation and reduction of $AuCl_4^-$ ions has not disturbed their basic structure.

4.2.8 Transmission Electron Microscopy (TEM) measurements

The transmission electron microscopy (TEM) images recorded from the lysine-PTA particles are shown in Figure 4.9A and B and clearly show bundles of loosely aggregated nanofibres with lengths in the range 100-150 μm and a high uniformity in structure. TEM images of the nanofibres at a higher magnification are shown in Figure 4.9C. At higher magnification, it is seen that the individual fibres are extremely uniform both in size and shape. The widths of the fibres was estimated from the high magnification TEM images to be in the range ~40-50 nm and have a smooth surface. Figure 4.9D-F show representative TEM images recorded at different magnifications from a drop-coated film of the gold nanoparticle solution synthesized by reaction of $HAuCl_4$ solution with the UV-irradiated lysine-PTA solution on a carbon coated copper

TEM grid. From the low magnification TEM image (Figure 4.9D) it is clearly seen that the fibre-like structures with negligible change in the overall morphology are retained even after formation of the gold nanoparticles.

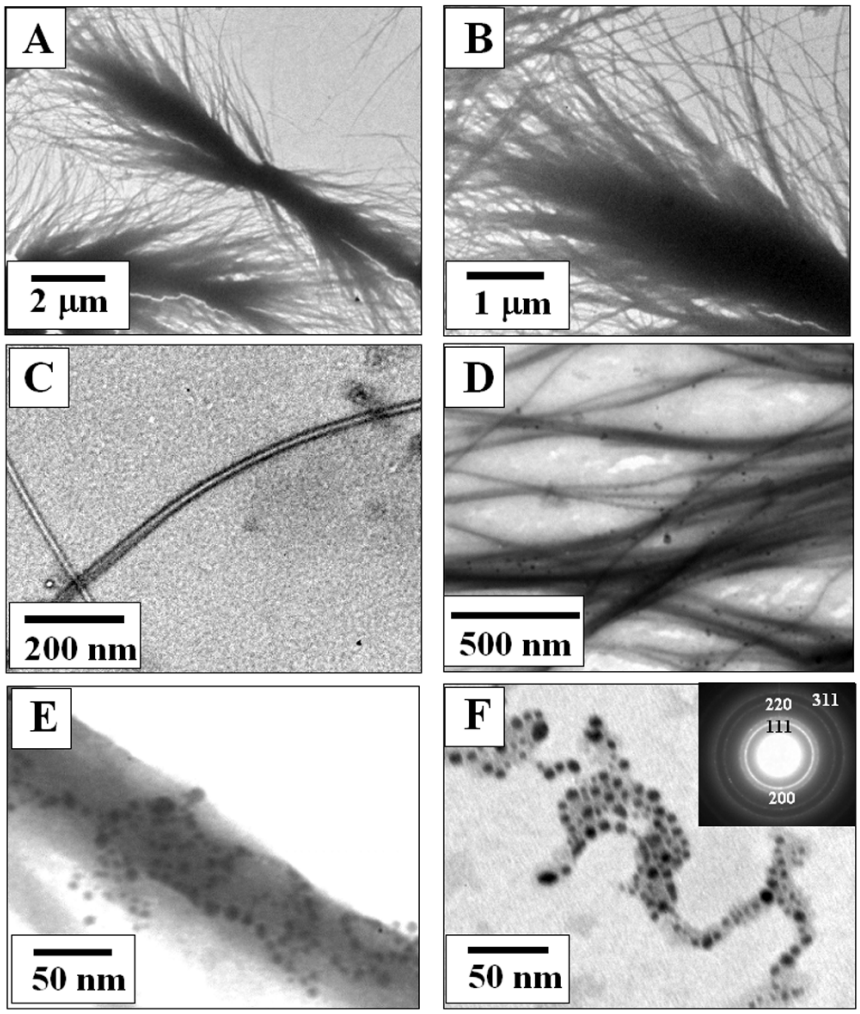

Figure 4.9: *(A)–(C) Representative TEM micrographs recorded at different magnifications from drop-cast films of the lysine-PTA solution on carbon-coated copper TEM grid. (D)-(F) Representative TEM micrographs recorded at different magnifications from drop-cast films of gold nanoparticles synthesized by the reaction of UV-irradiated lysine-PTA solution with aqueous 10^{-4} M $HAuCl_4$. The inset in F shows the selected area electron diffraction pattern recorded from the gold nanoparticles on the fibre-like lysine-PTA colloidal templates shown in the main part of the figure.*

Furthermore, the gold nanoparticles are observed only on the surface of the fibres indicating that the gold ion reduction has occurred on the surface of the lysine-PTA colloidal particles and therefore, act as excellent templates. At higher magnification

(Figure 4.9E and F) the individual gold nanoparticles attached to the underlying lysine-PTA fibres are seen in much greater clarity and detail. The gold nanoparticles range in size from 7 - 9 nm in diameter and are aligned along the axis of the fibres. The inset of the Figure 4.9F shows the selected area electron diffraction (SAED) pattern recorded from the gold nanoparticles on the lysine-PTA fibres of Figure 4.9C. The diffraction rings have been indexed in the figure and are clearly due to the face centered cubic (fcc) gold unit cell structure. It is interesting to note that there is very little spillover of the gold nanoparticles outside the fibre-like templates of lysine-PTA complex indicating the high degree of fidelity to the lysine-PTA template.

4.2.9 Summary

The formation of fibre-like colloidal particles of phosphotungstate Keggin ions complexed with lysine amino acid has been demonstrated. Lysine-PTA colloidal particles are excellent templates for the synthesis of organized assemblies of metal nanoparticles wherein the Keggin ion in the lysine-PTA host plays the role of a UV-switchable reducing agent. More specifically, we investigated the formation of aqueous colloidal particles of lysine amino acid complexed with phosphotungstate $(PW_{12}O_{40})^{3-}$ Keggin ions and showed that they may be used as a new class of organic-inorganic scaffolds in the synthesis of metal nanoparticle assemblies. The crystalline Keggin ion host reduced photochemically resulted in facile electron transfer to the gold ions and consequent formation of gold nanoparticle assemblies on the underlying fibre-like colloidal particle surface.

4.3 A comparative study of the binding of Keggin ions to amino acids

In spite of its well-demonstrated ability to study the thermodynamics of chemical reactions, ITC has remained relatively under-exploited in inorganic chemistry and in materials synthesis. As a first step towards addressing this lacuna, we have recently shown that ITC is an excellent technique to study the binding of amino acids with gold nanoparticles [59]. We extend our studies into the use of ITC in materials synthesis and present details of our investigation into the nature of interaction of different amino acids with phosphotungstate (PTA) Keggin anions. In a typical experiment, 20 ml of 10^{-3} M

aqueous solution of phosphotungstic acid was mixed in a test tube along with 20 ml each of 10^{-3} M aqueous solutions of the amino acids lysine, tryptophan, aspartic acid and glutamic acid and allowed to react for 3 hours. Samples for scanning electron microscopy (SEM) were prepared by drop-coating the amino acid-PTA solutions onto Si (111) wafers and allowing the aqueous component to dry. SEM measurements were carried out on a Leica Stereoscan-440 scanning electron microscope. Isothermal titration calorimetric (ITC) measurements were carried out to characterize the interaction between PTA and the various amino acids in a Micro Cal VP-ITC instrument at 298 K. The calorimeter consists of two cells: a reference cell filled with pure solvent (water) and a sample titration cell filled with 1.47 ml of 10^{-3} M aqueous phosphotungstic acid (PTA) solution. 4 x 10^{-2} M aqueous solution of each of the amino acids was added from the syringe into the titration cell containing the PTA solution in small steps of 10μL. The heat evolved/absorbed during reaction of the different amino acid with PTA anions was measured, the time between successive injections of aqueous solution of amino acids being 2 min. In order to correct for calorimetric response arising from dilution of the amino acids in water, control experiments were performed wherein 4 x 10^{-2} M aqueous solutions of the 4 amino acids were titrated against deionized water at pH 3 (pH of the PTA solution in the amino acid-PTA binding experiments), pH adjusted using acetic acid. The calorimetric response in these dilution experiments were then subtracted from the ITC data obtained during titration of the corresponding amino acids with PTA solution. This corrected data was subjected to analysis to extract the relevant thermodynamic parameters.

4.3.1 Complexation with L-Lysine

Figure 4.10A shows plots of the Isothermal Titration Calorimetric measurements of the binding of Keggin ion with L-lysine while Figure 4.10B and C show representative SEM images recorded at different magnifications from a drop-coated film of colloidal particles formed by the reaction of aqueous solution of PTA and L-lysine deposited onto a Si (111) substrate. Densely populated bundles of the highly linear lysine-PTA complexes are seen on the surface of the substrate (Figure 4.10B), very much in agreement with our previous results. In order to follow the real-time complexation of L-

lysine with the Keggin ions, we carried out ITC measurements where 10 µl of lysine ($4x10^{-2}$ M) from a syringe was injected into 1.47 ml of PTA solution (10^{-3} M) taken in a sample cell. The upper frame of Figure 4.10A shows the raw data obtained in the ITC experiment and shows clearly a strong exothermic reaction, where each peak in the figure is the result of a single injection.

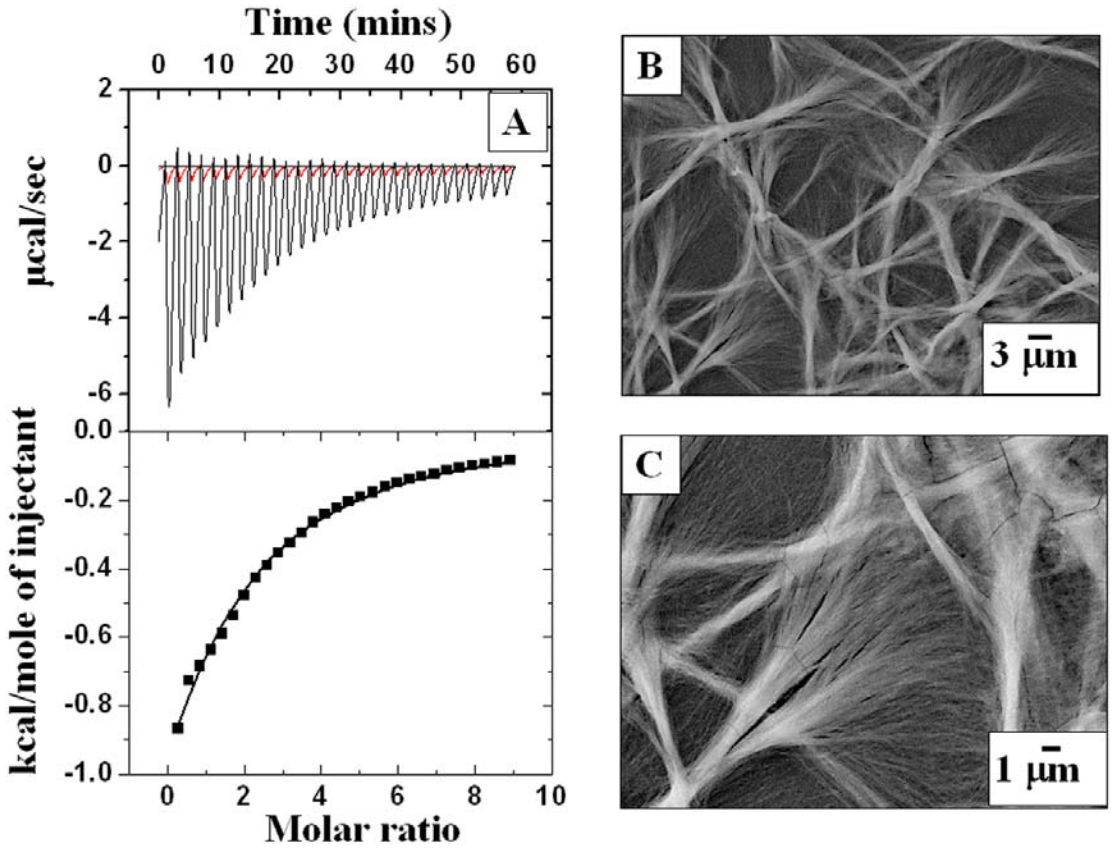

Figure 4.10: *(A) Isothermal titration calorimetric data recorded during successive injections of 10 µl aqueous L-lysine solution into the titration cell containing 1.47 ml of aqueous phosphotungstic acid solution. The data in red corresponds to the ITC response recorded during titration of L-lysine against deionized water with pH adjusted to 3 using acetic acid. The lower frame shows the binding isotherm obtained by integration of the raw data shown in the upper panel after conversion to molar ratio of the reacting lysine and PTA in the titration cell (text for details). The solid line is based on a 1-site binding model for the lysine-PTA reacting species. B and C. Representative SEM images of drop-cast films of L-lysine-PTA solution on a Si (111) substrate at different magnifications.*

Please note that the data shown here (and in all subsequent measurements) has been corrected for effects arising due to dilution of the amino acid during titration (data in red). It is well known that the calorimetric response during dilution of the injectant can be quite prominent and capable of obscuring the calorimetric response during reaction and must be carefully taken into account. Consequently, the calorimetric dilution response of the various amino acids (data shown in red in all the raw ITC data) has been subtracted from the ITC raw data recorded during reaction of the different amino acids with Keggin ions before extraction of thermodynamic parameters. During initial stages of reaction, a large number of amino acid molecules and Keggin ions are free and available for reaction, and hence the exothermicity is very large (Figure 4.10A). As the free reacting species are depleted, the exothermicity decreases progressively and reaches saturation (after roughly 25 injections). Integration of the heat exchanged over each injection cycle gives rise to the curve shown in the lower frame of Figure 4.10A, and is commonly referred to as the 'binding isotherm'. The binding isotherm clearly shows when the reaction is completed and also enables extraction of relevant thermodynamic parameters associated with the reaction. The binding isotherm data in Figure 4.10A has been analyzed using Origin (***Microcal***) software (solid line fit to the data) and fitted using a single-site binding model whereby a single set of enthalpy and entropy values has been obtained.

Since the isoelectric point (pI) of lysine is 9.74 and the pH of PTA solution used in all the ITC studies ranges between 2.7-3.0, it is obvious that at this pH lysine would be fully protonated. The expected strong electrostatic interaction of the cationic lysine molecules with PTA anions is clearly mirrored in the strong exothermicity of this reaction. The reaction primarily driven by enthalpy changes shows variations in morphology as is shown in Figure 4.10B and C. Nevertheless as was discussed in an earlier note, these structures are resistant to any sort of heat treatment.

4.3.2 Complexation with L-Tryptophan

Given the fact that tryptophan (amino acid having an indole group as the side chain) possesses one amine group as opposed to two in lysine and that the pI of tryptophan is 5.89, it would be expected that this amino acid would bind less strongly with Keggin ions. The

ITC data recorded during reaction of tryptophan with Keggin ions (accounting for amino acid dilution, data in red) is shown in Figure 4.11A. Comparing the raw ITC data recorded from lysine and tryptophan (Figure 4.10A and 4.11A respectively), we observe that the degree of exothermicity during the initial stages of reaction is conspicuously lower in case of tryptophan than that in lysine.

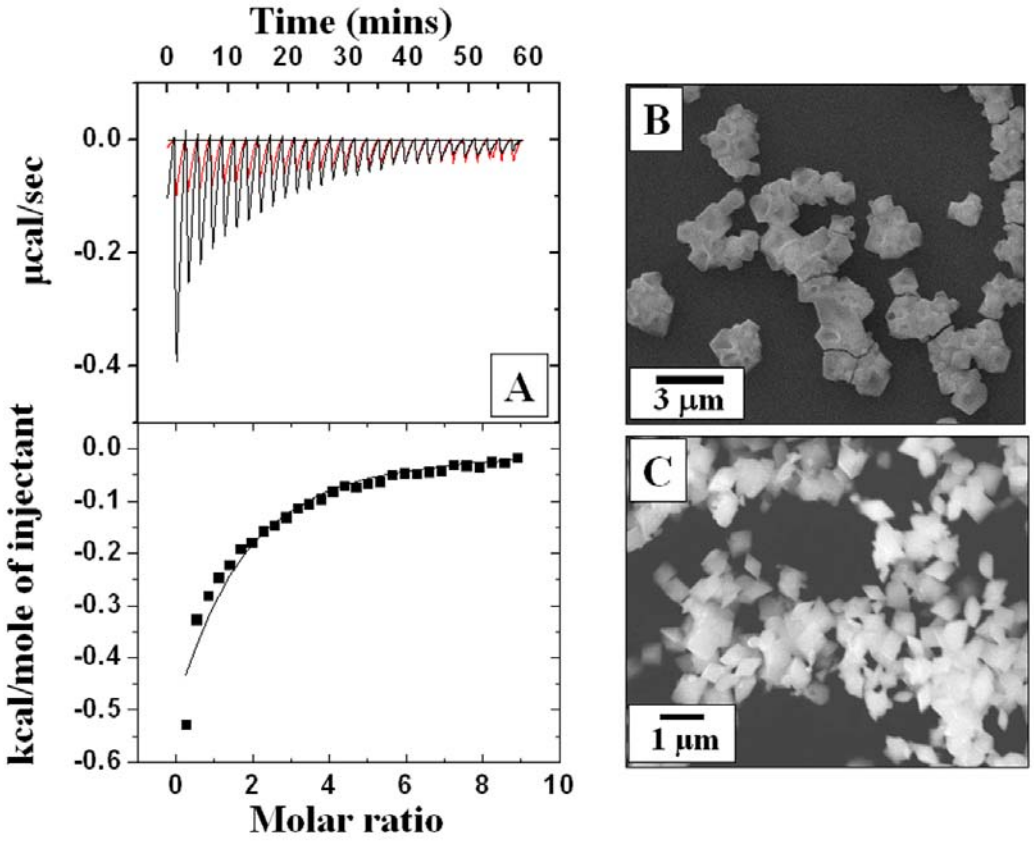

Figure 4.11: *(A) Isothermal titration calorimetric data recorded during successive injections of 10 µl aqueous L-tryptophan solution into the titration cell containing 1.47 ml of aqueous phosphotungstic acid solution. The data in red corresponds to the ITC response recorded during titration of L-tryptophan against deionized water with pH adjusted to 3 using acetic acid. The lower frame shows the binding isotherm obtained by integration of the raw data shown in the upper panel after conversion to molar ratio of the reacting L-tryptophan and PTA in the titration cell (text for details). The solid line is based on a single-site binding model for the L-tryptophan-PTA reacting species. B and C. Representative SEM images of drop-cast films of L-tryptophan-PTA solution on a Si (111) substrate at different magnifications.*

The tryptophan-PTA ITC binding isotherm data has been fitted using a single-site binding model (solid line shown in the lower frame of Figure 4.11A). It is seen that in this case, the reaction is entropically driven and in this sense, is different from the Keggin ion interaction observed for lysine. Representative SEM image recorded from the colloidal particles formed by the reaction of tryptophan with PTA is shown in Figure 4.11B. The morphology of the particles is considerably different from that obtained with lysine. At higher magnification (data not shown) the tryptophan-PTA colloidal particles are seen to vary in size from 300 to 500 nm and appear to possess a rhombic structure, considerably different from the whisker-like linear colloidal structures obtained by the reaction of lysine with PTA (Figure 4.10B).

4.3.3 Complexation with L-Aspartic acid and L-Glutamic acid

It is interesting that different amino acids after complexation with the same PTA anions result in a dramatic difference in the morphology of the colloidal particles formed in the biorgano-inorganic reaction. Clearly, stereochemical considerations dominate over simple electrostatic considerations in directing the morphology of the colloidal particles formed in such reactions with important implications in the use of such colloidal particles as scaffolds in nanomaterials synthesis [60]. In order to probe these effects further, we have studied the interaction of the acidic amino acids aspartic acid (pI ~ 2.77) and glutamic acid (pI ~ 3.22) with Keggin ions. At the pH of reaction of the amino acids with Keggin ions (pH 2.5-3), aspartic acid and glutamic acid would be zwitterionic and hence would be predicted to have little affinity for the Keggin anions. Figure 4.12A and B show the ITC calorimetric response of aspartic acid and glutamic acid during reaction with PTA solution respectively (upper panels). Unlike in the case of lysine and tryptophan that are charged positively at pH 3, these acidic amino acids exhibit an endothermic response during reaction with the Keggin ions. Indeed, the calorimetric response recorded during dilution is also endothermic in nature (data in red in the upper panels of Figure 4.12A and B) indicating considerable perturbation to the water structure during dissolution of these amino acids in water. That the calorimetric response is different in the dilution experiment and experiment related to reaction of the acidic amino acids with PTA indicates that there is some interaction of the amino acids with PTA anions. The lower panels in Figure 4.12A

and B show the binding isotherms obtained by integration of the raw data for the corresponding amino acids together with a fit to the data based on a single-site binding model. While the fit is good for the aspartic acid-PTA binding isotherm (lower panel, Figure 4.12A), the fit is poor for the glutamic acid-PTA reaction (lower panel, Figure 4.12B).

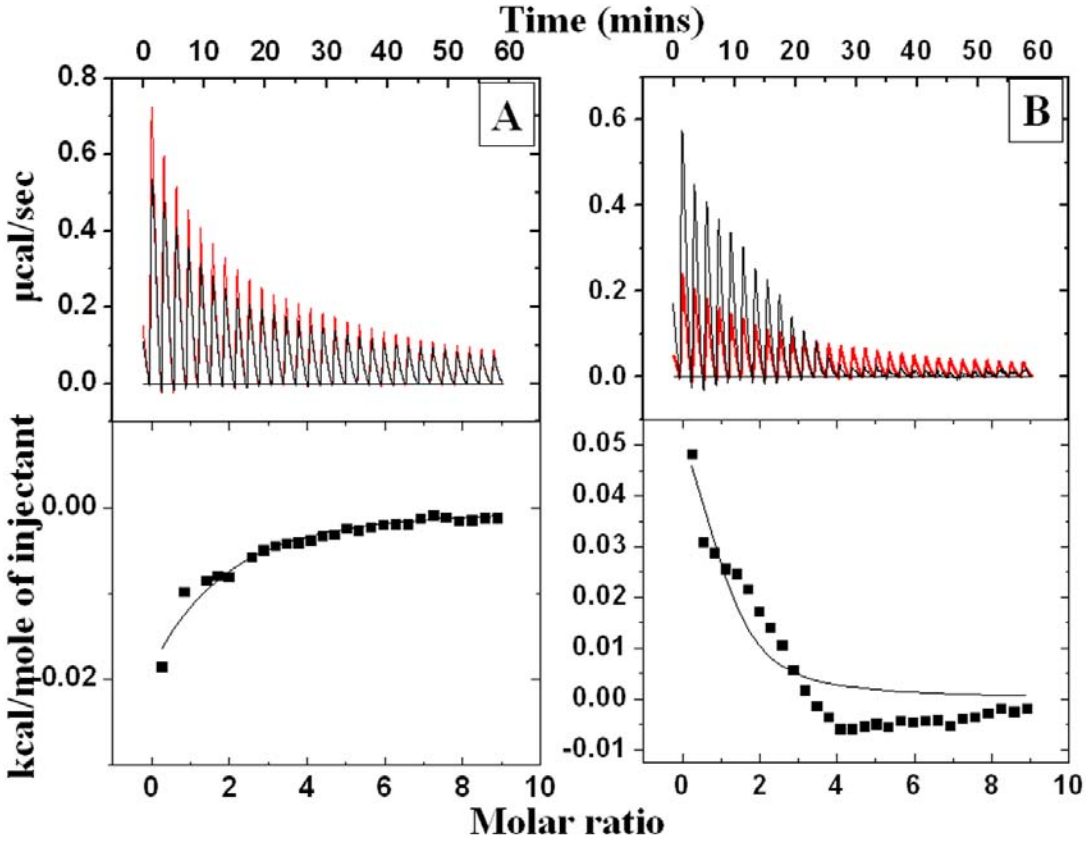

Figure 4.12: *Isothermal titration calorimetric data recorded during successive injections of (A) 10 µl aqueous aspartic acid solution and (B) 10 µl aqueous glutamic acid solution into the titration cell containing 1.47 ml of aqueous phosphotungstic acid solution showing considerable endothermicity. The data in red in (A) and (B) corresponds to the ITC response recorded during titration of L-aspartic acid and L-glutamic acid respectively against deionized water with pH adjusted to 3 using acetic acid. The lower frame shows the binding isotherm obtained by integration of the raw data shown in the upper panel.*

In both cases, the interaction of the amino acid with Keggin ions is entropically driven. In the case of glutamic acid reaction with Keggin ions, the model adopted to describe the

reaction needs refinement. At this stage, it is not clear whether the single-site binding model is inadequate or whether there are hierarchical binding events that occur in this reaction. Representative SEM images recorded from drop-coated films of PTA-aspartic acid and PTA-glutamic acid on Si (111) substrates are shown in Figure 4.13A and B respectively. In the case of aspartic acid-Keggin ion colloidal particles (Figure 4.13A), they seem to consist of different shapes of particles, a closer look into the structures reveals that in some places there are clusters, which grossly resemble that of the tryptophan-PTA structures. Interestingly, the morphology of the colloidal particles obtained by reaction of glutamic acid with Keggin ions is quite different exhibiting a quasi-spherical morphology (Figure 4.13B). The SEM studies thus clearly underline the fact that electrostatic interactions appear to be directing the morphology of the colloidal particles formed in the reactions between amino acids and Keggin ions.

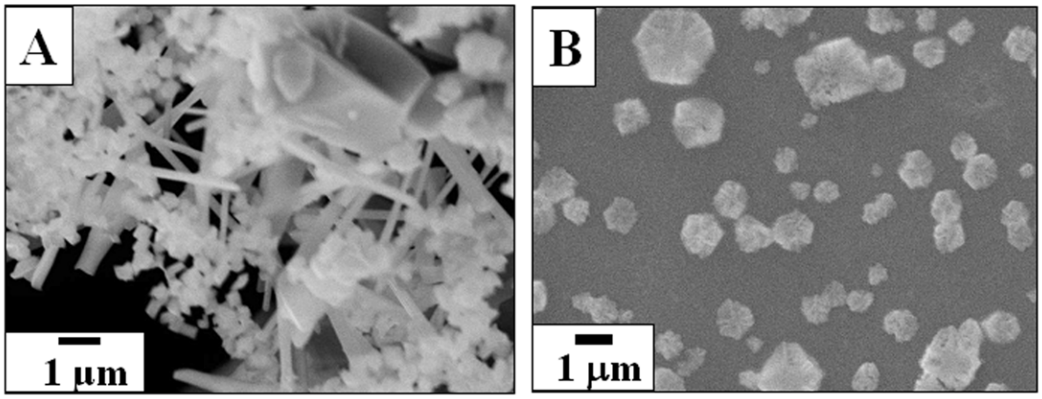

Figure 4.13: *(A) and (B) Representative SEM images of drop-cast films of the amino acid aspartic acid-PTA solution and glutamic acid-PTA solution on Si (111) substrates respectively.*

4.3.4 Summary

The binding of Keggin ions with four different amino acids has been demonstrated. While there is marked binding affinity with lysine and tryptophan, aspartic acid and glutamic acid show disinclination towards binding with Keggin ions. It has been possible to form nanofibres like superstructures with lysine, having an extremely exothermic binding nature, which are very stable and have potential application to serve as versatile nanoreactors for the template mediated synthesis of nanoparticles. However we caution that there exists no correlation in the morphology observed in the complexes

formed with different type of amino acids. Understanding of the thermodynamic parameters that control the binding of any two interacting species has opened up the great prospect of tailored growth of inorganic-organic hybrid superstructures.

4.4 Anisotropic gold nanotriangles using phosphomolybdate-lysine hybrid nanostructures

4.4.1 Synthesis of gold nanotriangles

In a typical experiment, 20 ml of 10^{-3} M aqueous solution of phosphomolybdic acid [PMA, $H_3(PMo_{12}O_{40})$] obtained from Aldrich as a solid powder and used as-received was mixed in a test tube along with 20 ml of 10^{-3} M aqueous solution of lysine amino acid (L-lysine) and was kept for 2 hours as shown in the scheme of Figure 4.14.

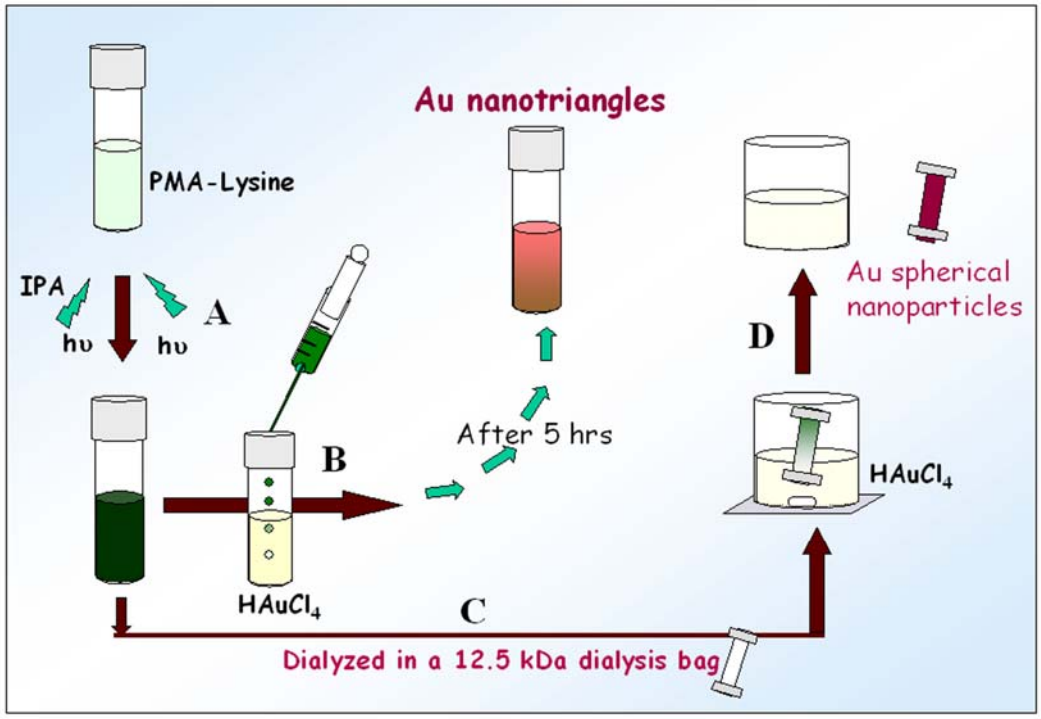

Figure 4.14: *Scheme showing the formation of Au nanotriangles in steps (A)-(B): Step (A) PMA-Lysine solution irradiated for 3 hrs. Step (B) 5ml of irradiated PMA-Lysine (dark green) solution injected into 5 ml of $HAuCl_4$ and kept for 5-6 hrs resulting in the formation of Au nanotriangles. In a control experiment irradiated PMA-Lysine was kept in a 12.5 kDa dialysis bag and stirred in a beaker containing 200 ml of $HAuCl_4$ (Step C). Step (D) Aliquot taken out from the dialysis bag and checked for spectral characterization.*

To 30 ml deaerated (nitrogen bubbled for 10 mins) aqueous solution of L-lysine and phosphomolybdic acid, 2 ml of propan-2-ol was added and the mixture irradiated by UV light for 3 h (pyrex filter, > 280 nm, 450 W Hanovia medium pressure lamp). This led to reduction of $(PMo_{12}O_{40})^{3-}$ ions present in the lysine-phosphomolybdate (lysine-PMA) complex and is seen as a dark green color appearing in the solution shown in the pictorial representation of Figure 4.14. To 5 ml of 10^{-3} M $HAuCl_4$ solution, 5 ml of this irradiated L-lysine-PMA solution was added and then was immediately characterized by UV-Vis-NIR spectroscopy measurements. The solution changed color gradually from yellow to colourless and then to red with a brown tinge indicating formation of gold nanoparticles and was monitored by UV-Vis-NIR spectra kinetics. Samples for transmission electron microscopy (TEM) analysis were prepared by drop-coating films of the lysine-PMA solution at different stages of reaction on carbon-coated copper TEM grids, allowing the grid to stand for 2 min following which the extra solution was removed using a blotting paper. Samples of the gold nanotriangles formed were cast onto Si (111) substrate and analyzed by Atomic force microscope (AFM).

4.4.1.1 UV-Vis-NIR spectroscopy measurements

Figure 4.15 shows the UV-Vis spectra recorded from the mixtures of 10^{-3} M PMA and 10^{-3} M L-Lysine at different stages of treatment. Prior to UV-irradiation, it is observed that the mixture shows no absorbance in the visible region of the electromagnetic spectrum (curve 1, Figure 4.15). This is corroborated with the test-tube image marked ‘a’ in the inset of Figure 4.15 which shows the solution to be transparent and colourless. The UV-vis absorption spectrum recorded after UV-irradiation of the aqueous solution of lysine-PMA complex for 3 h is shown as curve 2 in Figure 4.15 (also Step A in Figure 4.14). The UV-Vis spectrum shows absorption at around 700 nm with shoulders at 900 and 1000 nm, which is characteristic of multiple electron transfer [61] in PMA. The strong absorption in the visible region of the reduced PMA is seen as dazzling intense green color of the solution marked as ‘b’ in the inset of Figure 4.15. The color of the solution persists for more than a week showing the incapability of PMA to undergo easy aerial oxidation as opposed to reduced PTA (phosphotungstic acid) whose color (dark blue) fades within 4-5 hrs after it has been reduced. The mixture of PMA and L-

lysine after irradiation (5 ml) thereafter was added to 10^{-3} M $HAuCl_4$ (5 ml) and the UV-Vis spectra was recorded at different time intervals (Step B in Figure 4.14).

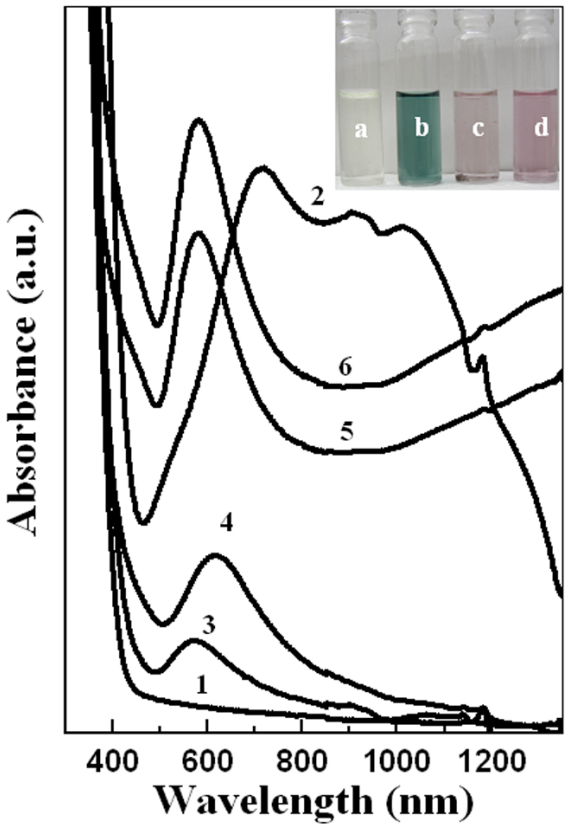

Figure 4.15: *UV-Vis-NIR spectra recorded from: curve 1– aqueous mixture of10^{-3} M phosphomolybdic acid and 10^{-3} M amino acid lysine solutions before UV irradiation; Curve 2- After UV-irradiation of the lysine-PMA solution for 3 h; Curves 3-6- Direct addition of aqueous solution of 10^{-3} M $HAuCl_4$ into the UV-irradiated lysine-PMA solution at different time intervals (immediate addition, after 2 h, 6h and 9h respectively).*

Curve 3 in Figure 4.15 shows the UV-Vis spectra recorded immediately after addition of aqueous solution of 10^{-3} M $HAuCl_4$ to the mixture of irradiated L-Lysine and PMA. It is observed that a fairly sharp absorption band appears centered around 569 nm. This absorption band is characteristic of gold nanoparticles and arises due to the excitation of surface plasmon vibrations in gold nanoparticles [1]. The apparent shift in the plasmon band might be due to the formation of clusters of gold nanoparticles.

Curve 4 in Figure 4.15 shows the UV-Vis spectra recorded from the same solution after 2 hrs of reaction. There appears to have been no significant change in the absorption

spectrum as compared to the zero time. solution (Curve 3 Figure 4.15) except that the absorption peak has still been red shifted to around 610 nm. This is shown by the test-tube marked 'c' in the inset of Figure 4.15. After 6 hrs of reaction in addition to the absorption peak centered around 600 nm there is a concomitant increase of the absorption band in the NIR region (Curve 5 in Figure 4.15). The appearance of a component in the higher wavelength region in the UV-Vis-NIR spectrum attribute to a considerable amount of anisotropy present in the gold nanoparticles. After 9 hrs of reaction there is no change in the absorption spectra of the reduced gold nanoparticles (Curve 6 in Figure 4.15) except that the intensity of absorption is increased.

4.4.1.2 Transmission Electron Microscopy (TEM) measurements

Figure 4.16A and B show representative TEM images recorded immediately after addition of 5 ml of $HAuCl_4$ to the aqueous solution containing 5 ml of reduced PMA-Lysine. It is clearly seen from the TEM image (Figure 4.16A) that there is a reasonable number of spherical gold nanoparticles. Taking a closer look into the morphology of the gold nanoparticles at higher magnifications (Figure 4.16B and inset of Figure 4.16A) it appears that some of the regions of the carbon-coated copper grid seem to consist of clusters of gold nanoparticles that are loosely associated. This could be one of the possible reasons for the apparent shift of the plasmon absorption peak at around 570 nm (curve 3 Figure 4.15A). As already seen, that the UV-Vis spectra after 2 hrs of reaction was further red-shifted to 610 nm and is corroborated by their corresponding TEM images which showed that increased amount of clustering might be the plausible reason for the shift as is shown in Figure 4.16C and D. The low magnification TEM image (Figure 4.16E) shows the appearance of truncated gold nanotriangles in addition to a small number of spherical particles. The inset of Figure 4.16E shows the selected area electron diffraction pattern recorded from one of the triangles shown in Figure 4.16F and have been indexed with reference to the fcc unit cell structure of gold.

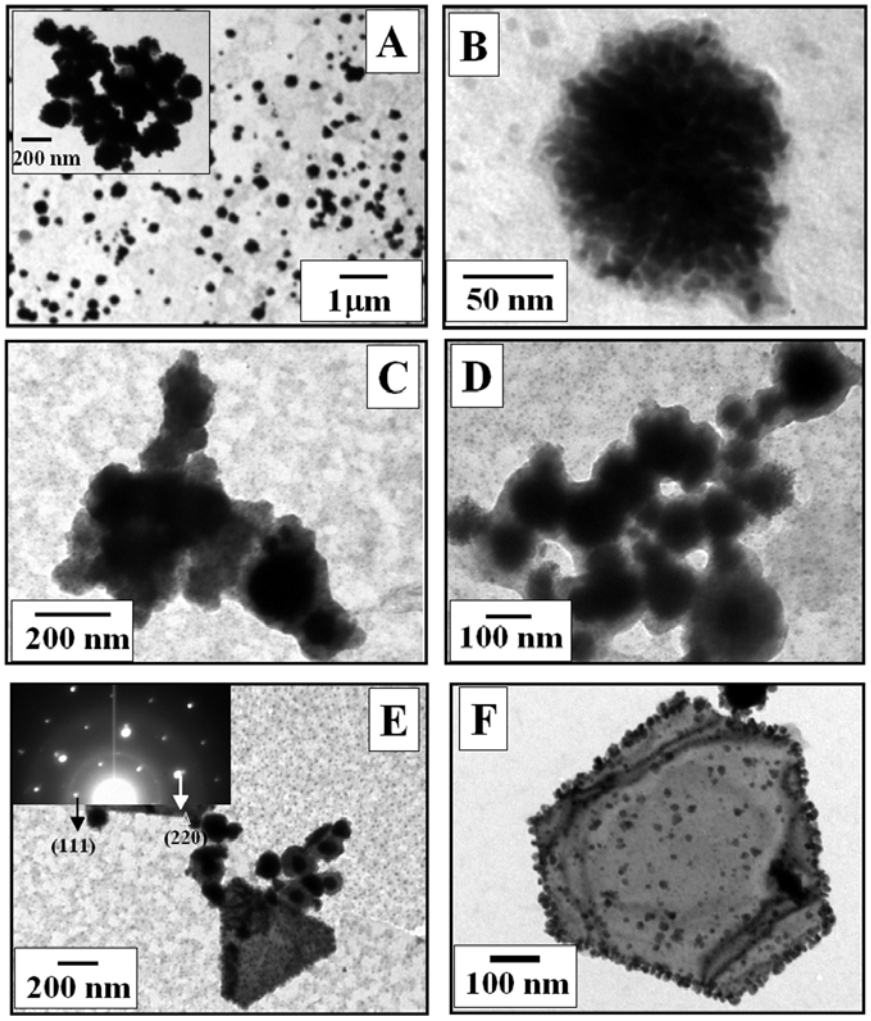

Figure 4.16: *Representative TEM micrographs at different magnifications from drop-cast films of the irradiated PMA-lysine solution added to 10^{-3} M $HAuCl_4$ aqueous solution recorded after immediate addition (A and B), 2 hrs (C and D) and 6 hrs (E and F) respectively. The inset in A shows clustering of gold nanoparticles whereas that in E shows the selected area diffraction pattern (SAED) recorded from one of the triangles shown in Figure F*

It can be easily visualized from the high magnified image of Figure 4.16F that a reasonable number of spherical gold nanoparticles have come together to make space for the formation of the truncated triangles. This is also evident from the fact that the edges of the triangle are rough and have not been properly formed.

Figure 4.17A-F shows representative TEM images of the same solution after 1 day of reaction. From the low (Figure 4.17A) and high magnification TEM image (Figure

4.17B) it is clearly seen that now there is a fair density of gold nanotriangles along with some hexagonal structures.

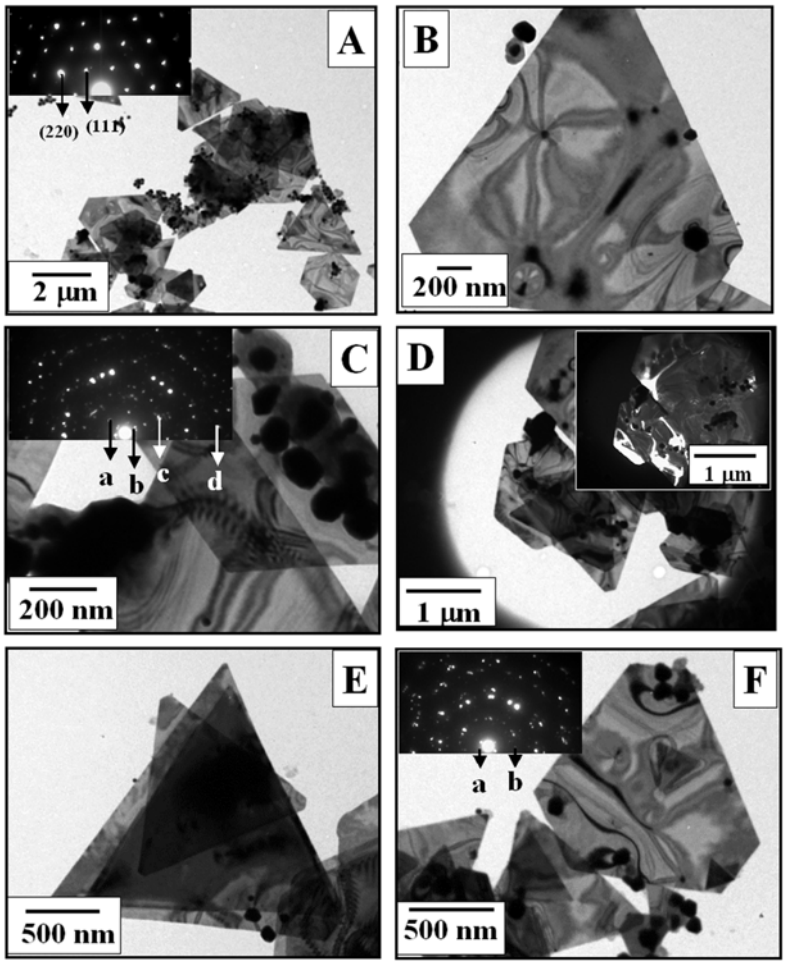

Figure 4.17: *Representative TEM micrographs at different magnifications from drop-cast films of the irradiated PMA-lysine solution added to 10^{-3} M $HAuCl_4$ aqueous solution recorded after 1 day of reaction (A-F). The inset in Figure A, C and F shows the selected area diffraction pattern (SAED) recorded from each of the triangles shown in the main figure respectively. The inner set of rings (marked with 'a' and 'b') in Figure 4.17C have been indexed with the unit cell structure of phosphomolybdic acid while that marked 'c' and 'd' in the same figure matches with that of fcc unit cell structure of gold. The inset in D shows the corresponding dark-filled image corresponding to (111) plane of the triangles as shown in the main Figure D. The letters 'a' and 'b' in the inset of Figure F corresponds to the d spacing of the fcc unit cell structure of gold.*

In contrast to the TEM image shown in Figure 4.16F in which the triangles have rough edges, the triangles here in Figure 4.17A possess a smooth growth front. That the

truncated triangles are extremely thin can be discerned from the high magnification TEM image (Figure 4.17B and C) which shows appearance of fringes typically known as 'Moiré fringes' occurring as a result of overlap of two such thin flat structures. Figure 4.17D and its corresponding inset show representative bright and dark-field TEM images corresponding to (111) plane respectively of the same triangles recorded from one of the sections of the carbon coated copper grid. Although with time (after 3 days) the triangles seem to grow in size (Figure 4.17E), yet the presence of some small triangles lying atop the bigger ones cannot be completely ruled out as is clearly visible from the TEM image of Figure 4.17F. The insets of Figure 4.17A, C and F show the selected area diffraction pattern recorded from one of the triangles as shown in their respective TEM images which have been carefully indexed. The inner set of rings shown in the diffraction pattern in the inset of Figure 4.17C (the inner rings corresponding to higher 'd' value, marked in black by 'a' and 'b') have been indexed with respect to the unit cell structure of pure PMA whereas those marked in white by 'c' and 'd' in the inset of Figure 4.17C corresponds to the fcc unit cell structure of gold.

4.4.1.3 X-Ray Diffraction Measurements (XRD)

The X-ray diffraction pattern recorded from a drop-coated film of the reduced $HAuCl_4$ aqueous solution by UV-irradiated PMA-Lysine complex solution on a glass substrate is shown in Figure 4.18. A number of sharp Bragg reflections are observed in the XRD pattern of Figure 4.18A that are characteristic of phosphomolybdic acid [62]. The peak marked as 'L' could be identified with that arising from L-Lysine. A sharp peak at $2\theta \sim 39^{o}$ is obtained in the XRD pattern shown in Figure 4.18A and B which corresponds to the (111) plane of the face-centered cubic gold nanoparticles.

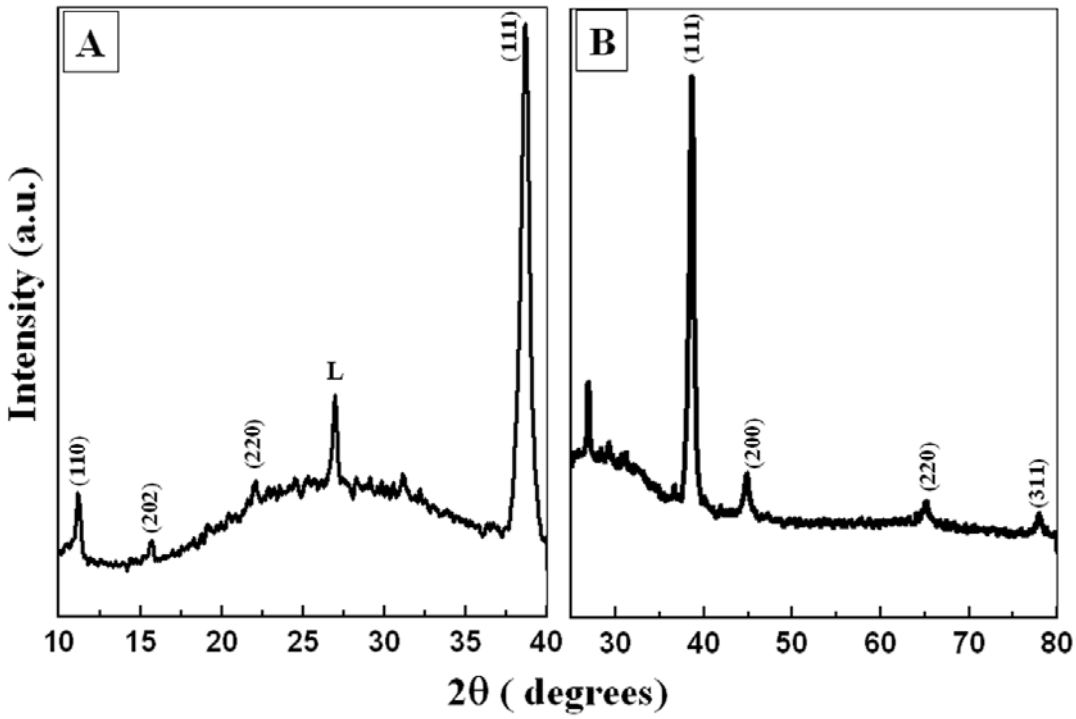

Figure 4.18: *A) and B) XRD patterns recorded from drop-coated films on glass substrates of the irradiated PMA-Lysine after addition to 10^{-3} M $HAuCl_4$ directly. The values given in parentheses are the (hkl) values arising from phosphomolybdic acid (A) and fcc unit cell structure of gold (B). The letter marked 'L' in A correspond to the (hkl) value arising from Lysine.*

4.4.1.4 Atomic Force Microscopy (AFM) measurements

A representative Atomic Force Microscopy (AFM) image of one of the gold nanotriangles obtained by reacting 5 ml of aqueous solution of 10^{-3} M $HAuCl_4$ to 5 ml of photo-irradiated PMA-lysine complex is shown in Figure 4.19. The surface profile is shown in Figure 4.19A and B which shows that the edge length is around 500 nm. The lines marked in blue and black in Figure 4.19B show the surface profile thickness to be 4.3 and 8.8 nm respectively taken from the triangle in Figure 4.19A. This indicates that the thickness of the triangle is not uniform and hence shows a high degree of anisotropy in the measured UV-Vis-NIR spectrum.

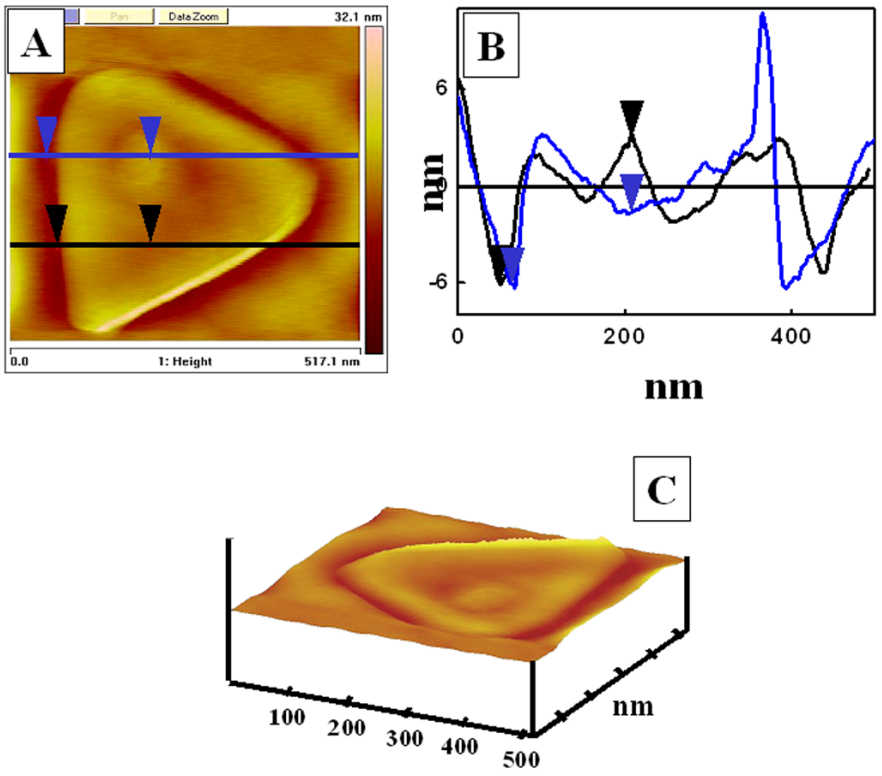

Figure 4.19: *AFM image of one gold nanotriangle showing the surface length profile (A and B) and the surface height (C). The black and blue lines marked in Fig. B show the different length profiles taken from different regions of the triangle in Fig. A*

4.4.2 Synthesis using a 12.5 kDa dialysis bag

In order to substantiate the role-played by L-Lysine in the synthesis of gold nanoparticles, a separate experiment was performed where the solution containing PMA-lysine after irradiation was kept inside a dialysis bag and then allowed to stir in a beaker containing 200 ml of aqueous solution of $HAuCl_4$. The solution inside the dialysis bag was kinetically monitored by UV-Vis spectroscopy measurements. After 24 hrs of reaction the solution kept outside the dialysis bag ($HAuCl_4$) was rotovapped and concentrated to form a powder. The powder was then mixed with KBr pellet and analyzed by Fourier Transform Infrared (FTIR) spectroscopy measurements and compared with that of pure $HAuCl_4$ and L-Lysine powders.

4.4.2.1 UV-Vis-NIR Spectra measurements

UV-Vis-NIR spectra of the aqueous solution containing photo-irradiated PMA-Lysine inside the dialysis bag was taken by taking minute aliquot of the solution at different time intervals. Figure 4.20 shows the kinetics of the UV-Vis-NIR spectra taken at different time intervals. Curve 1 in Figure 4.20 shows the UV-Vis-NIR spectra recorded from aqueous mixture containing 10^{-3} M PMA and 10^{-3} M Lysine. The solution mixture was UV irradiated for 3 hours, immediately clipped inside the dialysis bag and kept inside a beaker containing 200 ml of $HAuCl_4$ solution. The UV-Vis spectra of this irradiated solution was immediately taken which is shown as Curve 2 in Figure 4.20.

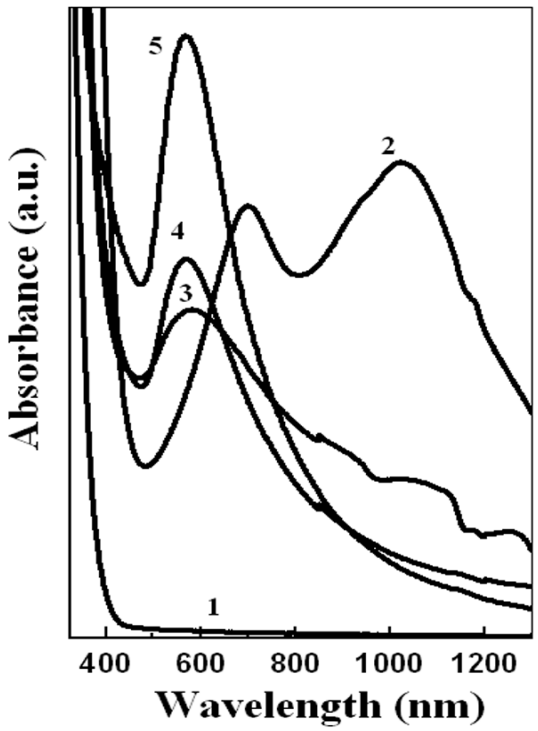

Figure 4.20: *Aliquots of irradiated PMA-Lysine kept in a 12.5 kDa cutoff dialysis and stirred in a beaker containing 200 ml of $HAuCl_4$ taken after 30 mins (curve 3), 5hrs (curve 4) and 1 day (curve 5) respectively. Curve 1 and 2 correspond to PMA-Lysine before and after irradiation respectively.*

The spectrum looks very much similar to that obtained after performing the reaction directly (Curve 2 Figure 4.15) that is characteristic of the photo-reduced state of PMA. After 30 minutes of reaction the solution-mixture was taken from inside the

dialysis bag and the spectra monitored. Curve 3 in Figure 4.20 shows the UV-Vis-NIR spectra recorded from this solution. There appears a peak centered around 570 nm, which is characteristic of the surface plasmon resonance of gold nanoparticles, with a complete damping of the absorption peak recorded for the photo-irradiated PMA-Lysine (Curve 2 Figure 4.20). This suggests that $HAuCl_4$ has gone through the dialysis membrane and have been reduced by irradiated PMA-Lysine. Further support to this can be obtained by recording the UV-Vis spectra of the solution outside the dialysis bag containing only $HAuCl_4$ that shows a progressive decrease in the absorption peak of $HAuCl_4$ centered around 300nm. Further aliquots at 5hrs and after 1 day taken from the solution inside the dialysis bag shows an UV-Vis-NIR absorption at exactly the same wavelength as obtained after 30 mins (Curves 3, 4 and 5 in Figure 4.20). The spectra recorded for the solution inside the dialysis bag (Curves 4 and 5 in Figure 4.20) appears very much different as recorded from the direct addition of irradiated PMA-Lysine to $HAuCl_4$ (Curves 5 and 6 in Figure 4.15), which shows no absorption in the NIR region.

4.4.2.2 Transmission Electron Microscopy (TEM) measurements

The fact that there has been no growth of anisotropy in the formed nanostructures as was shown by UV-Vis-NIR spectra was also confirmed from representative TEM images (Figure 4.21A and B) recorded even after 24 hrs, which shows no tendency for the formation of nanotriangles that is responsible for the longitudinal peak appearing in the NIR region. This marked difference in the shape selectivity might arise due to the leakage of Lysine which is a small molecule compared to the pore size diameter of the 12.5 kDa cutoff dialysis bag. PMA, which is a larger molecule (MW~1850), is trapped inside the dialysis bag and the reduced gold nanoparticles (TEM image of Figure 4.21D) along with that of larger clusters (TEM image of Figure 4.21C) is the result of mere reduction of $HAuCl_4$ by irradiated PMA.

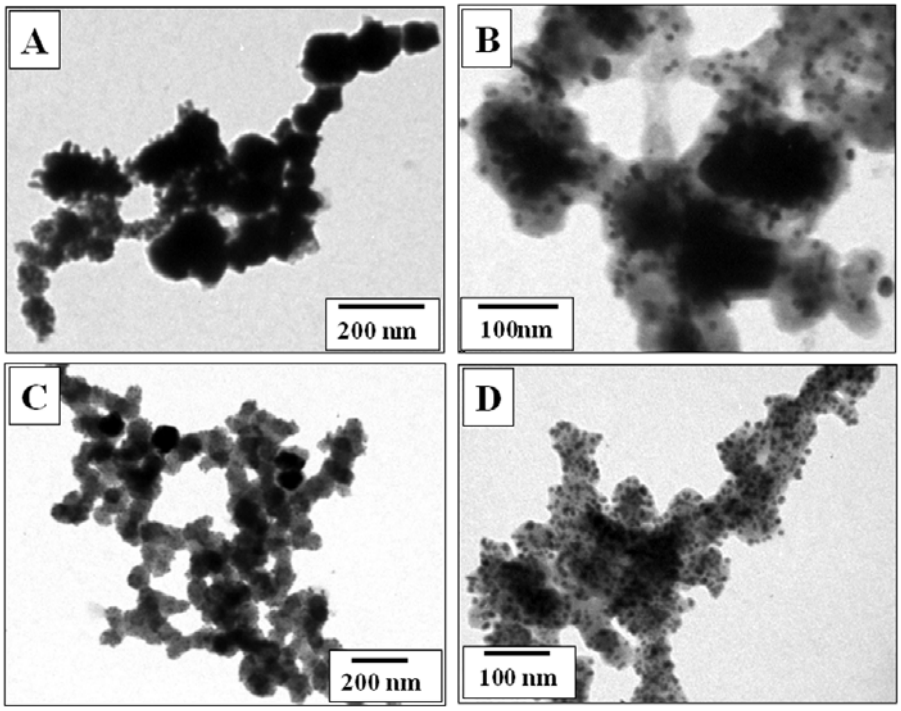

Figure 4.21: *A-D: Representative TEM images at different magnification taken from the aliquot after 1 day of reaction of the irradiated PMA-Lysine kept in a 12.5 kDa cutoff dialysis bag and stirred in a beaker containing 200 ml of $HAuCl_4$.*

4.4.2.3 Fourier Transform Infra-red (FTIR) Spectroscopy studies

An additional support to this supposition can be achieved by looking at the Fourier Transform Infrared (FTIR) spectra provided in Figure 4.22. The solution outside the dialysis bag after reaction for 24 hrs was taken and concentrated by rotovaping till it resulted into a yellowish powder. Fourier Transform Infrared (FTIR) spectroscopy measurements of the pure powders of $HAuCl_4$ and L-Lysine taken in KBr pellet are shown as Curves 1 and 2 in Figure 4.22 respectively. The spectrum has been separated into 2 windows in order to take into account the vibrational frequencies arising from different functional moieties. The FTIR spectra of pure Lysine (Curve 2 in Figure 4.22A) shows a batch of peaks in the region 600-1200 cm^{-1} which is classified as the finger-print region of the IR spectrum [63]. Such signatures are not observed in the FTIR spectra recorded from pure $HAuCl_4$ powder taken in a KBr pellet (Curve 1 in Figure 4.22A). After dialysis, it is believed that Lysine, a small molecule in size, which was bound to

PMA, separates out and goes into the solution which is evident from the FTIR spectra (Curve 3 in Figure 4.22) recorded from the rotovapped powder. Lysine outside the dialysis bag might electrostatically bind with $AuCl_4^-$ ions resulting in the shifted and broad nature of the FTIR bands in the finger print region (Curve 3 in Figure 4.22A) as compared to that of pure Lysine (Curve 2 in Figure 4.22A). Further support to this can be obtained by the diminished intensity of the highly characteristic NH_3^+ Nitrogen-Hydrogen symmetric deformation band (centered around 2000-2220 cm^{-1},

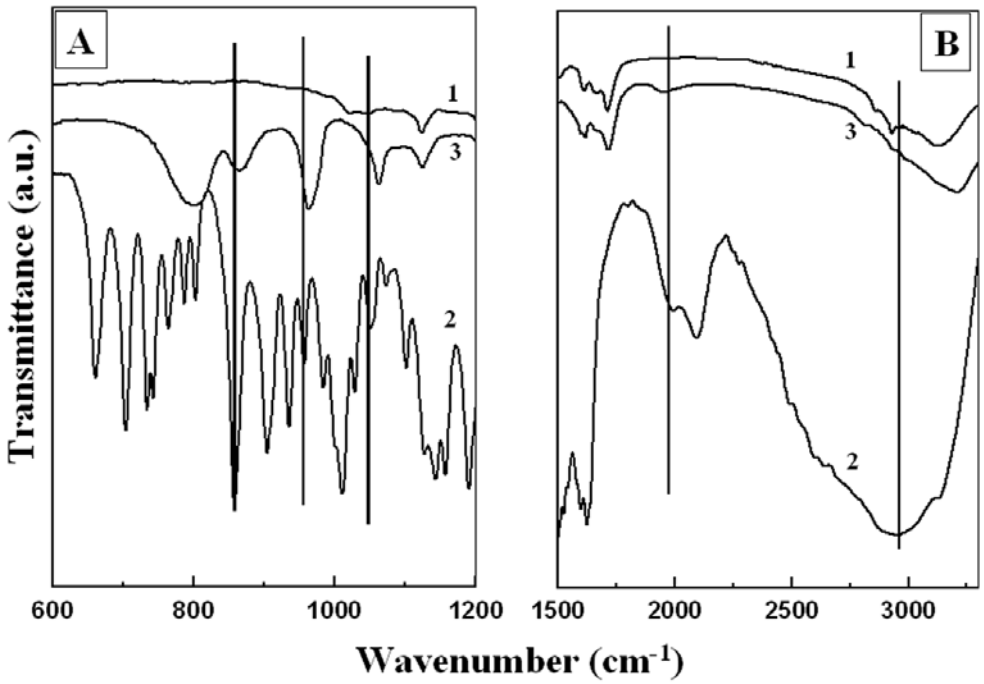

Figure 4.22: *Curves 1 and 2 in A) and B) show the FTIR spectra recorded in KBr pellet of pure $HAuCl_4$ and L-Lysine powder respectively. FTIR spectra taken in KBr pellet of the rotovapped powder obtained from concentrating the dialysed solution of PMA-Lysine with 10^{-3} M $HAuCl_4$ aqueous solution taken after 1 day (curve 3 in A and B).*

Curve 3 in Figure 4.22B) that was earlier present in the FTIR spectra of pure Lysine powder (Curve 2 Figure 4.22B). Although it is extremely difficult to differentiate an –OH and a broad amine vibrational band (centered around 3130 and 2960 cm^{-1} respectively, Curves 1 and 2 in Figure 4.22B), yet it appears that electrostatic coupling of Lysine outside the dialysis bag with $HAuCl_4$ might be a cause for the peak shift at 3200 cm^{-1} (Curve 3 in Figure 4.22B). This gives us a clear indication that it is Lysine, which

plays the important role of shape-modulating agent responsible for the formation of gold nanotriangles. Had Lysine not come out of the dialysis bag, we would have probably ended up with the gold nanotriangles that were previously obtained by the direct addition of PMA-Lysine with $HAuCl_4$ aqueous solution.

4.4.3 Supplementary proof of reaction mechanism

In order to comprehend the plausible mechanism a separate experiment was performed where in the first case instead of lysine, arginine (20 ml, 10^{-3} M) and in the second case aspartic acid (20 ml, 10^{-3} M) was used to complex separately with PMA. Thereafter the reaction was followed in the same way as was done with PMA-Lysine which has been elaborated in the previous note.

4.4.3.1 UV-Vis-NIR spectroscopy and TEM measurements

Figure 4.23A shows the UV-Vis spectra kinetics of the irradiated PMA-arginine reacted with $HAuCl_4$. No absorption is observed in the visible region of the electromagnetic spectrum till twelve hours of reaction as is evidenced from the aliquots taken after one hour (curve 1), five hours (curve 2) and twelve hours (curve 3) of reaction. However after one day of reaction, a strong absorption band appears in the NIR region only (curve 4), which suggests that, there must be a very high degree of anisotropy present in the nanoparticles in solution. This is confirmed from the representative TEM image taken after one day of the reaction, shown in Figure 4.23C, which shows that a mass of gold nanotriangles have clustered together and eventually in some areas appear as flat plate like structures. Similar clustering occurred when the reaction was carried out with aspartic acid, except that the solution contained only spherical gold nanoparticles (shown in Figure 4.23D). This was confirmed from the UV-Vis spectra kinetics taken at various time intervals for the reaction with aspartic acid, which shows a progressive increase in the absorption peak for spherical gold nanoparticles with no absorption in the NIR region (Figure 4.23B, curves1-4 taken after one, five, twelve and twenty-four hrs respectively).

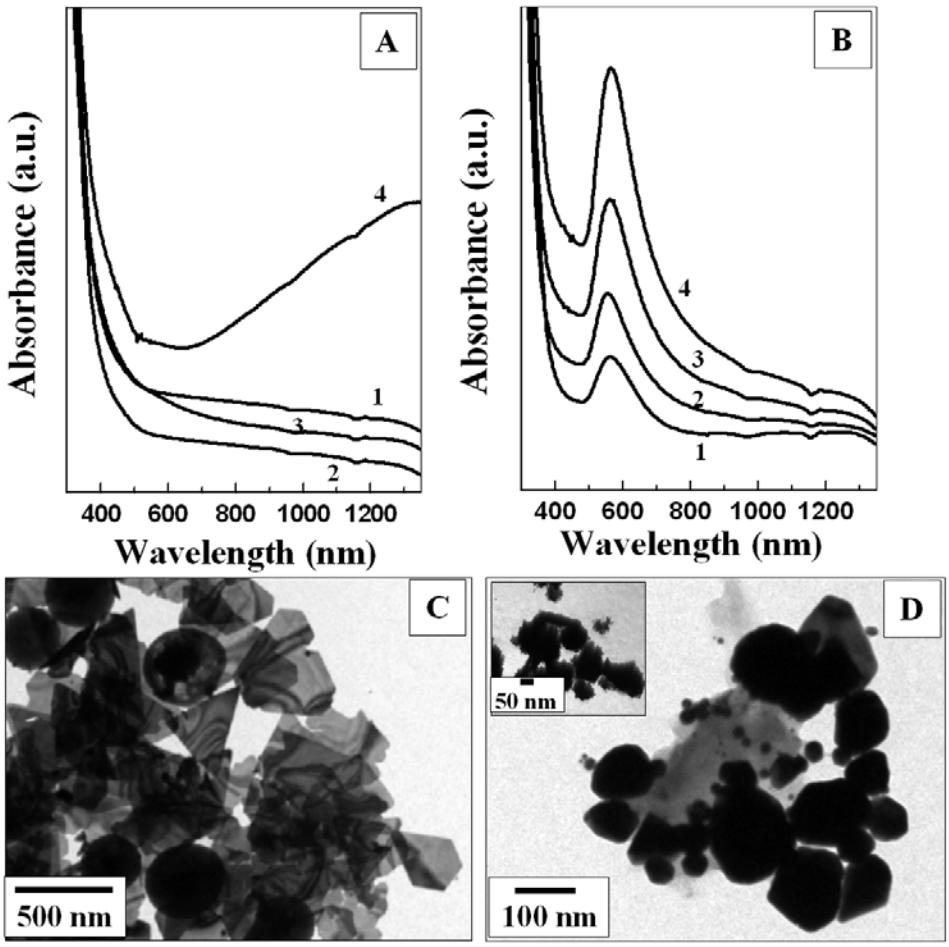

Figure 4.23: *UV-Vis-NIR spectra of direct addition of aqueous solution of 10^{-3} M $HAuCl_4$ into the UV-irradiated A) Arginine-PMA solution and B) Aspartic acid-PMA solution at different time intervals (Curve1-after 1 hour, curve 2- after 5 hrs, curve 3-after 12 hours and curve 4-after one day of reaction in both A and B). C and D): Representative TEM images taken after one day of reaction of arginine-PMA complex and aspartic acid-PMA complex respectively with $HAuCl_4$. The inset of D shows reaction of only irradiated PMA with $HAuCl_4$.*

It might be possible that other than electrostatic interactions present between the reacting species, stereochemistry is also playing a role in deciding the fate of the reaction system. Arginine, a basic amino acid, probably complexes with the PMA and then reduces $HAuCl_4$. Nevertheless since the size of arginine is larger than lysine, due to stereochemical reasons it is possible that this amino acid is hindered in its access to Au^{3+} thereby lowering the rate of reduction and thus formation of anisotropic nanostructures. Thus, the nature of the amino acid (in terms of acidity and basicity) does play a major

role in modulating the structure of the nanoparticle. A control experiment with only irradiated PMA being added to $HAuCl_4$ results in the formation of clusters of spherical nanoparticles (shown in the inset of Figure 4.23D).

4.4.4 Summary

To summarise, this piece of work demonstrates that L-Lysine can electrostatically complex with phosphomolybdic acid and the solution mixture when added to $HAuCl_4$ after photo-irradiation lead to the formation of truncated gold nanotriangles having a high degree of anisotropy. Following the same reaction in a 12.5-kDa cutoff dialysis bag alters the reaction such that due to the leakage of Lysine from the dialysis bag formation of such anisotropic structures totally dies out. The role of Lysine has evidently been brought out by control experiments where amino acids other that Lysine were used. While arginine (similar isoelectric point as Lysine) produced flat nanostructures upon reaction, the same was not obtained with aspartic acid suggesting that charge of the amino acid is dictating the morphology of the gold nanoparticles. Lysine thus plays the role of shape-modulating agent and thus the study can be extended to the use of such planned organic-inorganic hybrid nanostructures for the growth of anisotropic nanoparticles.

4.5 Conclusion

This chapter describes the use of organic-inorganic hybrid nanostructures for the synthesis of nanoparticles. Keggin ions since a long time have been used as a multifunctional molecule in various fields ranging from catalysis and photochemistry to hardcore biomedical applications. Here we have shown that these ions can complex with organic amino acids resulting in the formation of alluring nanohybrid structures with interesting morphologies. These fibres could then be modulated by the inherent photochemical property of Keggin ions to produce and assemble gold nanoparticles. The degree to which these hybrid nanostructures act as a faithful host to the reduced gold nanoparticles enthrall the possible use of them into the programmed assembly of various other nanomaterials of commercial value. It has also been shown that by suitable modification to the choice of reactants, anisotropic nanoparticles at room temperature can also be synthesized with these hybrid nanostructures. Thus this section opens up an

exciting possibility of use of such materials for the synthesis, growth and assembly of nanoparticles.

4.6 References

[1] El-Sayed, M. A. *Acc Chem.Res.* **2001**, *34*, 257.

[2] Buffat, Ph.; Borel, J-P *Phys.Rev.* **1976**, *A13*, 2287.

[3] Narayanan, R.; El-Sayed, M. A. *J.Am.Chem.Soc.* **2004**, *126*, 7194.

[4] Liao, H.; Hafner, J. H. *J. Phys. Chem. B* **2004**, *108,* 19276.

[5] Tsuji, M.; Hashimoto, M.; Nishizawa, Y.; Tsuji, T. *Materials Letters* **2004**, *58*, 2326.

[6] Aslan, K.; Lakowicz, J. R.; Geddes, C.D. *J. Phys. Chem. B* **2005,** *109,* 6247.

[7] Wang, L.; Chen, X.; Zhan, J.; Chai, Y.; Yang, C.; Xu, L.; Zhuang, W.; Jing, B. *J. Phys. Chem. B* **2005**, *109*, 3189.

[8] Sun, Y.; Mayers, B.; Xia, Y. *Nano Lett* **2003**, *3*, 675.

[9] Hao, E.; Kelly, K. L.; Hupp, J.T.; Schatz, G.C. *J. Am. Chem. Soc.* **2002**, *124*, 15182.

[10] Maillard, M.; Giorgio, S. ; Pileni, M.P. *Adv. Mater* **2002**, *14*, 1084.

[11] Chen, S.; Fan, Z.; Carroll, David L. *J. Phys. Chem. B* **2002**, *106,* 10777.

[12] Pastoriza-Santos, I.; Liz-Marza´n, L. M. *Nano Lett* **2002**, *2*, 903.

[13] Metraux, G.S.; Cao, Y.C.; Jin, R.; Mirkin, C.A. *Nano Lett.* **2003**, *3*, 519.

[14] Jin, R.; Cao, Y.; Mirkin, C.A.; Kelly, K. L.; Schatz, G.C.; Zheng, J.G. *Science* **2001**, *294*,1901.

[15] Jin, R.; Cao, Y.; Hao, E.; Metraux, G.S. *Nature* **2003**, *425*, 487.

[16] Hu, J.; Odom, T. W.; Lieber, C. M. *Acc. Chem. Res*. **1999**, *32*, 435.

[17] Patzke, G. R.; Krumeich, F. K.; Nesper, R. *Angew. Chem. Int. Ed*. **2002**, *41*, 2446.

[18] Li, M.; Mann, S. *Langmuir* **2000**, *16*, 7088.

[19] Liang, J. Z. *J. Appl. Polym. Sci*. **2002**, *83*, 1547.

[20] Shenton, W.; Douglas, T.; Young, M.; Stubbs, G.; Mann, S. *Adv.Mater.* **1999**, *11*, 253.

[21] Che, G.; Lakshmi, B. B.; Martin, C. R.; Fisher, E. R. *Langmuir* **1999**, *15*, 750.

[22] Xue, B.; Chen, P.; Hong, Q.; Lin, J.; Tan, K. L. *J. Mater. Chem.* **2001**, *11*, 2378.

[23] Davis, S. A.; Patel, H. M.; Mayes, E. L.; Mendelson, N. H.; Franco, G.; Mann, S. *Chem. Mater.***1998**, *10*, 2516.

[24] Caruso, F.; Lichtenfeld, H.; Giersig, M.; Mohwald, H. *J. Am. Chem. Soc.* **1998**, *120*, 8523.

[25] Hall, S. R.; Shenton, W.; Engelhardt, H.; Mann, S. *Chem. Phys. Chem*. **2001**, *3*, 184.

[26] Tanev, P. T.; Chibwe, M.; Pinnavaia, T. J. *Nature* **1994**, *368*, 321.

[27] Jun, Y. N.; Dabbs, D. M.; Aksay, I. A.; Erramilli, S. *Langmuir* **1994**, *10*, 3377.

[28] Dan, Nily, *Tibtech* **2000,** *18*, 370.

[29] Sun, X.; Dong, S.; Wang, E. *J.Am.Chem.Soc*. **2005**, *127*, 13102.

[30] Raman, N. K.; Anderson, M. T.; Brinker, C. J. *Chem. Mater.* **1996**, *8*, 1682.

[31] Mann, S.; Burkett, S. L.; Davis, S. A.; Fowler, C. E.; Mendelson, N. H.; Sims, S. D.; Walsh, D.; Whilton, N. T. *Chem. Mater.* **1997**, *9*, 2300.

[32] Bromley, L. A.; Cottier, D.; Davey, R. J.; Dobbs, B.; Smith, S.; Heywood, B. R. *Langmuir* **1993**, *9*, 3594.

[33] Convey, P. V.; Davey, R.; Griffin, J. L. W.; He, Y.; Hamlin, J. D.; Stackhouse, S.; Whiting, A. *J. Am. Chem. Soc*. **2000**, *122*,11557.

[34] Shi, H.; Qi, L.; Ma, J.; Cheng, H. *Chem.Commun*. **2002**, 1704.

[35] Shi, H.; Qi, L.; Ma, J.; Cheng, H.; Zhu, B. *Adv. Mater*. **2003**, *15*, 1647.

[36] Li, M.; Schnablegger, H.; Mann, S. *Nature*, **1999**, *402*, 393.

[37] Zhang, D.; Qi, L.; Yang, J.; Ma, J.; Cheng, H.; Huang, L. *Chem. Mater*. **2004**, *16*, 872.

[38] Yu, S. H.; Antonietti, M.; Colfen, H.; Hartmann, J. *Nano Lett* **2003**, *3*, 379.

[39] Pe´rez-Maqueda, L. A.; Matijevic, E. *Chem. Mater.* **1998**, *10,* 1430.

[40] Koliadima, A.; Pe´rez-Maqueda, L. A.; Matijevic, E. *Langmuir* **1997,** *13,* 3733.

[41] Huheey, J. E. *Inorganic Chemistry*, **(Third Edition)**, 698.

[42] Misono, M. *Mater. Chem. Phys.*, **1987**, *17*, 103.

[43**]** Serwicka, E. M.; Black, J. B.; Goodenough, J. B. *J. Catal.*, **1987***, 106*, 23.

[44] Hardwick, A.; Dickens. P. G.; Slade, R. C. T. *Solid State Ionirs* **1984,** *13*, 345

[45] a) Yamase, T.; Fujita, H.; Fukushima, K. *Inorg. Chim. Acra* **1988**, *151*, 15; b) *J. Mater. Chem.* **2005**, *15*, 4773.

[46] Pope, M. T.; Muller, A. *Angew. Chem. Int. Ed.*, **1991**, *30*, 34.

[47] Papaconstantinou, E. *Chem. Soc. Rev.* **1989,***18*,1.

[48] Troupis, A.; Hiskia, A.; Papaconstantinou, E. *Angew. Chem. Int. Ed.*, **2002**, *41*, 1911.

[49] a) Mandal, S.; Selvakannan, PR.; Pasricha, R.; Sastry, M. *J. Am. Chem. Soc*. **2003**, *125*, 8440. b) Mandal, S.; Rautaray, D.; Sanyal, A.; Sastry, M. *J. Phys. Chem. B.* **2004**, *108*, 7126. c) Rautaray, D.; Sainkar, S. R.; Sastry, M. *Langmuir* **2003**, *19*, 10095.

[50] Naruke, H.; Fukuda, N.; Yamase, T. *Acta Crystallographica* **2000**, *C56*, 177.

[51]. Link, S.; Wang, Z.I.; El-Sayed, M. A. *J.Phys.Chem.B.* **1999**, *103*, 3529.

[52] Gole, A.; Sastry, M. *Inorganic Chemistry Communication* **2001**, *4*, 568.

[53] Jelesarov, I.; Bosshard, H.R. *J.Mol.Recog.* **1999**, *12*, 3.

[54] Dam, T. K.; Roy, R.; Page, D.; Brewer, C.F. *Biochemistry* **2002**, *41*, 1359.

[55] Oda, M.; *J. Molec. Bio*. **1998**, *276*,775.

[56] Wenk, M. R.; Seelig, M. J. *Biochemistry* **1998,** *37*, 3909.

[57] Pierce, M.M.; Raman, C. S.; Nall, B. T. *Methods* **1999**, *19*, 213.

[58] Kumar, A.; Mandal, S.; Selvakannan, PR.; Pasricha, R.; Mandale, A. B.; Sastry, M. *Langmuir* **2003**, *19*, 6277.

[59]. Joshi, H.; Shirude, P. S.; Bansal, V.; Ganesh, K. N.; Sastry, M. *J. Phys. Chem. B.* **2004**, *108,* 11535.

[60] Mandal, S.; Rautaray, D.; Sastry M. *J.Mater.Chem*. **2003**, 13, 3002

[61] Oh, S-Y.; Yun, Y-J.; Hyung, K-H.; Han, S-H. *New. J. Chem.* **2004**, *28*, 495.

[62] The XRD patterns were indexed with respect to the unit cell structure of phosphomolybdic acid (a=b= 15.88 Å, c= 20.71 Å, PCPDF CAS No. 46-0482)

[63] The Aldrich Library of Infrared Spectra-Edition III, Charles, J. Pouchart, Aldrich Chemical Company, Wisconsin Pages 337 and 350.

CHAPTER V

Biological Synthesis of Mineral Crystals

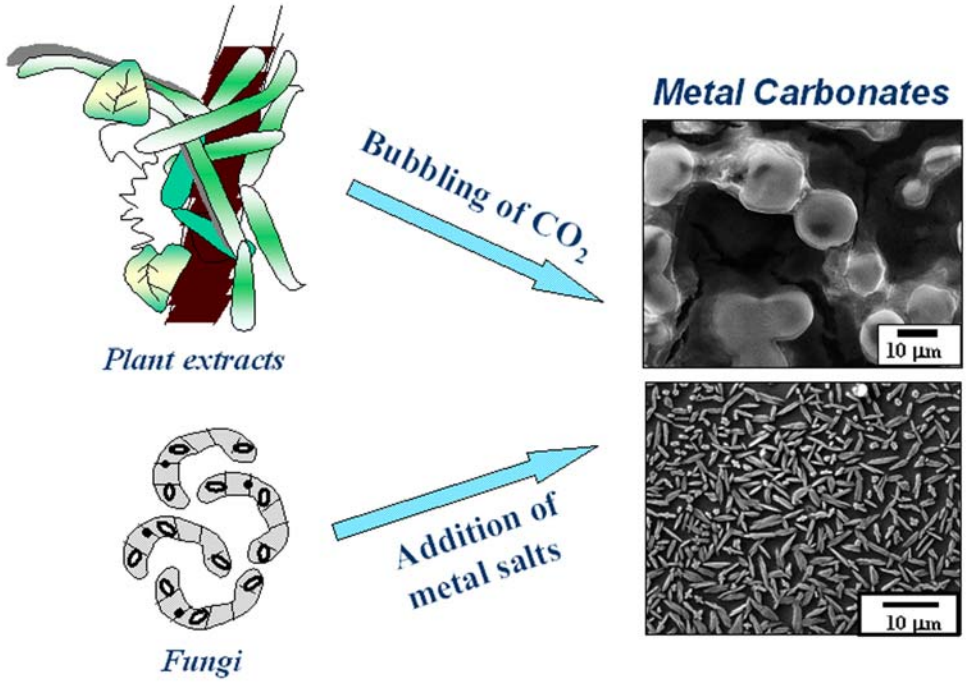

This chapter describes the growth of mineral crystals using a host of different materials that are of biological origin. Here, we show that CO_2 and characteristic proteins secreted by the fungus, when reacted with selected metal ions like Cd^{2+} and Pb^{2+}, lead to the formation of $CdCO_3$ and $PbCO_3$. It has also been shown that plant seeds and stem extracts when subjected to different experimental conditions lead to the formation of $CaCO_3$ of vaterite and calcite morphology respectively.

Part of the work presented in this chapter has been published and patented:

1). Rautaray, D.; Sanyal, A.; Ahmad A.; Sastry, M. *Cryst.Growth & Des.* **2005**, *5*, 399. 2) Sanyal, A.; Rautaray, D.; Bansal, V.; Ahmad A.; Sastry, M. *Langmuir* **2005***, 21*, 7220. 3) Sanyal, A.; Ahmad A.; Sastry, M. *Curr. Sci.* **2005**, *89*, 1742.4) Ahmad Absar, Rautaray, Debabrata, Sanyal, Ambarish, Sastry, Murali *US Patent Filed* (Ref. No. 20050214194)

5.1 Introduction

The term 'biomineralizaton', in a broader sense, can be given to the synthesis of inorganic mineral crystals by living organisms. There exists a diverse range of biominerals like calcium carbonate, calcium hydroxyapatite, silicates and iron-oxides. Magnetotactic bacteria having iron-rich magnetic crystals show fascinating magnetic properties that enable them to align and navigate along the Earth's geomagnetic field lines [1]. Mollusk shells have long been termed as the "Master-builders" by various authors, as they carve their shell out of calcium carbonate and a matrix of biomacromolecules. Nacre or the 'mother of pearl' is the best-studied architecture out of seven types of structures present in their shell [2]. It is this marvelous creation of nature that tempts various material scientists to mimic and comprehend the mechanism of crystal growth in bio-organisms. Yet even after much investigation of the biomaterials, regardless of their simple material constituents, they have multifunctional properties that are far superior to their human-made synthetic counterparts. Hence the search to mimic and recreate nature's design continues.

Another example of nature's exquisite creation is the presence of silica in the cell wall of diatoms. Diatoms, which are a major contributor to earth's carbon-fixation, are unicellular organisms are almost found in every aquatic environment [3]. Mineral growth in prokaryotic organisms like bacteria may be primarily classified into two different modes; one is Biologically Induced Mineralization (BIM) while the other is Biologically Controlled Mineralization (BCM). The difference lies in the fact that in the latter method, the organism exerts a great degree of control over the mineralization process. Minerals through this process are generally synthesized either within organic matrix or in vesicles inside the cell, thus making the process genetically and metabolically controlled [4].

Crystallization within an organic matrix is thus a key step in natural biomineralization. In this milieu, it would be totally unfair if we do not have a discussion on the creative works of Professor Pieter Harting who during the last phase of the 19th century coined the experiments, which we better know as biomimetic inorganic chemistry [5]. It was in 1917 when Sir D'Arcy Thomson offer in material form a physicogeometrical study on the growth of many beautiful protozoan cellular assemblies [6]. This lead to the synthetic growth of mineral structures with a greater degree of

fidelity and resemblance to natural structures. Apart from biological systems like silica sponges, mollusk shells, diatoms, bone (collagen), teeth and enamel are also exquisite forms of natural mineralization. Calcium hydroxyapatite (calcium phosphate), the principal component found in teeth and bones is biocompatible [7] and biodegradable [8,9].

Laboratory synthetic methods for the growth of $CaCO_3$ include crystallization at Langmuir monolayers [10], on self-assembled monolayers (SAM'S) [11], within lipid bilayer stacks [12], or on functionalized polymer surfaces [13] and in vesicles [14]. Various other metal carbonates like $SrCO_3$, $BaCO_3$, $CoCO_3$ and $PbCO_3$ have been synthesized in the presence of polyelectrolytes [15]. Even though many industrially important technologies like bioremediation of toxic metal ions using bacteria [16] and yeast [17] exist, it has been only very recent that similar types of reactions have been tried with fungi and actinomycetes. In this laboratory, have earlier synthesized noble metal nanoparticles namely Au, Ag [18, 19], quantum dots like CdS [20] have been synthesized using fungus, actinomycetes and leaf extracts [21]. At that stage we could very little infer as to which is the principal protein or the enzymatic mechanism that lead to such exotic structures. In our previous studies, have even shown that metal carbonates like $CaCO_3$, $SrCO_3$ can be synthesized using the fungus *Fusarium oxysporum* [22, 23]. The feature of our work lies in the fact that the morphology of the mineral carbonates is totally dictated by the enzymatic proteins and that no external source of CO_2 is required for the synthesis.

In this chapter we address the following questions:

(a) Is it possible to remove heavy metal ions like Cd^{2+} and Pb^{2+} by means of production of their respective carbonates through a fungus based method?

(b) Will the fungus tolerate the toxicity and in turn be able to generate the metal carbonates?

(c) Can other polymorphs of $CaCO_3$ be synthesized at room temperature without using any harsh condition?

(d) If so, can we have a preliminary protein profile for the formation of those unstable polymorphs?

(e) Whether minerals like calcium hydroxyapatite be synthesized by a truly biological process?

5.2 Biological synthesis of lead and cadmium carbonates:

A plant pathogenic fungus, *Fusarium oxysporum* was isolated from the plant, *Rosa* sp. that was infected by a natural biological attack of this fungus. Thereafter, the fungus isolated was maintained on potato-dextrose-agar (PDA) slants. Stock cultures were maintained by sub-culturing at monthly intervals. After growing at pH 7 and 27 ^{o}C for four days, the slants were preserved at 15 ^{o}C. From an actively growing stock culture, subcultures of the fungus were made on fresh slants and after four days of incubation at pH 7 and 27 ^{o}C were used as the starting materials for fermentation experiments. For preparation of the $PbCO_3$ and $CdCO_3$ crystals, the fungus was grown in 500 ml Erlenmeyer flasks containing 100 ml **MGYP** medium, which is composed of **M**alt extract (0.3 %), **G**lucose (1 %), **Y**east extract (0.3 %) and **P**eptone (0.5 %). After adjusting the pH of the medium to 7, the culture was grown under continuous shaking on a rotary shaker (200 rpm) at 27 ^{o}C for 96 hours. After 96 hours of fermentation, mycelium of the fungus was separated from the culture broth by centrifugation (5000 rpm) at 20 ^{o}C for 20 minutes and then the mycelia were washed thrice with sterile distilled water under sterile conditions. The harvested mycelia mass (20 g wet wt. of mycelia) of *Fusarium oxysporum* was then resuspended in 100 ml each of 10^{-3} M $Pb(NO_3)_2$ and $CdCl_2$ solutions in 500 ml Erlenmeyer flasks. The flasks were then plugged with cotton and put into a shaker at 27 ^{o}C (200 rpm) and the reaction carried out for a period of 24 hours. Thereafter, the biomass was separated from the filtrate and both the fungal biomass and the filtrate were subjected to different chemical analysis as mentioned below in order to investigate the bio-transformation of the electrolyte salts into the respective carbonates. The residue after 1 day of reaction was washed thoroughly several times using copious amounts of double-distilled water and the washed biomass was cast in the form of films onto Si (111) substrate for further analysis. The filtrate was subjected to centrifugation at 10000 rpm and the pellets obtained were washed repeatedly with copious amounts of double distilled water. The purified pellets were solution-cast in the form of films onto different solid supports for further analysis.

5.2.1 Scanning Electron Microscopy (SEM) studies

5.2.1.1 Spherical $PbCO_3$: Figure 5.1A shows representative SEM images recorded from solution-cast films of the aqueous $Pb(NO_3)_2$ solution after exposure to *Fusarium oxysporum* for 1 day. It is observed from the SEM image that the sample mainly consists of large, highly irregular structures of size greater than 10 microns. The whole region of the sample is enveloped with clusters as is shown in Figure 5.1A. A higher magnified image of the cluster would edify about the nature of the structure. Thus at progressively higher magnifications (Figure 5.1B-D), these structures are seen to be aggregates of smaller particles that are uniform in size and highly spherical in morphology. The size of the individual spherical crystallites in the large assemblies ranges between 120-200 nm.

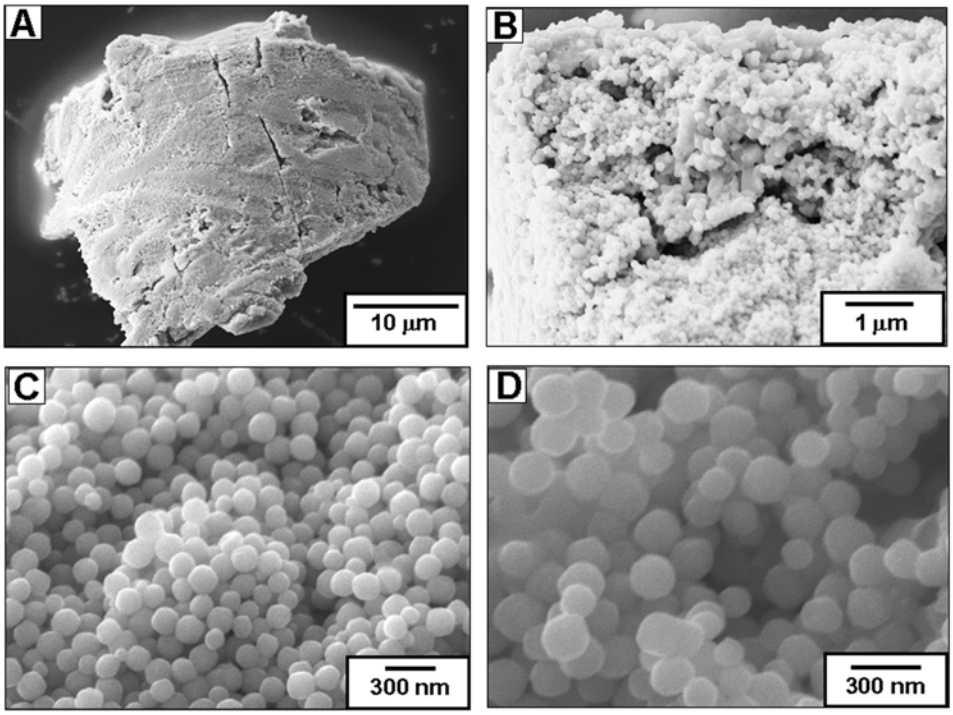

Figure 5.1: *(A)–(D) SEM micrographs at different magnifications of $PbCO_3$ crystals formed after 1 day of reaction of aqueous Pb^{2+} ions with the fungus, Fusarium oxysporum.*

The structures are composed of spherical aggregates and are very much different from the generally observed cerrusite ($PbCO_3$ crystal) structure. Antonietti *et al.* have synthesized $PbCO_3$ crystals in solution in the presence of double-hydrophilic block copolymers (DHBCs) [24] and have observed the formation of disk-like plates (in the presence of

PEG-*b*-PMAA) and flat hexagonal plates of $PbCO_3$ (in the presence of PEG-*b*-[(2-[4-dihydroxyphosphoryl]-2-oxabutyl) acrylate ethyl ester]) whereas poorly defined starlike $PbCO_3$ platelets were obtained in the absence of block copolymers.

5.2.1.2 Needle-shaped $CdCO_3$: Figure 5.2A & B show representative SEM images recorded from extracellularly grown $CdCO_3$ crystals after reaction of aqueous Cd^{2+} ions with the fungus, *Fusarium oxysporum* for 1 day. A large number of very uniform needle-shaped crystals of $CdCO_3$ are observed in the SEM micrograph (Figure 5.2A). Viewed at higher magnification (Figure 5.2B and C), the $CdCO_3$ needles can be seen in greater detail.

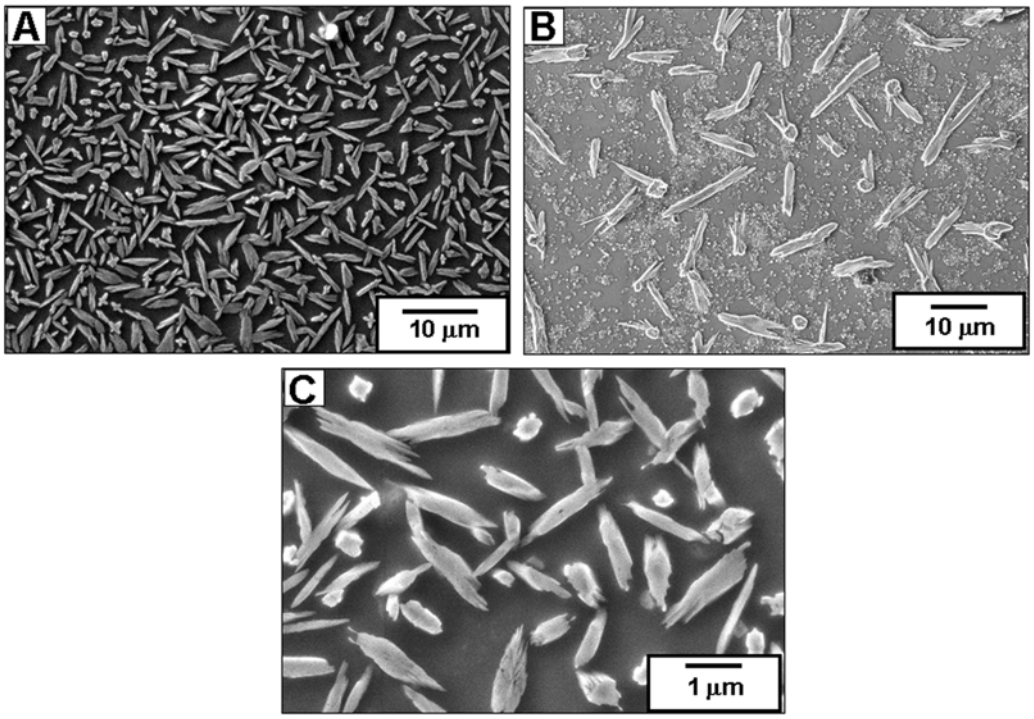

Figure 5.2: *(A)–(C) Representative SEM micrograph at different magnifications of $CdCO_3$ crystals obtained after reaction of $CdCl_2$ with the fungus, Fusarium oxysporum.*

The length of the needles varies from 2 to 6 µm while the width ranges from 100 to 300 nm. From the magnified image of Figure 5.2B and C, it can be seen that along with the needle shaped crystals, some spheroaggregates are present at the terminal part of the

needles. It might be possible that the needle shaped crystals are formed from the spherical crystals the formation of which had been kinetically driven.

5.2.1.3 Extracellular proteins: To determine the nature of protein(s) responsible for the crystal morphology control, the extracellular proteins secreted by the fungus in the filtrate obtained in the aforesaid experiment in the absence of lead and cadmium ions were salted out overnight at 4 ^{o}C using ammonium sulphate precipitation followed by centrifugation. The proteins obtained thereafter, were dissolved in minimal volume of deionized water and dialyzed (using 12 kDa cutoff dialysis membrane). The dialyzed protein fraction containing a mixture of proteins was further purified by ion exchange columns.

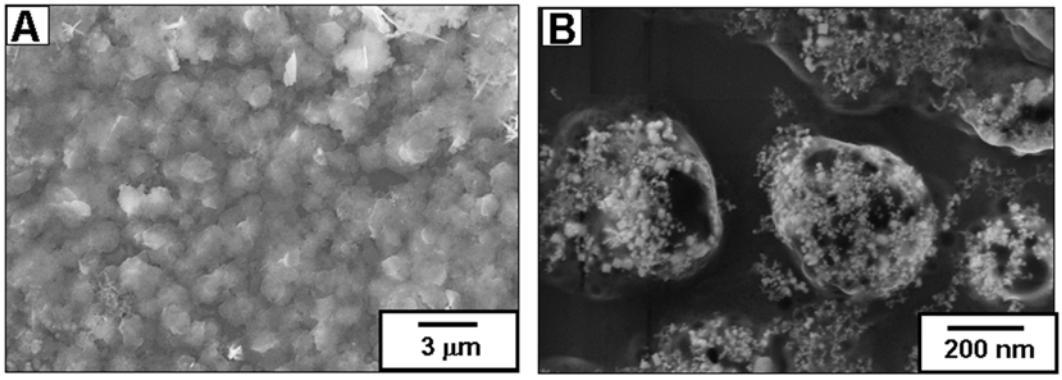

Figure 5.3: *(A), (B) SEM micrographs of $PbCO_3$ crystals grown using protein fraction 1 extracted from the fungus, Fusarium oxysporum.*

The various fractions obtained from CM-Sephadex column were checked for their activity. Out of various fractions obtained, only two fractions showed positive results in modulating the morphology of the lead and cadmium carbonate crystals. Out of these two protein fractions, one was responsible for the shape control of $PbCO_3$ (protein fraction 1) while the second protein fraction (protein fraction 2) was responsible for shape control of $CdCO_3$ crystals. These two protein fractions are anionic in nature suggesting that the interaction of the proteins with the lead and cadmium carbonate crystals could occur electrostatically with the metal ions exposed at specific crystallographic faces. Figure 5.3A, B shows SEM images of $PbCO_3$ crystals grown in the presence of protein fraction

1 after bubbling CO_2 into the protein fraction part. We can observe that the particle morphology obtained in this case is fairly similar to that obtained when the fungal extract was added to $PbCl_2$ (Figure 5.1 A-D) which suggests that the protein fraction 1 is definitely the major component dictating the morphology of the corresponding carbonate. Nonetheless, that the SEM image of Figure 5.3A has been smeared with a sheath of protein that makes the spherical crystals appear blurred.

However, in a similar manner with the second protein fraction (protein fraction 2), the results obtained were entirely different. Figure 5.4A shows the SEM image of the $PbCO_3$ crystals, grown by bubbling CO_2 into protein extract 2, to be essentially prismatic and in no way analogous to the spherical type of crystals obtained when the fungal extract was added to $CaCl_2$ solution.

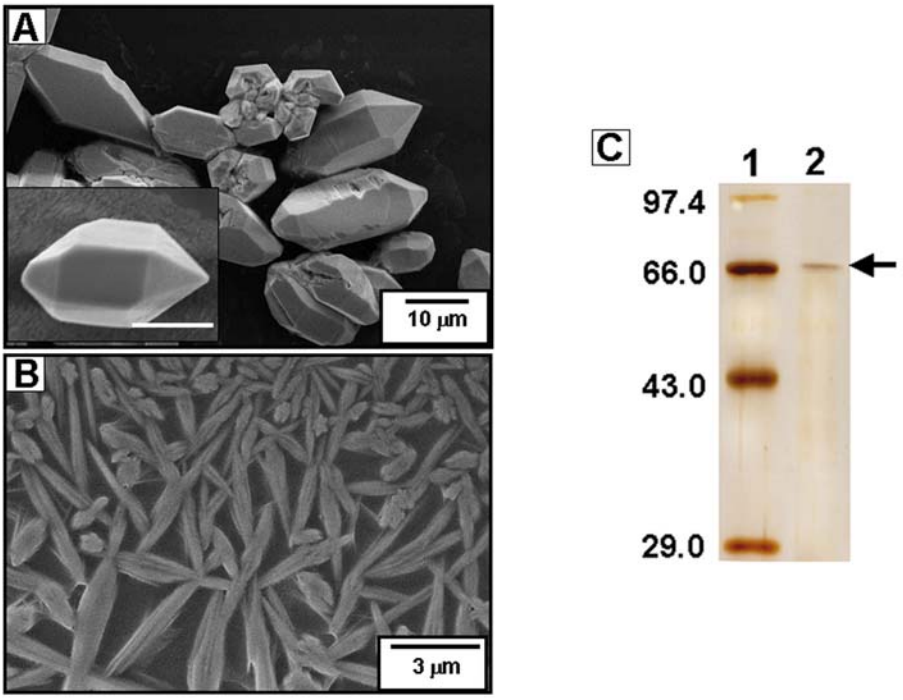

Figure 5.4: *(A), (B) SEM micrographs of $PbCO_3$ and $CdCO_3$ crystals respectively obtained by the reaction of $Pb(NO_3)_2$ and $CdCl_2$ respectively with the protein fraction 2. The scale bar in the inset of A corresponds to 2 µm.* ***C:*** *SDS-PAGE analysis of the protein fraction responsible for the needle-like morphology of $CdCO_3$ crystals (lane 2). Lane 1 shows standard protein molecular weight markers with the corresponding molecular weights in kDa. The arrow highlighting the band in lane 2 indicates the protein responsible for the morphology control of $CdCO_3$ crystals.*

This attests that although the morphology is dictated by a single major protein, yet contributions from other minor proteins cannot be ruled out. Whereas, the second protein fraction 2, when reacted with $CdCl_2$ and CO_2 resulted in the growth of elongated shape structures (SEM image of Figure 5.4B). The structures were very much similar to that obtained by simply reacting the fungal extract with the metal salt. This suggests that the protein responsible for morphology control in this case is different from that responsible for the formation of $PbCO_3$. In order to identify better the individual proteins in each of the fractions (protein fractions 1 and 2) leading to morphology control, gel electrophoresis analysis of the two protein fractions was carried out. While the proteins in protein fraction 1 could not be easily separated by SDS-PAGE, meaningful results were obtained for protein fraction 2 that was responsible for the morphology control of $CdCO_3$ crystals (lane 2, SDS-PAGE data shown in Figure 5.4C). A comparison of the protein bands in this fraction with the markers (Figure 5.4C, lane 1) indicates that the $CdCO_3$ shape-modulating protein has a molecular weight of ~ 68 kDa. As we had already stated, though this protein contributes to a major extent in controlling the $CdCO_3$ crystal morphology, contribution of other minor proteins in the crude extract cannot be ruled out.

5.2.2 Energy Dispersive Analysis of X-rays (EDAX) and Fourier Transform Infrared Spectroscopy (FTIR) measurements

In order to understand the chemical composition of these spherical crystallites synthesized using *Fusarium oxysporum* Energy Dispersive Analysis of X-rays (EDAX) measurement was done. This was conveniently done by spot-profile EDAX measurement of one of the spherical crystallites grown using the fungus (curve 1, Figure 5.5A). In addition to the expected Pb, C and O signals from $PbCO_3$, we observe the presence of N and S signals in the $PbCO_3$ crystals. (The Si signal is from the substrate). The N and S signals in the EDAX spectrum indicate the presence of proteins within/on the spherical $PbCO_3$ crystallite. A very similar result was obtained in the EDAX spectrum of $CdCO_3$ (curve 2 in Figure 5.5A).

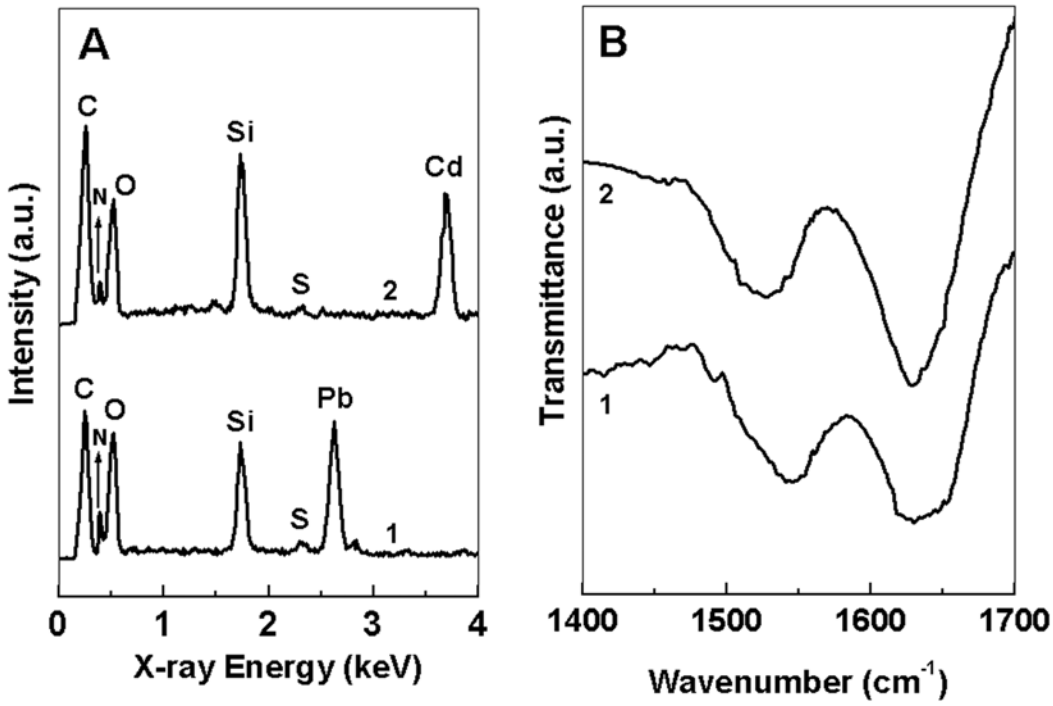

Figure 5.5: *(A) Spot-profile EDAX spectra recorded from films of $PbCO_3$ (curve 1) and $CdCO_3$ (curve 2) crystals synthesized using the fungus, Fusarium oxysporum. (B) FTIR spectra showing the amide I and II bands recorded from $PbCO_3$ (curve 1) and $CdCO_3$ (curve 2) crystals obtained by the reaction of aqueous Pb^{2+} ions and Cd^{2+} ions with the fungus, Fusarium oxysporum respectively.*

That these signals are likely to be due to the proteins secreted by the fungus is supported by the FTIR measurement of the $PbCO_3$ and $CdCO_3$ crystals (Figure 5.5B, curves 1 and 2) which clearly shows the presence of amide I and II bands at 1542 and 1633 cm^{-1} respectively [25]. This observation indicates that the $PbCO_3$ crystals in the spherical morphology are present with proteins that are possibly occluded into the crystals or are bound to the surface of the crystals thereby acting as a sort of glue holding the spherical crystallites together in the superstructure.

5.2.3 X-Ray Diffraction (XRD) measurements:

XRD analysis of the biological $PbCO_3$ crystals formed by the reaction of aqueous Pb^{2+} ions with *Fusarium oxysporum* for 1 day was performed and the diffraction pattern obtained is shown as curve 1 in Figure 5.6.

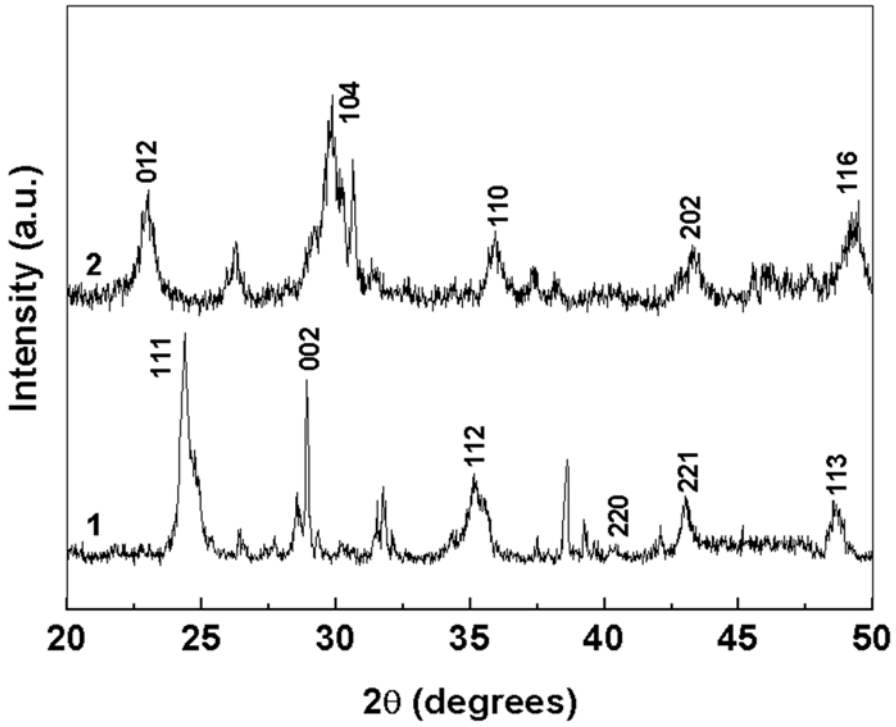

Figure 5.6: *XRD patterns recorded from $PbCO_3$ (curve 1) and $CdCO_3$ (curve 2) crystals obtained by the reaction of aqueous Pb^{2+} ions and Cd^{2+} ions with the fungus, Fusarium oxysporum respectively.*

A number of Bragg reflections are identified and have been indexed with reference to the unit cell of the $PbCO_3$ structure (a = 5.178 Å, b = 8.515 Å, c = 6.146 Å; space group *Pmcn*) [26]. The broad Bragg reflections in the XRD spectrum indicate that the $PbCO_3$ crystals are rather small and is consistent with the SEM analysis that revealed the crystallites to be of 120-200 nm dimensions (Figure 5.1C and D). The XRD pattern recorded from the needle-like $CdCO_3$ crystals is shown as curve 2 in Figure 5.6. A number of Bragg reflections are identified and have been indexed with reference to the unit cell of the $CdCO_3$ structure (a = 4.929 Å, c = 16.30 Å; space group *R3c*) [26].

As mentioned above, heavy metal ions such as lead and cadmium are considered to be toxic to all types of cells, and hence it is important to establish whether the fungus *Fusarium oxysporum* survives the exposure to the Pb^{2+} and Cd^{2+} ions.

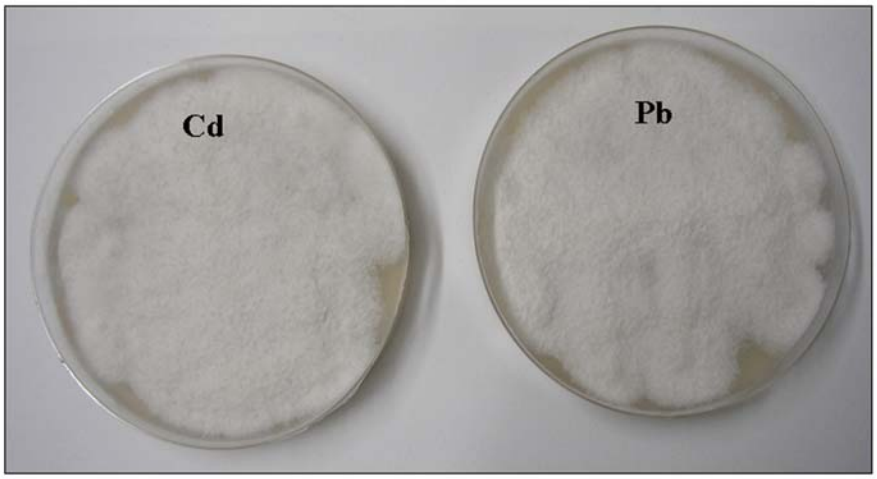

Figure 5.7: *Pictures showing growth of fungus, Fusarium oxysporum after exposure to cadmium (plate to the left) and lead ions (plate to the right) for a period of 10 days.*

To answer this crucial question, the fungus from the reaction medium containing lead and cadmium ions after 1 day of reaction was separately washed and plated in a Petri plate containing MGYP medium. Pictures of the fungus after exposure to cadmium (Petri plate to the left) and lead ions (Petri plate to the right) and growth in the MGYP medium for a period of 10 days are shown in Figure 5.7. It can be clearly seen that the fungus survives the exposure to the Pb^{2+} and Cd^{2+} ions and grows quite readily in the nutrient medium.

5.2.4 Summary

We have shown that heavy metal ions such as Pb^{2+} and Cd^{2+} can be removed from aqueous solutions by exposure to the fungus, *Fusarium oxysporum*. The detoxification occurs by a process of metal carbonate formation. The metal carbonates are useful by-products and possess morphologies that are directed by proteins secreted by the fungus. The metal ions are not toxic to the fungus under the experimental conditions of this study and thus highlight the potential of this process in bioremediation and large-scale mineral growth.

5.3 Biological synthesis of stable vaterite crystals:

As already mentioned, biological systems provide a number of examples of inorganic materials such as $CaCO_3$, magnetic iron oxide and amorphous silica of exquisite morphology with structural and functional value. Laboratory processes for the synthesis of $CaCO_3$ crystals have hitherto relied on an external source of CO_2 for reaction with Ca^{2+} ions and synthetic molecules or very specific proteins extracted from calcareous microorganisms to achieve morphology control. It is known that CO_2 gas, acetone, alcohols, aldehydes and volatile organic acids are released by germinating seeds and roots [27]. In our experiment, uniform sized chickpea seeds were washed with sterile distilled water and soaked for 45 min. in water. After soaking, the seeds were surface-sterilized with Na-hypochlorite solution for 2-3 min., washed with copious amounts of sterile distilled water and spread on moistened Whatman filter paper in an autoclaved Petridish (150 mm diameter). The closed Petridish was placed in the dark at 25-26 ^oC for 3 days to initiate germination. 5-8 germinated seeds were then placed on a moistened filter paper support in an autoclaved test-tube containing 20 ml sterile aqueous solution of 10^{-3} M $CaCl_2$ (test-tubes in Figure 5.8).

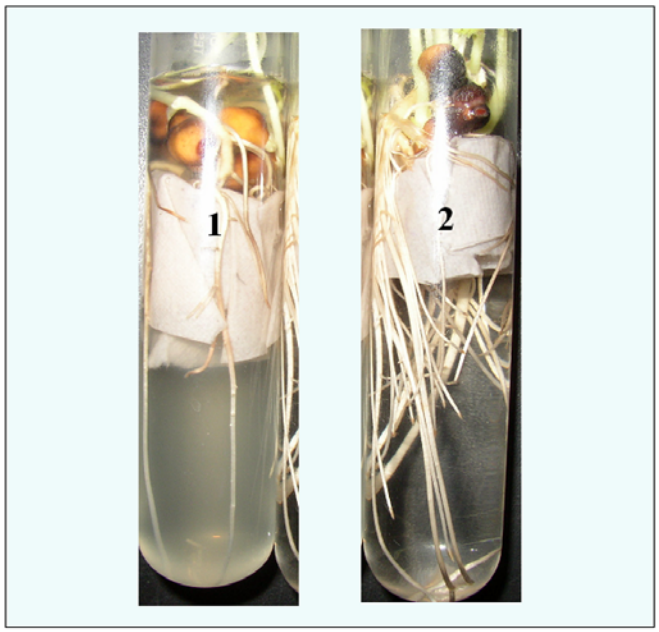

Figure 5.8: *Picture of test tubes with germinated chickpea seeds immersed in $CaCl_2$ solution (test-tube 1) and distilled water (test-tube 2) for 5 days.*

The test-tube was then plugged with cotton and incubated at 25-26 ^{o}C. The roots from the seeds were allowed to grow into the aqueous $CaCl_2$ solution for 5 days. After 5 days of reaction the aqueous solution became milky as can be seen from the photograph of the test-tube with the seeds (Figure 5.8, test-tube 1), indicating $CaCO_3$ crystallization. In comparison a test-tube containing pure distilled water with chickpea seeds after 5 days of exposure showed no cloudiness in the aqueous medium (Figure 5.8, test-tube 2). The solution from test-tube 1 was drop-cast in the form of films onto Si (111) substrates for further characterization. For FTIR measurements the 5-days reacted biogenic $CaCO_3$ was lyophilized into powders and taken in a KBr pellet.

5.3.1 Scanning Electron Microscopy studies

5.3.1.1 Spherical $CaCO_3$: Figure 5.9A-D show SEM images recorded at progressively higher magnifications from solution-cast films of the aqueous $CaCl_2$ solution after reaction with chickpea roots for 5 days.

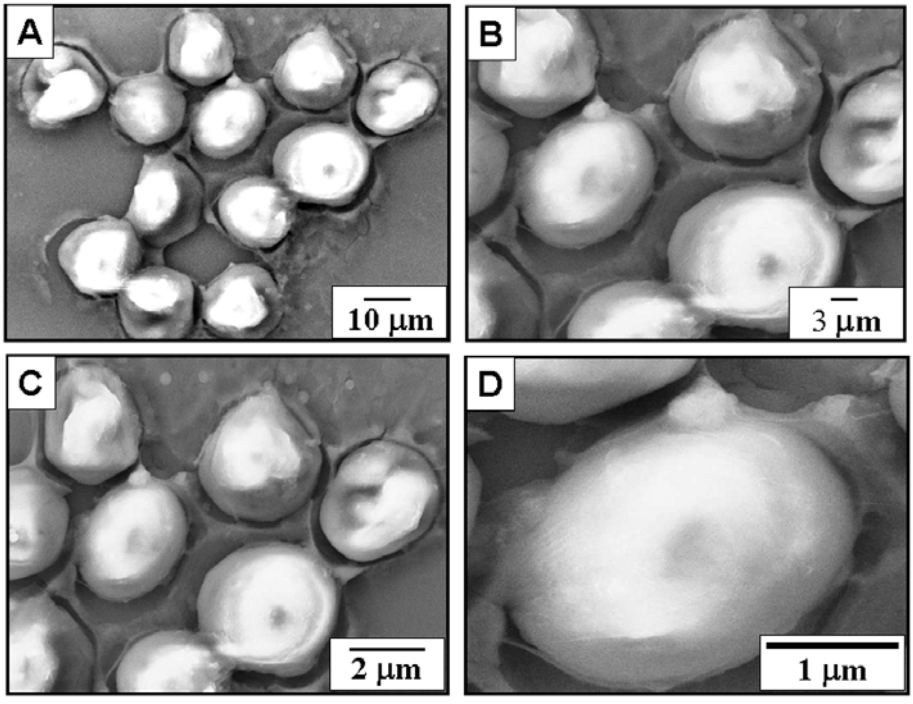

Figure 5.9: *(A)-(D) Representative SEM images of $CaCO_3$ crystals formed by reaction of Ca^{2+} ions with roots of chickpea seeds.*

The formation of quasi-spherical $CaCO_3$ crystals of fairly uniform size is observed. At higher magnification, the crystals are seen to be ellipsoidal in shape (similar to vaterite polymorph, an unstable form of $CaCO_3$) and having a smooth growth front (Figure 5.9D). It seems from the SEM images of Figure 5.9B-D that the crystals are held by some organic matrix which is thereby stabilizing the morphology of the crystal. While the exact nature of binding of the proteins with specific crystallographic faces needs elaboration, the location of the proteins in the crystals (surface adsorption vs. uniformly intercalated in the crystals) may be indirectly determined by removal of the proteins via calcination.

5.3.1.2 Calcined $CaCO_3$: It is most likely that the proteins have played a major role in the polymorph selectivity of the vaterite crystals, to prove this; we calcined the sample at 300 ^oC for 3 hours. We observed from the drop-cast SEM images of Figure 5.10A, B that there was a complete transformation in the morphology of the crystals. The crystals have predominantly changed from spherical to the usual rhombohedral geometry of calcite crystals.

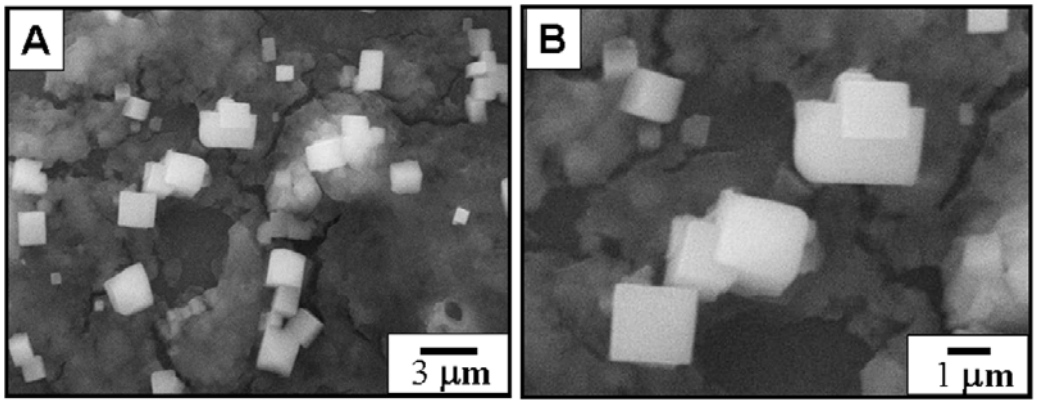

Figure 5.10: *(A), (B) SEM picture of biogenic $CaCO_3$ crystals shown in Figure 5.8B and C after calcination at 300 ^0C.*

However it remains unclear whether the heat treatment caused removal of proteins or has directly altered the morphology of the crystals from an unstable form to a more thermodynamically stable form. In order to make clear the process going on, we devised 2 separate experiments, wherein the first experiment, chickpea seeds were soaked in water for 5 days and the aqueous component separated by filtration. The aqueous fraction containing proteins released by the root fraction during germination was then taken with

10^{-3} M $CaCl_2$ solution and CO_2 was bubbled very slowly through this solution for 24 h. This solution was drop-cast onto Si (111) wafers and analyzed by SEM. Figure 5.11A shows a representative SEM image of the $CaCO_3$ crystals formed in the control experiment. The $CaCO_3$ crystals have a predominantly spherical morphology and appear almost identical to the ones obtained in the experiment involving in-situ reaction of Ca^{2+} ions with chickpea seeds (Figures 5.9 A-D). The pH of the chickpea seed-$CaCl_2$ reaction medium 24 h after reaction was measured to be ca.5 and is therefore weakly acidic. It is a well-known fact that vaterite formation is feasible under acidic conditions [28], and hence the pH of the reaction medium modulated by bioorganic molecules released from the chickpea roots along with the surface-bound proteins may be playing an important role in stabilization of the vaterite polymorph.

In order to identify the proteins that stabilize the vaterite crystals grown by the reaction of Ca ions with chickpea seeds, we carried out a separate experiment where the solution containing biogenic $CaCO_3$ crystals was treated with 4 % sodium hypochlorite (NaOCl) solution. Sodium hypochlorite treatment is known to be an efficient method to denature any surface bound proteins due to its oxidizing capability and is also capable of detaching them from the surface. Figure 5.11B shows a representative SEM image of one biogenic vaterite crystal after treatment with NaOCl solution.

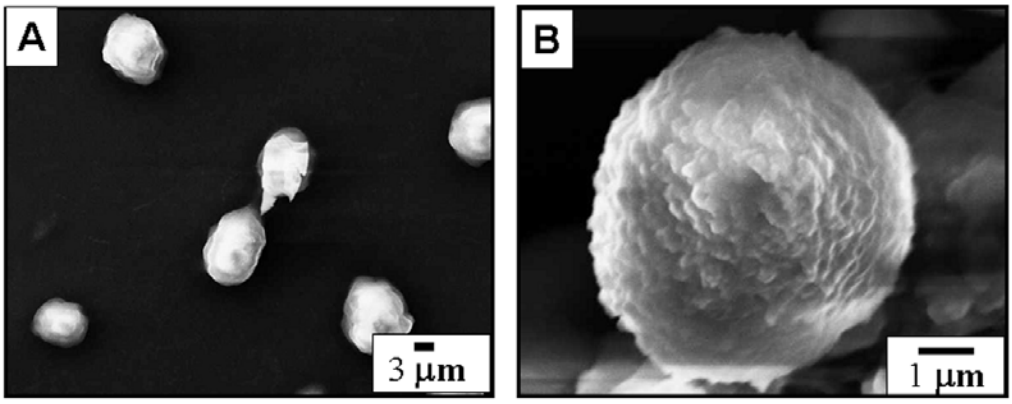

Figure 5.11: *(A) SEM image of $CaCO_3$ crystals formed using the extract secreted by chickpea seeds. (B) Magnified SEM image of a vaterite crystal grown in the presence of chickpea seeds after treatment with NaOCl solution.*

It can be clearly seen from this image that the surface of the crystal becomes very rough upon removal of the surface bound proteins by NaOCl treatment. The protein-$CaCO_3$ composite structure inferred from the SEM studies discussed above may arise from Ca^{2+}-ion mediated aggregation of the proteins secreted by the chickpea roots that is then followed by reaction of the Ca^{2+} ions with CO_2 within the protein aggregates thereby yielding templated $CaCO_3$ crystals.

5.3.2 EDAX and FTIR evidence for presence of proteins

The chemical composition of the spherical vaterite crystals was studied by spot-profile EDAX and is shown in Figure 5.12A (curve 1).

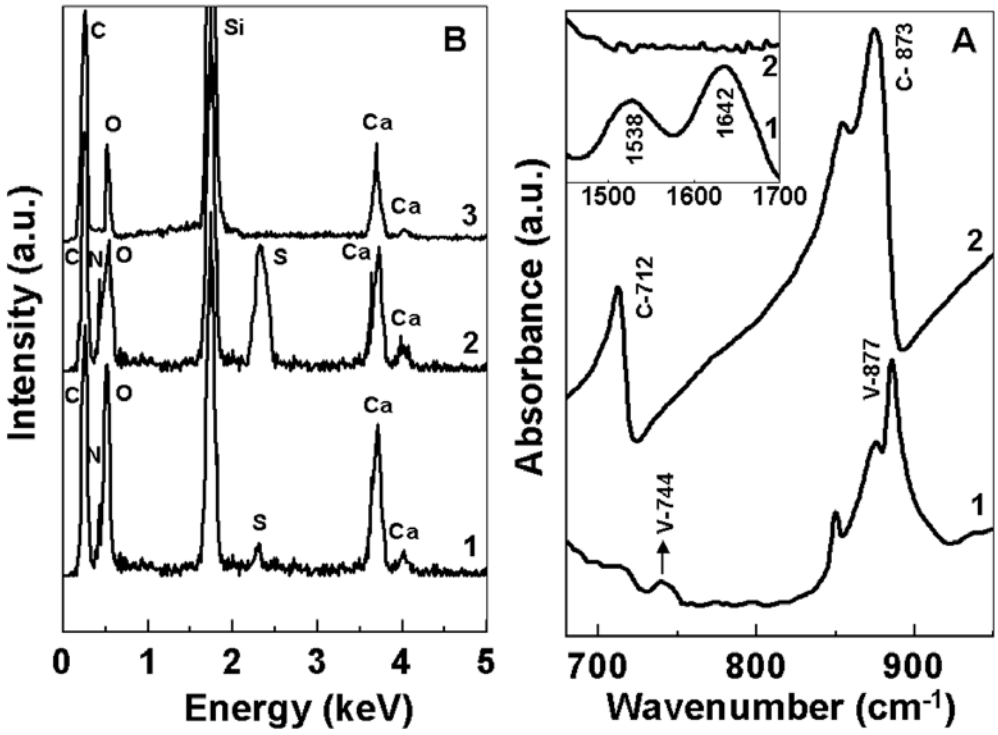

Figure 5.12: *(A) Spot-profile EDAX spectra recorded from films of $CaCO_3$ crystals synthesized using chickpea seeds: curve 1, from the spherical crystals; curve 2, from the neck region; curve 3, after calcination. (B) FTIR spectra recorded from films of $CaCO_3$ crystals synthesized using chickpea seeds: curve 1, from the spherical crystals; curve 2, after calcification (V stands for vaterite and C for calcite). The inset shows the protein I and II bands in the spherical crystals (Curve 1) and their absence after calcination (Curve 2).*

In addition to the expected Ca, C, and O signals, strong N and S signals are also observed. These signals are believed to arise from proteins either on the surface of the vaterite crystals or occluded within the crystals. That these signals are likely to be due to proteins secreted during root growth is supported by the FTIR results (inset of Figure 5.12B, curve 1) which clearly show the presence of the amide I and II bands at 1642 and 1538 cm-1, respectively. Thus, proteins secreted by the chickpea roots play a crucial role in the stabilization of the $CaCO_3$ structure. From Figure 5.9B, the presence of a sheath of organic matrix between the 2 crystals was inferred, hence EDAX spot analysis was taken from this neck-region (curve 2 in Figure 5.12A). To our supposition there is a marked increase in the intensity for N and S signals as compared to the EDAX analysis from the spherical crystals. This confirms that the proteins hold the crystals very similar to that of a brick and mortar structure. FTIR analysis of powders of 5-day-reacted biogenic $CaCO_3$ crystals taken in a KBr pellet is shown in Figure 5.12B, curve 1). The absorption bands centered at 877 cm-1 (strong) and 744 cm-1 (weak) are characteristic of vaterite [29].

The transformation of the crystals from vaterite to calcite was brought about by calcination that caused removal of surface-bound proteins. This can be seen from the complete disappearance of the amide I and II peaks shown in the inset of Figure 5.12B (curve 2). A completely new set of absorbance peaks appear in the FTIR spectra of the calcined sample (curve 2 in Figure 5.12B) centered around 712 and 873 cm^{-1} which are characteristic of calcite [29] crystal, this was accompanied with the disappearance of the vaterite signature of 877 cm^{-1}. This is further confirmed from the spot-profile EDAX analysis of the calcined sample, which shows retention of Ca and O signal and complete absence of the N and S signals (curve 3 Figure 5.12A).

5.3.3 X-Ray Diffraction (XRD) and Gel-Electrophoresis measurements

XRD analysis of solution-cast films on glass substrates for the as synthesized biogenic $CaCO_3$ crystals is shown as curve 1 in Figure 5.13. A number of Bragg reflections have been identified and have been marked with reference to the vaterite polymorph of $CaCO_3$. It has been already mentioned that there is a complete transformation of the observed phase on calcination at 300 ^{0}C for 3 hours.

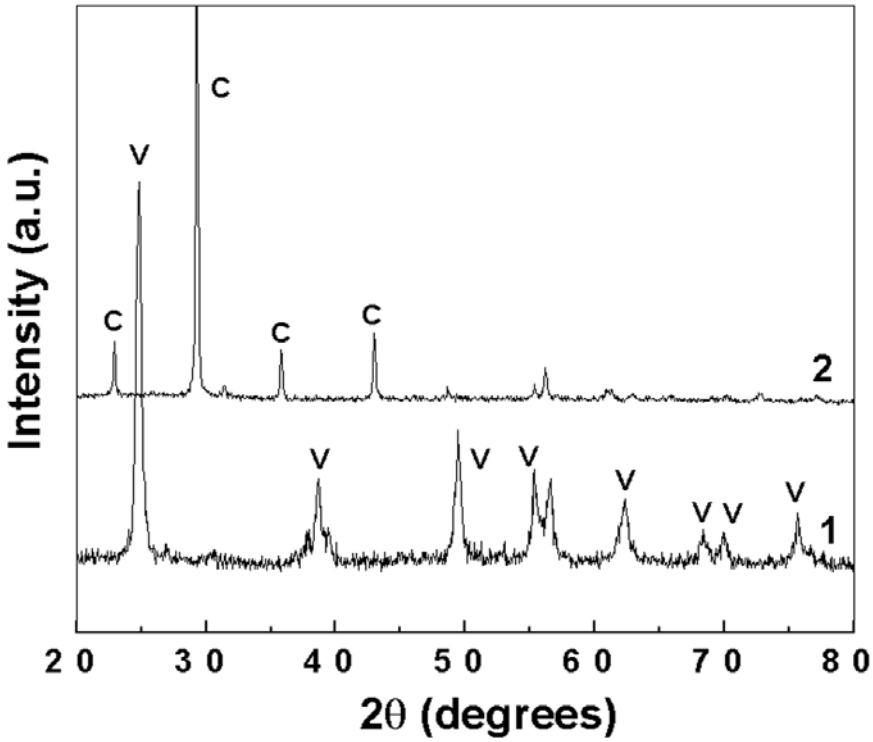

Figure 5.13: *XRD patterns recorded from solution-cast films of $CaCO_3$ crystals synthesized using chickpea seeds before calcination (Curve 1) and after calcination (Curve 2). 'C' corresponds to calcite while 'V' corresponds to vaterite.*

This is confirmed from the XRD pattern of the calcined sample (curve 2, Figure 5.13) which shows complete disappearance of the vaterite peaks and appearance of new peaks characteristic of calcite ($2\theta = 29^0$). The transformation of vaterite to calcite is generally brought about by a solvent-mediated process [30] or in the presence of metal ions like Cu^{2+} [31]. This is very much different from the usual method which further strengthens our belief that some proteins are definitely playing a major role in stabilizing the unstable vaterite polymorph.

The surface-bound proteins released from the vaterite crystals grown by reaction of Ca ions with the chickpea seeds were removed by NaOCl treatment as briefly discussed in a previous page and subjected to analysis by gel electrophoresis. The aqueous extract containing the proteins bound to the surface of the biogenic $CaCO_3$ crystals was analyzed by 12% SDS-PAGE carried out at pH 8.2, and the gel was subsequently silver stained [32]. Preliminary gel electrophoresis measurements (Figure

5.14) indicate the presence of two distinct proteins having molecular weights of 33 and 29 kDa (Figure 5.14, lane 2).

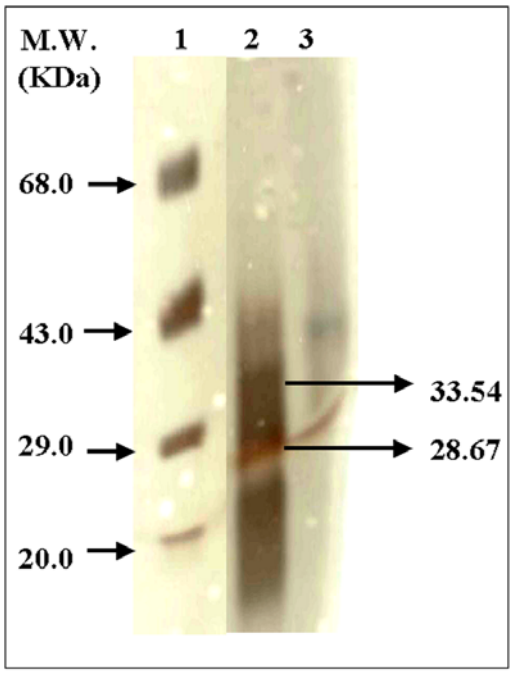

Figure 5.14: *SDS-PAGE data showing the contribution of the proteins involved in the stabilization of the vaterite crystals grown in the presence of chickpea seeds. Lane 1 shows standard protein molecular weight markers with the corresponding molecular weights in kDa indicated by arrows. Lane 2 corresponds to the protein bands in the extract obtained by NaOCl treatment of vaterite crystals grown using chickpea seeds. Lane 3 shows the protein bands present in the plain chickpea extract.*

However the contribution of minor proteins responsible for the stabilization of vaterite polymorph cannot be negated. We believe that these two proteins are the major inducible proteins secreted by the chickpea seeds in response to exposure to aqueous Ca^{2+} ions and are also responsible for stabilization of the vaterite phase. These two protein bands are not present in the SDS-PAGE analysis of the proteins present in the extract obtained by soaking chickpea seeds in water for 5 days (Figure 5.14, lane 3). Lane 1 in Figure 5.14 corresponds to SDS-PAGE of standard protein markers.

5.3.3 Summary

The total biological synthesis of the metastable vaterite polymorph of $CaCO_3$ with controlled morphology by simple protein-mediated reaction of aqueous Ca^{2+} ions with the CO_2 generated during the root growth from chickpea seeds has been described. That the carbonate ions are provided by the plant organism itself significantly enhances the application potential of this approach with important implications in crystal engineering, catalyst design and so forth. Specific proteins secreted during root growth play a very important role in directing and stabilizing the metastable vaterite polymorph.

5.4 Calcite growth using a traditional Indian plant extract

As discussed earlier in a previous note that apart from calcium carbonate, among the many inorganic minerals present in biological systems, calcium hydroxyapatite, the major component in bones and teeth, is the other important calcium-based mineral due to its biocompatible [7] and biodegradable properties [8]. Consequently, considerable effort has been devoted to understanding how and why this mineralization takes place and a number of biomimetic strategies have been developed to grow calcium hydroxyapatite in the laboratory [33-35]. Traditional recipes for treatment of physical and mental ailments exist in all major ancient civilizations of the world. One such recipe popular in the Indian subcontinent involves the use of the extract of the plant *Cissus quadrangularis*. The stem and root extracts of this medicinal plant are known to possess antioxidant and antimicrobial activity [36] and are routinely used to accelerate the process of bone-fracture healing [37]. In spite of the fact that various organic macromolecules ranging from terpenoids to large stilbene derivatives [38] have been isolated from this plant, very few reports exist on its ability to accelerate bone fracture healing [39]. Here, we have analyzed the extract of the stem of *Cissus quadrangularis* from the point of view of its putative ability to promote mineral growth.

The broth used in the experiments was prepared by taking 40 gm of thoroughly washed and finely cut *Cissus quadrangularis* stems in a 500 ml Erlenmeyer flask. To the biomass, 100 ml of distilled water was added and then boiled for 5 mins. After boiling, the solution was decanted and filtered, and CO_2 was bubbled through 5 ml of the broth. After 3 h of reaction, the originally wheat colored solution was observed to turn turbid

and after 1 day of reaction, the particles settled down at the bottom of the test tube. The precipitate was filtered, washed with copious amounts of water and redispersed in water. Films of the purified crystals were prepared by simple solution-casting onto Si (111) wafers for scanning electron microscopy (SEM) and energy dispersive analysis of X-rays (EDAX) studies.

5.4.1 Scanning Electron Microscopy (SEM) studies

Figure 5.15A shows a picture of the *Cissus quadrangularis* plant. The plant is a Xerophyte, which means that it possesses a cactus-like overall appearance and grows under arid conditions.

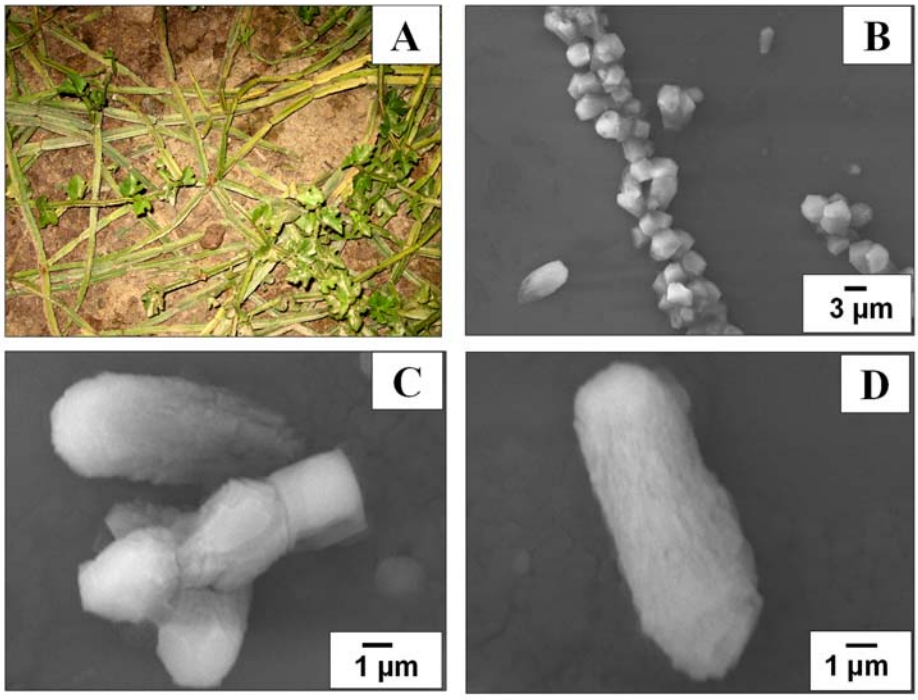

Figure 5.15: *(A) Photograph of Cissus quadrangularis plant. (B)-(D) Representative SEM micrographs at different magnifications of $CaCO_3$ crystals grown from the extract of C. quadrangularis plant.*

Figures 5.15B-D show representative SEM images of the $CaCO_3$ crystals at different magnifications. At various places on the substrate surface, we could observe quasi-spherical particles of irregular morphology assembled in a linear fashion (Figures 5.15B, C). The size of the particles varies between 3 and 10 µm. While the reasons for this assembly are not understood at this stage, it is possible that it is driven by

interactions between biomolecules present on the particle surface. Some of the particles exhibit cube-like and highly elongated ellipsoidal morphologies (Figure 5.15D).
All the particles possess a highly irregular and corrugated surface, very unlike the smooth, rhombohedral crystals observed in chemically synthesized calcite [40].

In order to get an idea about the stability of the crystals formed, we have characterized the crystals at different time intervals of growth by SEM (Figure 5.16). It is observed that after 30 mins of reaction, a large number of highly irregular crystals are formed (Figure 5.16 A).

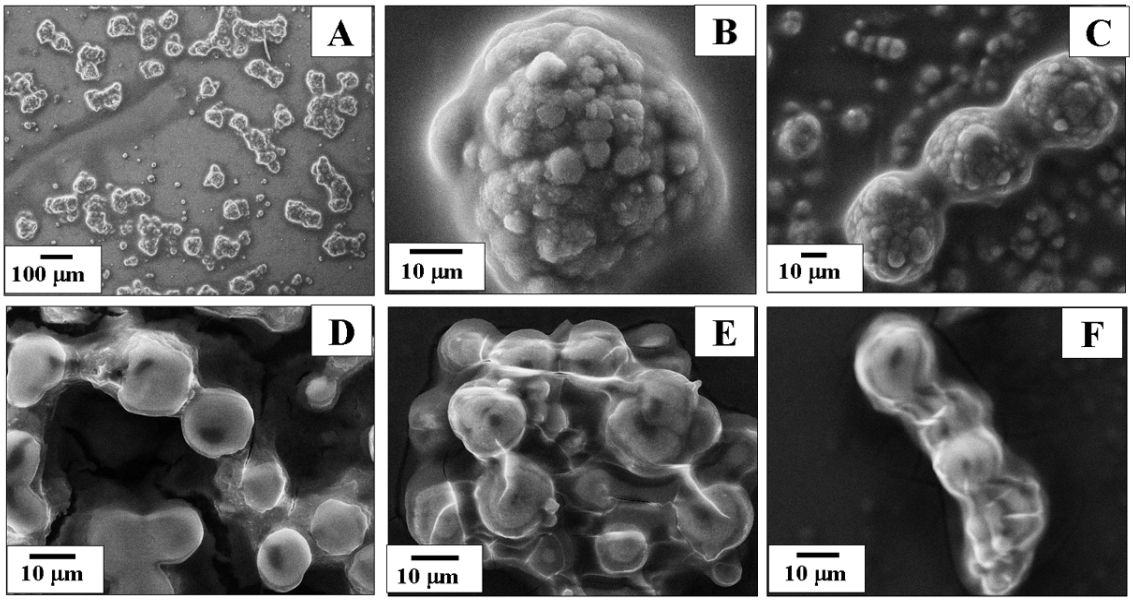

Figure 5.16: *Representative SEM images of calcite crystals formed at different time intervals by bubbling CO_2 into the plant extract of C. quadrangularis.(A),(B) 30 min of reaction**;** (C), (D) 2 and 4 h of reaction respectively; (E), (F) 1 and 2 days of reaction respectively.*

At higher magnification, the structures are seen to be composed of sphero-aggregates of much smaller crystals (Figure 5.16 B). As the time of reaction increases, it is observed that the crystals within the superstructures increase in size (Figure 5.16 C and D, SEM images recorded after 2 and 4 h of reaction respectively). An interesting observation is that the sphero-aggregates tend to assemble in a linear fashion, very much similar to the crystals shown previously in Figure 5.15 C. The crystals are assembled in a

quasi-linear fashion suggesting that the biomolecules present are either surface bound or have been intercalated within the crystal. After 2 days of reaction, the crystallites within the spherical superstructure have re-crystallized to yield single particles assembled in a linear manner (Figure 5.16 E and F).

5.4.2 X-ray Diffraction and EDAX analysis

Curve 1 in Figure 5.17 shows the XRD pattern recorded from the crystals coated on Si (111) substrate. A number of Bragg reflections have been identified and indexed with reference to the unit cell of the calcite phase [(*a, b* = 4.989 Å, *c* = 17.062 Å, space group $D_{3D}6$- *R*3*c*] [41].

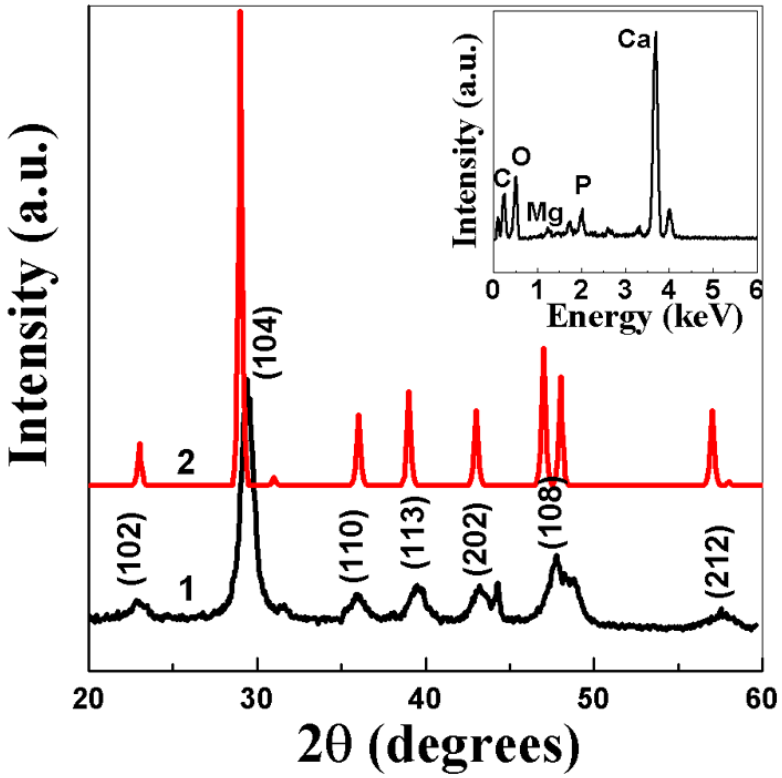

Figure 5.17: *XRD pattern recorded from biogenic $CaCO_3$ powder obtained after bubbling CO_2 into the extract of C. quadrangularis and subsequent drying (Curve 1) and Curve 2 is the simulated diffraction pattern for $CaCO_3$. The inset shows spot-profile EDAX spectrum of the $CaCO_3$.*

The morphology of the calcite crystals obtained from the *Cissus quadrangularis* plant extract is significantly different from that normally observed for calcite, which indicates

the important role of bioorganic molecules present in the extract in modulating the morphology of the crystals. This can be compared to the synthesis of calcite crystals using bovine serum albumin [42] or the self-assembled growth of calcite crystals [43] wherein proteins make an important contribution to the morphological growth of the crystals. It is well known that calcite in biological systems can exist in highly complex morphologies wherein growth in confined reaction spaces and in the presence of specific biomolecules directs the morphology [44]. The inset of Figure 5.17 shows the spot profile EDX spectrum recorded from the crystals shown in Figure 5.15D. In addition to the C and O signals, an intense Ca signal and peaks corresponding to Mg and P are also observed. The signal of Mg could be due to its inheritent presence in the cell wall. From EDX analysis the Ca: C atomic ratio is found to be 1: 3.8. The difference from the expected 1:1 ratio may be due to the presence of biological molecules present in the crystals that would contribute to an enhanced C signal. The presence of Mg may be due to formation of $MgCO_3$. It can be compared from the simulated diffraction pattern of calcite morphology (curve 2 in Figure 5.17) that the XRD pattern from the crystals (curve 1 of Figure 5.17) show that the Bragg reflections are broad, most likely due to the presence of $MgCO_3$ which possesses a crystal structure identical to calcite with marginally different lattice spacings [45].

5.4.3 FTIR and Transmission Electron Micrograph results

The formation of calcite is further supported by FTIR spectroscopy analysis of the $CaCO_3$ crystals taken in a KBr pellet (Figure 5.18A, curve 2). For comparison, the FTIR spectrum recorded from the lyophilized powder of the plant extract is shown (curve 1, Figure 5.18A). A comparison of the two curves shows that two strong absorption band appear at ca. 712 and 870 cm^{-1} in the $CaCO_3$ crystals (curve 2) that are clearly missing in the plant extract (curve 1).

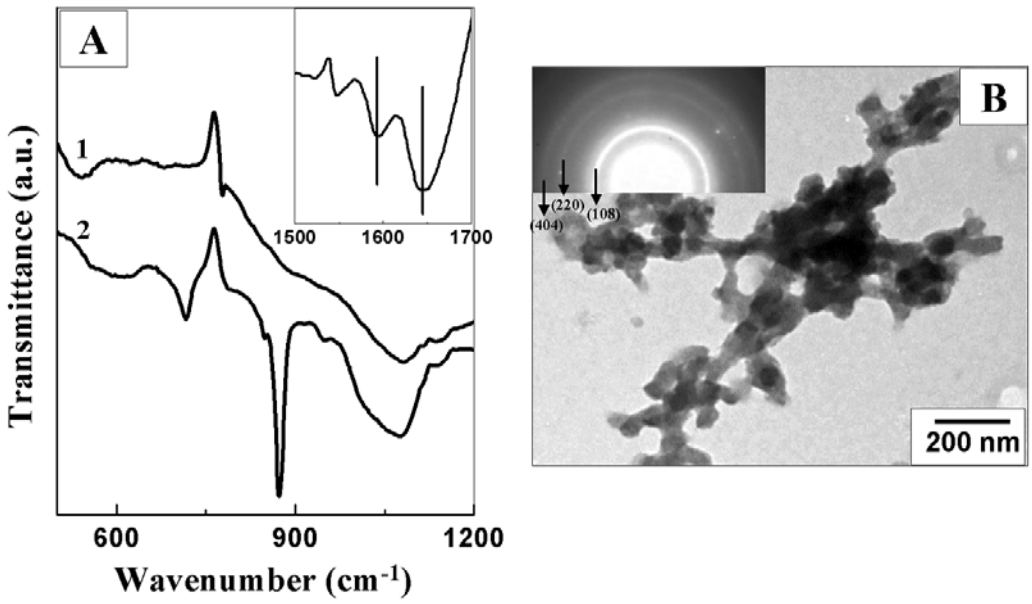

Figure 5.18: *(A) FTIR spectra recorded from pure stem extract (Curve 1) and from the biogenic $CaCO_3$ crystals obtained by bubbling CO_2 into the extract of C. quadrangularis (Curve 2). (Inset) Region of amide vibrational modes are identified. (B) Representative TEM image of the $CaCO_3$ crystals held together by surface-bound proteins, the inset shows the Selected Area Electron Diffraction (SAED) pattern from one of the crystals. The rings have been indexed with the lattice structure of calcite.*

These two peaks are characteristic of the pure form of calcite [29]. That the crystals are bound together by some kind of protein sheath is evident from the representative transmission electron (separate TEM analysis) micrograph shown in Figure 5.18B. The inset of Figure 5.18B shows the Selected Area Electron Diffraction (SAED) from the center of the crystal as shown in the main image of Figure 5.18B and has been indexed with respect to the lattice parameters of calcite. That these crystals contains a considerable amount of biomolecules can be confirmed from the presence of highly intense amide band *c.a.* 1590 and 1650 cm^{-1} as is evident from the FTIR spectrum of these crystals shown in the inset of Figure 5.18A.

5.4.4 X-ray Photoelectron Spectroscopy studies (XPS)

Since the plant has traditionally been used as a recipe for the treatment of bone fractures, hence it should be extremely interesting to study the chemical composition of

the crystals formed. A chemical analysis of the calcite crystals grown using the *Cissus quadrangularis* extract and deposited in the form of a film on Si (111) wafers was carried out by X-ray photoemission spectroscopy (XPS). Figures 5.19A and B show the C 1s and Ca 2p core level spectra respectively. In the C 1s spectrum (Figure 5.19A), curves 1, 2 and 3 correspond to the chemically distinct C 1s core levels with binding energies of 285, 286.6 and 288.4 eV respectively.

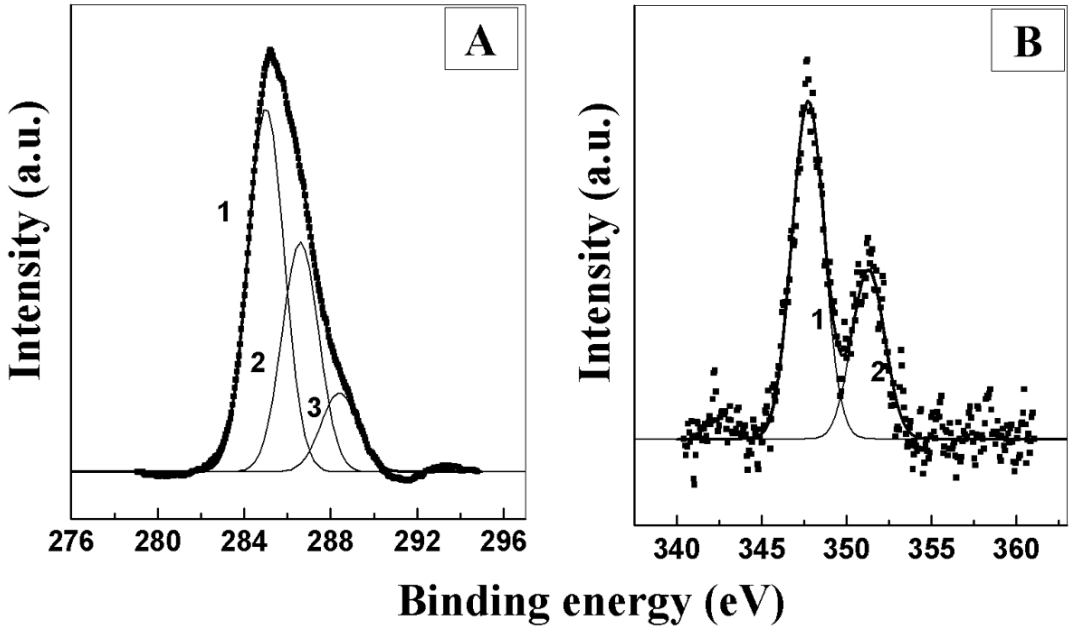

Figure 5.19: *(A) C 1s core-level spectrum recorded from a drop-cast film of $CaCO_3$ crystals formed by bubbling CO_2 into the plant extract on a Si (111) substrate together with the chemically distinct components (1–3). (B) Ca 2p core-level spectrum recorded from a drop-cast film of calcite crystals synthesized by bubbling CO_2 into the stem extract of C. quadrangularis on Si (111) substrate. Curves 1 and 2 correspond to deconvoluted spin-orbit pairs of the 2p component.*

These binding energies most likely originate from the hydrocarbon chains, α-carbon and keto (-C=O) groups present in the protein fraction of the aqueous extract respectively. The Ca 2p core level spectrum (Figure 5.19B) could be resolved into a single spin-orbit pair (splitting ~ 3.55) with a $2p_{3/2}$ binding energy (BE) of 347.7eV. This binding energy is characteristic of calcium carbonate [46]. A weak P 2p signal was also recorded from the calcite crystals. However, the signal-to-noise ratio of this core level was not sufficient to perform a reliable quantitative analysis.

5.4.5 Summary

We have shown here the formation of truly biogenic $CaCO_3$ crystal of exquisite morphology by simply bubbling CO_2 into the aqueous stem extract of an indigenous medicinal plant, *C. quadrangularis*. The plant contains high percentage of calcium probably due to its thick cell wall, which makes it suitable for growth of mineral crystals. The presence of phosphorous in the plant can also be exploited for synthesizing hydroxyapatite, thus utilizing the traditional knowledge of bone-fracture healing in advanced technique of new material synthesis.

5.5 Conclusion

This chapter describes some biomimetic approaches to the synthesis of inorganic mineral crystals namely $CaCO_3$, $CdCO_3$, $PbCO_3$ of interesting morphology. Given the fact that the fungus used in our experiments is not exposed to metal ions described herein in its lifetime, the nature with which it transforms these salts into mineral carbonates of a particular morphology at room temperature is exciting from materials perspective. The transformation is definitely the handiwork of a large number of enzymes, proteins and biomacromolecules in unison in order to achieve such extraordinary structure. Although at this particular state we have been able to identify the major protein responsible for the morphology selectivity, yet a lot of work still remains in the understanding of binding of the proteins to specific crystallographic face in order to achieve morphology selectivity. A very similar reasoning has been given to the synthesis of mineral crystals through seed and plant extracts. The simple approach with which these biogenic methods assist in the generation of inorganic mineral crystals enhance the possibility of use of these procedures in large-scale synthesis with significant applications in crystal growth and engineering.

5.6 References

[1] Bazylinksi, D.A. *Chem. Geol.* **1996**, *132,* 191.

[2] Addadi, L.; Weiner, S. *Nature***, 1997,** *389*, 912**.**

[3] Round, F.E.; Crawford, R.M.; Mann, D.G. *Diatoms: Biology and Morphology of the Genera: Cambridge University Press* **1990.**

[4] Bazylinksi, D.A. *Encyclopedia of Materials: Science and Technology* **2001**, 441.

[5] Ozin, G.A. *Acc. Chem. Res.*, **1997,** *30*, 17.

[6] Thompson, D. W. *On Growth and Form*; Cambridge University Press: Cambridge, **1917**. (b) Thompson, D. W. *On Growth and Form*, complete revised edition; Dover Publications: New York, **1992**, 708.

[7] Schmidt, H. T.; Gray, B. L.; Wingert, P. A.; Ostafin, A. E. *Chem. Mater*, **2004**, *16*, 4942.

[8] Habibovic, P.; Barrere, F.; Van Blitterswijk, C. A.; De Groot, K.; Layrolle, P. *J. Am. Ceram. Soc.* **2002**, *85*, 517.

[9] Lu, J. X.; Descamps, M.; Dejou, J.; Koubi, G.; Hardouin, P.; Lemaitre, J.; Proust, J.-P. *J. Biomed. Mater. Res.* **2002**, *4*, 408.

[10] Damle, C.; Kumar, A.; Bhagwat, M.; Sainkar, S.R.; Sastry, M. *Langmuir* **2002**, *18,* 6075. (b) Rautaray, D.; Sainkar, S. R.; Sastry, M. *Chem. Mater.* **2003**, *15*, 2809.

[11] Falini, G.; Gazzano, M.; Ripamonti, A. *Adv. Mater.* **1994**, *6*, 46. (b) Donners, J. J. J. M.; Nolte, R. J. M.; Sommerdijk, N. A. J. *J. Am. Chem. Soc.* **2002**, *124*, 9700.

[12] Walsh, D.; Mann, S. *Nature* **1995**, *377*, 320.

[13] Qi, L. ; Li, J. ; Ma, J. *Adv. Mater.* **2002**, *14*, 300.

[14] (a) Sondi, I.; Matijevic, E. *Chem. Mater.* **2003**, *15*, 1322. (b) Grajeda, J. P. R.; Zuniga, D. J.; Batina, N. Salazar, M. S.; Moreno, A. *J. Crystal Growth* **2002**, *234*, 227. (c) Qi, L.; Ma, J.; Cheng, H.; Zhao, Z. *J. Phys. Chem. B* **1997**, *101*, 3460.

[15] Yu, S- H.; Colfen, H.; Xu, A. W.; Dong, W. *Crystal Growth & Design* **2004**, *4*, 33.

[16] Stephen, J. R.; Maenaughton, S. J. *Curr. Opin. Biotechnol.* **1999**, *10*, 230.

[17] Mehra, R. K.; Winge, D. R. *J. Cell. Biochem.* **1991**, *45*, 30.

[18] Ahmad, A.; Senapati, S.; Khan, M. I.; Kumar, R.; Sastry, M. *Langmuir* **2003,** *19,* 3550.

[19] Mukherjee, P.; Senapati, S.; Mandal, D.; Ahmad, A.; Khan, M. I.; Kumar, R.; Sastry, M. *ChemBioChem* **2002**, *3*, 461.

[20] Ahmad, A.; Mukherjee, P.; Mandal, D.; Senapati, S.; Khan, M. I.; Kumar, R.; Sastry, M. *J. Am. Chem. Soc.* **2002**, *124*, 12108-12109

[21] Shankar, S. S.; Ahmad, A.; Sastry, M. *Biotechnol. Prog.* **2003,** *19,* 1627.

[22] Rautaray, D.; Ahmad, A.; Sastry, M. *J. Am. Chem. Soc.* **2003**, *125*, 14656.

[23] Rautaray, D.; Sanyal, A.; Adyanthaya, S. D.; Ahmad, A.; Sastry, M. *Langmuir* **2004**, *20*, 6827.

[24] Yu, S-H.; Colfen, H; Antonietti, M. *J. Phys. Chem. B* **2003,***107,* 7396.

[25] Templeton, A. C.; Chen, S.; Gross, S. M.; Murray, R. W. *Langmuir* **1999**, *15*, 66.

[26] The XRD patterns were indexed with reference to the unit cell of the $PbCO_3$ structure (a = 5.178 Å, b = 8.515 Å, c = 6.146 Å; space group *Pmcn*, ASTM chart card no. 47-1734) and $CdCO_3$ structure (a = 4.929 Å, c = 16.30 Å; space group *R3c*, ASTM chart card no. 42-1342) from *ASTM* chart.

[27] Smith, M. T.; Staden, J. V. *Environmental and Experimental Botany* **1995**, *35*, 113.

[28] Naka, K.; Chujo Y.*Chem Mater* **2001**, *13*, 3245.

[29] Falini, G.; Albeck, S.; Weiner, S.; Addadi, L. *Science* **1996**, *271*, 67.

[30] Lopezmacipe, A.; Fomezmorales, J.; Rodriguezclemente, R.*J. Cryst. Growth* **1996**, *166*, 1015.

[31] Nassrallah-Aboukaı¨s, N.; Boughriet, A.; Laureyns, J.; Aboukaı¨s, A.; Fischer, J. C.; Langelin, H. R.; Wartel, M. *Chem. Mater.* **1998,** *10,* 238.

[32] Laemmli, U. K. *Nature* **1970**, *227*, 680.

[33] Cao, M., Wang, Y., Guo, C., Qi, Y. and Hu, C. *Langmuir*, **2004**, *20*, 4784.

[34] Jillavenkatesa, A. and Condrate, R. A. S. R *J. Mater. Sci.*, **1998**, *33*, 4111.

[35] Loher, S.; Stark, W. J.; Maciejewski, M.; Baiker, A.; Pratsinis, S. E.; Reichardt, D.; Maspero, F.; Krumeich, F.; Gunther, D. *Chem. Mater.* **2005**, *17*, 36.

[36] Murthy, K. N. C.; Vanitha, A.; Swami, M. M.; Ravishankar, G.A. *J. Med. Food*, **2003**, *6*, 99.

[37] Udupa, K. N.; Prasad, G. C. *Indian J.Med. Res.* **1964**, *52*, 26

[38] Adesanya, Saburi, A.; Rene, N.; Martin, M-Therese; Boukamcha, N.; Montagnac, A.; Pais, M. *J. Nat. Prod.* **1999**, *62*, 1694.

[39] Deka, D. K.; Lahon, L. C.; Saikia, J.; Mukit, A. *Indian J. Pharmacol.*, **1994**, *26*, 44.

[40] DeOliviera, D. B.; Laursen, R. *J. Am. Chem. Soc.* **1997**, *119*, 10627.

[41] The XRD patterns were indexed with reference to the unit cell of the calcite structure; ([*a*, *b*) = 4.989 Å, *c* = 17.062 Å, space group $D_{3D}6$-*R*3*c*, ASTM chart card no. 5-0586].

[42] Nayar, S.; Sinha, A. *J. Mater. Sci. Lett.* **2003**, *22*, 167.

[43] Sinha, A., Chakraborty, J., Das, S. K. and Ramachandrarao, P *Curr. Sci.* **2003**, *84*, 1437.

[44] Kato, T.; Sugawara, A.; Hosoda, N. *Adv. Mater.* **2002**, *14*, 869.

[45] Magnesium carbonate is of the space group D3D6-*R*3*c*, with crystallographic axis (*a*, *b*) = 4.633 Å, *c* = 15.01 Å, PCPDF file no. 08-0479, CAS no. 13717-00-5.

[46] Muilenberg, G. E. *et al.*, In *Handbook of X-ray Photoelectron Spectroscopy*, Perkin-Elmer Corporation, **1979**, p. 64.

CHAPTER VI

Conclusions

This chapter outlines the salient feature of the work described in this thesis and emphasizes possible future scope in this field of work.

6.1 Summary of the Research Work

Synthesis of nanomaterials with fascinating optical and electronic properties has resulted from an interdisciplinary effort of various researchers since the last two decades. Colloidal metal nanoparticles especially gold and silver are of importance as they are biocompatible and had been used in a variety of applications ranging from drug delivery [1], anti bacterial-agents [2] to catalysis. The properties of nanomaterials can be largely altered by tuning the shape and size of the nanoparticles, hence there has been much of interest in the synthesis of 2D, 1D and anisotropic nanostructures like nanowires, nanorods, nanotriangles, nanosheets, nanofibres and so on.. The objective of this thesis was directed towards the use of different inorganic composites for the synthesis of nanoparticles. Focus has also been provided to the synthesis of hybrid organic-inorganic nanostructures by use of "Keggin ion". It has been observed that phosphotungstic acid (a type of Keggin ion), due to its inherent high negative charge and acidic nature, complexes with amino acids having a high pI value forming nicely designed fibre kind of structures. These fibres range from 100-150 μm in length and ~40-50 nm wide. Due to the remarkable UV-switchable reducing property of these fibres, they were then used to synthesize gold nanoparticles on these hybrid fibre-like structures with precise control over their assembly. We have also made an attempt to synthesise gold nanosheets at the liquid-liquid interface by the use of Keggin ions in the aqueous phase and anthracene in the organic phase. Further to the formation of anisotropic nanostructures, by use of a different Keggin ion (phosphomolybdic acid) and following the same reaction as that of phosphotungstic acid, we ended up synthesising gold nanotriangles having a high degree of anisotropy. We have also suggested a mechanism for the change in the products obtained. Finally we have shown that inorganic mineral crystals can be obtained by challenging microorganisms into the salts of the desired material. We have thus been able to remove toxic heavy metal ions like Cd^{2+} and Pb^{2+} via the formation of their corresponding carbonates. The striking design in which the crystals grow is thus the handiwork of a large of enzymes that work in unison for the creation of such structures. Although the mechanism of growth of these mineral crystals with a defined orientation appears to be quite intricate, yet we have shown the presence of a dominant as well as some dormant proteins which is responsible for the particular

structure formation. As a continuation to this work we have also shown that such mineral crystals can also be grown with different plant extracts and seeds during their germination.

6.2 Scope for further work

Template based synthesis is one of the most general and versatile methods for the synthesis of nanoparticles. The use of Keggin ion-amino acid hybrid super-structures has thus opened up a new direction for the controlled growth of nanoparticles. The versatility of these nanoreactors can be utilised in the synthesis of magnetic and other commercially important nanoparticles too. As we have elucidated that rate of the reduction is one of the key factors for the growth of anisotropic nanostructures, hence use of different type of Keggin ions (silicotungstic acid, "Dawson" type of structures) could lead to a different result which would be very interesting to pursue. Combining the reducing capability of the Keggin ions and the anisotropy inherent in the liquid-liquid interface can further help us to grow nanostructures of transition metal ions like Co, Ni and Cu, which would find application in electronic and magnetic storage devices. The nanosheets described in this thesis, as are formed at the interphase, can be tested for various catalysis and separation techniques. Further insight into the reaction mechanism can be obtained if we are able to study the crystal structure of these superstructures which can surely be an extension to the work mentioned in this thesis.

The most intricate designs present in this earth are of nature's creation and we are just at the primary stage of understanding the process of "biomineralization", hence a vivid study into the proteins, their sequence and so on will help us to comprehend the exact role played by them in the crystal nucleation and growth. A detailed knowledge will further lead to the controlled growth of such mineral crystals with wide applications in crystal and genetic engineering.

6.3 References

[1] Paciotti, G.; Myer, L.; Weinreich, D.; Goia, D.; Pavel, N; Maclaughlin, R.; Tamarkin, L. *Drug Delivery* **2004**, *11*, 169.

[2] Lee, H. J.; Yeo, S. Y.; Jeong, S. H. *J. Mater. Sc.* **2003**, *38*, 2199.

List of Publications

1. "*Gold nanosheets via reduction of aqueous chloroaurate ions by anthracene anions bound to a liquid-liquid interface"*
   Ambarish Sanyal and Murali Sastry, *Chemical Communications* **2003**, 1236 – 1237.

2. **"***Synthesis and Assembly of CdS Nanoparticles in Keggin Ion Colloidal Particles as Templates"*
   Saikat Mandal, Debabrata Rautaray, **Ambarish Sanyal** and Murali Sastry**,** *J. Phys. Chem. B.* **2004**, *108*, 7126 –7131.

3. "*Biological Synthesis of Strontium Carbonate Crystals Using the Fungus Fusarium oxysporum"*
   Debabrata Rautaray, **Ambarish Sanyal**, Suguna D. Adyanthaya, Absar Ahmad, and Murali Sastry, *Langmuir* **2004,** *20***,** 6827-6833.

4. *"Biological synthesis of stable vaterite crystals by the reaction of calcium ions with germinating chickpea seeds"*
   Debabrata Rautaray, **Ambarish Sanyal**, Absar Ahmad and Murali Sastry
   Cryst.Growth & Des. **2005**, *5*, 399-402.

5. *"Synthesis and assembly of gold nanoparticles in quasi linear lysine-Keggin ion colloidal particles as a template"*
   Ambarish Sanyal, Saikat Mandal and Murali Sastry, *Adv. Funct. Mater* **2005**, *15*, 273-280.

6. *"Heavy metal remediation by a fungus as a means of production of lead and cadmium carbonate crystals"*
   Ambarish Sanyal, Debabrata Rautaray, Vipul Bansal, Absar Ahmad and Murali Sastry, *Langmuir* **2005,** *21*, 7220-7224.

7. *"Calcite growth in Cissus quadrangularis plant extract, a traditional Indian bone healing aid"*
   Ambarish Sanyal, Absar Ahmad and Murali Sastry, *Curr.Sci.* **2005,** *89***,** 1742-1745.

8. "*Synthesis of gold nanotriangles using Keggin-lysine hybrid nanostructures"*
   Ambarish Sanyal and Murali Sastry, *Langmuir **(2006)**, communicated*

9. *"Bioleaching of sand by the fungus Fusarium oxysporum as a means of producing extracellular silica nanoparticles"*

Vipul Bansal, **Ambarish Sanyal**, Debabrata Rautaray, Absar Ahmad and Murali Sastry, *Adv.Mater.***2005**, *17*, 889-892.

10. *"Fungus-mediated biosynthesis of silica and titania particles"*
Vipul Bansal, Debabrata Rautaray, Atul Bharde, Keda Ahire, **Ambarish Sanyal**, Absar Ahmad and Murali Sastry, *J.Mater.Chem.* **2005**, *15***,** 2583-2589.

List of Patents filed

1. *"Biological process for the preparation of mineral crystals using seeds*
Absar Ahmad, Debabrata Rautaray, **Ambarish Sanyal** and Murali Sastry
U.S. Pregrant Abstract 20050214194, Serial No: 807992, Series Code: 10
Filed: 2004-03-23